Fluorescence-doped silica nanoparticles for ultrasensitive detection of prostate specific antigen

A thesis submitted in fulfilment of the requirements.

for the degree of

MASTER OF SCIENCE

Of

RHODES UNIVERSITY

By

TUMELO MSUTU

ORCID

0000-0003-1054-5154

February 2024

DEDICATIONS

This work is dedicated to my late cousin Tshepo Percy Ralepobi who battled with cancer and sadly passed on in 2019 at only the age of 24, and also to other individuals that may be battling with cancer or have a loved one affected by cancer.

More importantly I dedicate this work to my mother, father, siblings, and close relatives.

ACKNOWLDEMENTS

I would like to first and foremost thank my lord and saviour Jesus Christ for this moment in my life. A special thank you and immeasurable appreciation to my supervisor Professor Philani Mashazi, for all the knowledge imparted, support, and making this work possible. Your endless advice and guidance carried me through all this scientific journey. Thank you for reviewing my work progress reports, manuscripts, and this thesis. Your invaluable insight and support during my work presentations has shaped the research enthusiast that I am today.

My deepest gratitude to our nanoBiosensor Research Group (F3/F5). You were not only a research group but my second family. Thank you for sharing your contributions in expanding my insight in this research and sharing your knowledge and expertise accompanied by the brilliant comments that help advance my work. To my mentors, Dr Omotayo K. Adeniyi and Dr Daniel Mwanza, thank you for the valuable lessons.

The Gauteng City Regional Academy (GCRA), Tastic Rice legacy fund, and Sandisa Imbewu, thank you for the financial support for my MSc studies.

Warm thank you to my parents, Mr Johannes Msutu and Mrs Nancy Khamelile Msutu; siblings, Tebogo Msutu, Glady Msutu, Nelson Msutu, Mpho Ardinas Mathebe; Sekoro William Makgasha, Aphelele Ntlantsana, and my friends. Thank you all for your endless support and words of encouragement. I am grateful for your love and prayers.

I would like to extend my gratitude to Rhodes University, the Chemistry department, staff, and fellow postgraduate students for all the assistance and support.

ABSTRACT

Prostate cancer (PCa) is the topmost diagnosed cancer in males in South Africa according to the National Cancer Registry 2020, affecting both adolescent and young adult men. Currently, PCa is diagnosed using the dreaded digital rectal examination (DRE) followed by tissue biopsy, and prostate-specific antigen (PSA) test for confirmation. DRE is an invasive method and can detect PCa in late stages when the tumour has formed. Therefore, there is a need for early diagnosis technology, that can detect PCa during carcinogenesis. PSA test offers this opportunity even though it is non-specific. This test is a non-invasive, well-established, and conventional method used as a confirmatory test. However, the test suffers from shortfalls like the misdiagnosis of benign prostatic hyperplasia (BPH) or prostatitis as prostate cancer. In this work, we have developed an ultrasensitive fluorescence-based PSA test based on the oriented immobilization of *anti*-PSA monoclonal and polyclonal antibodies. *Anti*-PSA polyclonal antibodies (*anti*-PSA-pAb) were bioconjugated via boronate ester onto the fluorescein-5-isothiocyanate (FITC) doped silica nanoparticles for detection. *Anti*-PSA monoclonal antibodies were used as capture antibodies on dark fluorescence microplate or magnetic nanoparticles. A sandwich immunoassay was used for the detection of PSA. The *anti*-PSA-pAb was bioconjugated on the surface of the FITC-doped silica nanoparticles. In the design, the FITC-(3-aminopropyl)triethoxysilane (APTES) organosilane precursor was encapsulated into the silica nanoparticles to form fluorescent silica nanoparticles (FITC@SiO_2NPs). The silica shell prevented dye leakage and promoted fluorescent signal amplification. Optimization of the as-prepared fluorescent silica nanoparticles was investigated at altered FITC-dye loadings of 3.0% and 6.0% (for high loading). The fluorescent silica nanobioconjugates exhibited a strong excitation-dependent emission property at 518 nm and was photostable over time. The fluorescent silica nanoparticles exhibited 65% dye loading for both 3.0% and 6.0% silica nanoparticles respectively for 30 ± 3 nm and 46 ± 2 nm. The fluorescent nanobioconjugates' performance was evaluated using black 96-well microplates. A fluorescence sandwich-type immunoreaction was achieved via the antibody-antigen reaction of the FITC@SiO_2-prAmPBA-*anti*-PSA-pAb/glucose nanobioconjugates binding to the captured PSA analyte. NaOH was used for alkali hydrolysis of the sensing nanobioconjugates to release the FITC-APTES molecules, leading to fluorescence signal amplification. The proposed fluorescence immunobiosensor exhibited a linear relationship between the fluorescent signals and the concentration of PSA obtained in the range of 2.0 pg.mL^{-1} to 50 ng.mL^{-1}, with excellent limit of detection and limit of quantification both in the pg.mL^{-1} range in PBS buffer (pH 7.4) and PSA in spiked serum samples. The immunosensor was based on the immunometric sandwich protocol, using nanomagnetic-silica antibody bioconjugates for capture and fluorescent nanobioconjugates as sensing probes. The use of nanomagnetic-silica antibody bioconjugates allowed concentration of PSA as the analyte and ease of separation using a magnet. Alkali hydrolysis of the sensing fluorescent nanobioconjugates is achieved using NaOH, resulting in the release of FITC molecules and an amplified fluorescence detection signal. The analytical performance of the proposed fluorescence immunobiosensor exhibited a linear relationship between the fluorescent signals and the concentration of PSA obtained in the range of 2.0 pg.mL^{-1} to 100 ng.mL^{-1}, with excellent limit of detection and limit of quantification both in the pg.mL^{-1} range in PBS buffer (pH 7.4) and PSA in spiked serum samples. The immunosensor also exhibited good specificity and selectivity for PSA with 94.8% - 102.5% recovery rates. The proposed fluorescence immunoassay exhibited high selectivity and specificity for the detection of PSA.

Table of Contents

LIST OF ABBREVIATIONS

4-CPBA	4-carboxyphenylboronic acid
APTES	(3-aminopropyl)triethoxysilane
Anti-PSA-pAb	Polyclonal *anti*-PSA antibody
Anti-PSA-mAb	Monoclonal *anti*-PSA antibody
ASMR	Age-Standardized Mortality Rate
AMCA	Aminomethylcoumarin Acetate
a.u	Arbitrary Unit
ALP	Alkaline Phosphatase
BPH	Benign prostate hyperplasia
%CV	Coefficient of Variation
Cy3 or Cy5	Cyanine dye 3 or 5
DRE	Digital Rectal Examination
DDSNs	Dye-doped silica nanoparticles
DMSO-d_6	Deuterated Dimethyl Sulfoxide
EDX/EDS	Energy Dispersive X-ray Spectroscopy
EDC	1-ethyl-3-(3-dimethylaminopropyl)carbodiimide hydrochloride
ELISA	Enzyme-linked Immunosorbent Assay
FITC	Fluorescein isothiocyanate
FITC-APTES	Fluorescein-isothiocyanito-3-propyltriethixysilane
FLISA	Fluorescence-linked Immunosorbent Assay
FRET	Förster (Fluorescence) Resonance Energy Transfer
FT-IR	Fourier Infrared Transform Spectroscopy

GLOBOCAN	Global Cancer Statistics
HRP	Horseradish Peroxidase
^{1}H NMR	Proton Nuclear Magnetic Resonance
IEP	Isoelectric Point
LOD	Limit of Detection
LOQ	Limit of Quantification
MIR	Magnetic Resonance Imaging
MNPs	Magnetic Nanoparticles
NaOH	Sodium Hydroxide
NH_4OH	Ammonium Hydroxide
NHS	N-Hydroxysuccinimide
NCS	Newborn Calf Serum
OA	Oleic Acid
PSA	Prostate-Specific Antigen
PBS	Phosphate Buffer Solution.
PBST	Phosphate Buffer Solution with Tween® 20
PCa	Prostate cancer
QDs	Quantum Dots
SEM	Scanning Electron Microscopy
TES-prAmPBA	Triethoxysilanepropyl-3-amido phenylboronic acid
TEM	Transmission Electron Microscopy
TEOS	Tetraethyl orthosilicate
Triton X-100	4-(1,1,3,3-tetramethylbutyl)-phenyl polyethylene glycol
TRUS	Transrectal Ultrasound-guided Needle Biopsy
UV-Vis	Ultraviolet-Visible Spectroscopy

LIST OF FIGURES

LIST OF TABLES

LIST OF SCHEMES

LIST OF PUBLICATIONS

Here is a list of papers prepared for publication and based on the research done in this thesis and therefore will note cited further:

1. Tumelo Msutu, Omotayo K. Adeniyi, Philani Mashazi. Antibody fluorescein-doped silica nanobioconjugate for the ultrasensitive detection of prostate-specific antigen. Sens. Diagn. 3 (2024) 1167-1176.
2. Tumelo Msutu, Philani Mashazi. Using fluorescent dye-doped silica sensing and nanomagnetic silica capture nanobioprobes for ultrasensitive detection of prostate-specific antigen. **(to be submitted)**.

Tumelo contributions: Conceptualization, Method development, Data collection, Data curation, Experimental Execution, Performed Analysis, Validations, Writing first draft, and Editing.

Chapter 1

1.1 Justification

Cancer is characterized by the abnormal and rapid uncontrollable growth of cells in the body and results in tumours or mass damaging the body tissues and body organs such as the lungs, breast, prostate, colorectal, liver, stomach, and more [1–5]. Globally, cancer is the second leading cause of death and the second deadliest non-communicable disease (NCD) after cardiovascular disease (CVD) [6,7]. By 2020, cancer has accounted for about 10 million deaths with an estimated 19.3 million new cancer cases worldwide [8–10]. Lung, prostate, colorectal, stomach, and liver cancers are the most common types of cancer in men. Breast, colorectal, cervical, lung, and thyroid cancers are the most common types of cancer among women [8–10]. The biggest challenge in curbing cancer is the late diagnosis using the current technologies, which involves identifying a tumour. At this stage of diagnosis, the disease (cancer) would have metastasized (affected other organs in the body) making treatment very difficult. Therefore, accurate and sensitive systems for early detection of cancer are of great importance in both biomedical and clinical diagnosis research [11–13]. This is due to the fact that, early detection would detect cancer early (during carcinogenesis) and will allow for effective and timely treatment. Therefore, understanding the physiological processes associated with cancer carcinogenesis is important for the development of sensitive diagnostic systems, thus affording early detection of the disease before it manifests and metastasizes [2,13–16]. Immunobiosensors are essential detection systems used for screening, monitoring, detection, and early diagnosis of cancer and related diseases [1–4].

In men, prostate cancer (PCa) is the main contributor in incidence cases accounting for about 40% of reported cancer cases worldwide [5–10,16,17]. Early PCa diagnosis, treatment, and monitoring is of great interest due to reported high incidence cases, and the second highest mortality rates after lung cancer [5–8]. The high incidence and mortality rates of PCa are due to an increase in the number of late diagnosis and misdiagnosis, which are evident in several asymptomatic patients among men above the age of 50 years [18,19]. Many cases of PCa are detected at advanced tumour stages with the current diagnostic methods. The most common methods of PCa diagnosis are digital rectum examination (DRE), magnetic resonance imaging (MRI), tissue biopsy, and prostate-specific antigen (PSA) screening [20–23]. The DRE, MRI, and tissue biopsy are invasive, non-specific as benign cancer can be diagnosed as PCa, and the diagnosis of PCa is detected at late stages of development when the tumour or mass has metastasized [21–24]. Therefore, making chemotherapy for patients not effective and high chances of cancer reoccurrences [22]. On the other hand, PSA screening is a non-invasive clinical method used for screening, diagnosis, and monitoring of PCa. The method uses the quantification of low concentrations of the PSA biomarker produced during the early stages of PCa development [20,22,25]. Reports have indicated that patients with elevated levels of PSA in blood serum between 4.0 ng.mL $^{-1}$ to 10 ng.mL^{-1} are considered to be at higher risk of developing PCa [26–28]. Therefore, the detection of PSA at the onset of carcinogenesis would allow for a timely and effective chemotherapeutic treatment for patients when detected at low concentrations and early stages of PCa.

Various clinical diagnostic systems and immunoassays for the detection and quantification of PSA have been developed to improve the PSA tests for early diagnosis of PCa. These include commercial enzyme-linked immunosorbent assays (ELISA) [29,30], and biosensors [31] such as electrochemical immunosensor [32], photoelectrochemical immunosensor [33], colorimetric immunoassay [34], and chemiluminescence immunosensor [35]. However, these methods have been shown to require lots of time for analysis, are expensive, use of expensive equipment, and high purity enzymes like horseradish peroxidase (HRP), involve tedious and laborious procedures, require highly skilled personnel for analysis and have high limit of detection. These limitations make these techniques not amenable for practical applications. Therefore, there is a gap in the research for investigating more convenient detection methods for PCa diagnosis with a comparable or even higher sensitivity [36,37]. In this sense, the use of enzyme-free fluorescence immunoassays and biosensors as detection systems recently gained research interest in the quantitative analysis of PSA [38]. This is due to its high sensitivity, low costs, simple instrumentation, and easy operation. Many conventional fluorescence-based biosensors incorporate quantum dots (QDs) [39], upconversion nanoparticles (UCNPs) [40], and organic fluorophores (such as fluorescein, Cy3, and rhodamine) which provide high extinction coefficient for high sensitivity, allow for low limits of detection and ease of preparation at very low costs [41]. However, QDs are of limited use due to cytotoxicity due to the use of heavy metal cadmium (Cd) [39], and upconversion nanoparticles (UCNPs) experience low fluorescence and easily undergo quenching [42]. Moreover, organic dyes are environmentally friendly with low cytotoxicity and high fluorescence in biological systems [41]. Therefore, the development of a cheap, simple, highly sensitive, selective, and specific diagnostic system targeting the detection of PSA antigen in real time is important.

1.2 Problem statement

Prostate cancer is a disease causing a lot of health challenges. Prostate-specific antigen (PSA) is the biomarker that can be used in screening and identifying individuals predisposed to prostate cancer. Therefore, immunoassays that seek to quantify the amount of PSA are needed for early diagnosis of prostate cancer and better than the currently available systems such as DRE and tissue biopsy. Can fluorescence-doped nanoparticles afford sensitive detection and determination of prostate-specific antigen?

To address all problems associated with the statement above, this work focused on the fabrication of a low-cost and highly sensitive fluorescence immunobiosensor. The immunobiosensor was fabricated with fluorescein-5-isothiocyanate (FITC) as a fluorophore loaded into silica nanoparticles for stability and reduction of fluorescence quenching. The prepared fluorescent FITC-doped silica nanoparticles were modified with polyclonal *anti*-PSA antibodies (*anti*-PSA-pAb) and used as sensing (signal generation). For the detection of PSA, *anti*-PSA monoclonal antibodies (*anti*-PSA-mAb) were used as capture antibodies on black microtiter plate and also bioconjugated onto nanomagnetic-silica nanoparticles. The immobilization of antibodies in this study was done in an oriented manner to expose the PSA binding site and enhance the sensitivity of the immunoassay. The signal generated using fluorescence was measured for intact nanoparticles and also dissolved nanoparticles for enhanced sensitivity.

1.3 Aim of thesis

The aim of this thesis is to prepare fluorescent FITC-doped silica antibody nanoparticles and nanomagnetic-silica nanoparticles for selective, specific, and ultrasensitive detection prostate-specific antigen (PSA) at ultra-low concentrations.

The specific objectives of the thesis were:

(i) To prepare FITC-doped silica nanoparticles (FITC@SiO_2NPs).

(ii) To optimize and compare between the 3.0% and 6.0% (w/w) FITC-dye loading into silica nanoparticles.

(iii) To characterize the prepared nanoparticles using various analytical methods such as Fourier Transform Infrared Spectroscopy (FT-IR), Zeta-potential, UV-Visible (UV-Vis) spectroscopy, Transmission electron microscopy (TEM), Proton nuclear magnetic resonance (^{1}H NMR), Energy-dispersive X-ray spectroscopy (EDS), and Fluorescence spectroscopy.

(iv) Surface functionalize FITC@SiO_2NPs with TES-prAmPBA to yield FITC@SiO_2-prAmPBANPs for oriented antibody bioconjugation.

(v) Bioconjugate polyclonal *anti*-PSA antibodies (*anti*-PSA-pAb) onto FITC@SiO_2-prAmPBANPs to yield FITC@SiO_2-prAmPBA-*anti*-PSA-pAb/glucose sensing nanobioconjugate.

(vi) To compare the intact and dissolution methods for the detection of PSA in both buffer and complex matrix (Newborn Calf Serum, NCS).

(vii) To synthesize nanomagnetic-silica antibody capture conjugates bioprobes (Fe_3O_4@SiO_2-prAmPBA-*anti*-PSA-mAb/glucose).

(viii) To characterize the synthesized nanomagnetic-silica nanoparticles using various analytical methods such as Fourier Transform Infrared Spectroscopy (FT-IR), Zeta-potential, UV-Visible (UV-Vis) spectroscopy, Transmission electron microscopy (TEM), Scanning electron microscopy (SEM), Proton nuclear magnetic resonance (^{1}H NMR), Energy-dispersive X-ray spectroscopy (EDS/X), X-ray diffraction (XRD), and Fluorescence spectroscopy.

(ix) To evaluate the analytical performance on the detection of PSA in the presence of both the nanomagnetic-silica nanoparticles and FITC-doped silica nanoparticles in serum matrix (Newborn Calf Serum, NCS).

1.4 Thesis outline

This thesis comprises of five chapters. Briefly, Chapter one - outlines the general introduction of the study, identifies gap in the research, and proposes the method for PCa detection using fluorescence detection, summarizes the thesis and the chapters. Chapter two - outlines a comprehensive background and literature review of the study. Chapter three - investigates the preparations of the fluorescence dye-doped silica nanoparticles and their bioconjugation with *anti*-PSA-pAb. Chapter four - investigates the use of nanomagnetic-silica nanoparticles as capture for dissolution fluorescence ELISA immunoassay. Chapter five - summarizes the study conclusions and proposes future perspectives.

Chapter 1: Justification and problem statement

This chapter describes the importance of developing sensitive systems for the early diagnosis, and monitoring of prostate cancer. The chapter also highlights the current diagnostic methods of prostate cancer and their limitations. It further explains the importance of the detection and screening of the PSA biomarker during carcinogenesis, to allow for accurate and sensitive diagnosis of prostate cancer (PCa). Further, outlines the use of biosensors for PSA detection using fluorescent nanoparticles and nanomagnetic silica nanoparticles. Lastly, the chapter also states the aims and objectives of the study and provides a brief outline of the thesis and highlights the different chapters in the study.

Chapter 2: Introduction and literature review

The chapter provides a comprehensive background of prostate cancer, which includes outlining the epidemiology and cause of prostate cancer, the risk factor leading to the development of prostate cancer, the stages of diagnosis of prostate cancer, and current diagnostic methodologies. The chapter also looks at the significance of prostate-specific antigen (PSA) as a diagnostic biomarker for prostate cancer screening, and monitoring. Furthermore, the chapter briefly describes the development of biosensors, the use of optical biosensors (fluorescent immunosensor systems), and the use of nanomaterials, such as silica nanoparticles and magnetic nanoparticles for analyte capture, signal transduction, and amplification using fluorescence immunosensors.

Chapter 3: Fluorescence dye-doped silica nanoparticles and the bioconjugation with *anti*-PSA-pAb for PSA detection

In this chapter, fluorescein-isothiocyanito-3-propyltriethoxysilane (FITC-APTES) precursor was successfully prepared and encapsulated into silica nanoparticles. The fluorescent silica nanoparticles were surface functionalized using triethoxysilanepropyl-3-amido phenylboronic acid (TES-prAmPBA) for oriented antibody immobilization of *anti*-PSA-pAb. The non-specific binding sites were blocked with glucose. The fluorescent silica nanoparticles were also optimized at altered 3.0% and 6.0% FITC-dye loadings and compared for signal amplification using NaOH in the intact and dissolution comparison studies. The dissolution route was used for the detection of PSA antigen both in buffer and serum matrix.

Chapter 4: Nanomagnetic silica nanoparticles as capture for dissolution fluorescence ELISA

In chapter four, nanomagnetic-silica nanoparticles were prepared by synthesizing oleic acid iron oxide nanoparticles and coated with a silica shell. Surface functionalization with triethoxysilanepropyl-3-amido phenylboronic acid (TES-prAmPBA) was achieved and bioconjugation of *anti*-PSA-mAb in an oriented manner. Glucose blocked boronic acids functional groups as non-specific binding sites. The nanomagnetic-silica as capture nanoprobes were used for PSA capture along with the FITC-doped silica nanoparticles for sensing. The PSA was detected using the dissolution route of the FITC-doped silica nanobioconjugates which resulted in fluorescence signal amplification. Further, a magnet was used to separate the capture nanobioprobes and fluorescence nanobioconjugates after immunocomplex formation in buffer and serum samples. This afforded the enhanced detection of PSA using the fluorescence signal generated.

Chapter 5: Conclusions and future perspectives

This chapter reports on the conclusions of this work and highlights the future perspectives.

1.5 References

[1] P. D’Orazio, Biosensors in clinical chemistry - 2011 update, Clin. Chim. Acta. 412 (2011) 1749–1761.

[2] G.M. Cooper, The Cell: A Molecular Approach, 2nd Edition, ASM Press, Sunderland (MA), 2000.

[3] L. Wu, X. Qu, Cancer biomarker detection: recent achievements and challenges, Chem. Soc. Rev. 44 (2015) 2963–2997.

[4] O.K. Adeniyi, P.N. Mashazi, Stable thin films of human P53 antigen on gold surface for the detection of tumour associated anti-P53 autoantibodies, Electrochim. Acta. 331 (2020) 135272.

[5] C. Mattiuzzi, G. Lippi, Current Cancer Epidemiology, J. Epidemiol. Glob. Health. 9 (2019) 217 - 222.

[6] F. Bray, M. Laversanne, E. Weiderpass, I. Soerjomataram, The ever-increasing importance of cancer as a leading cause of premature death worldwide, Cancer. 127 (2021) 3029–3030.

[7] F. Bray, J. Ferlay, I. Soerjomataram, R.L. Siegel, L.A. Torre, A. Jemal, Global cancer statistics 2018: GLOBOCAN estimates of incidence and mortality worldwide for 36 cancers in 185 countries, CA. Cancer J. Clin. 68 (2018) 394–424.

[8] H. Sung, J. Ferlay, R.L. Siegel, M. Laversanne, I. Soerjomataram, A. Jemal, F. Bray, Global Cancer Statistics 2020: GLOBOCAN Estimates of Incidence and Mortality Worldwide for 36 Cancers in 185 Countries, CA. Cancer J. Clin. 71 (2021) 209–249.

[9] R. Sankaranarayanan, Screening for Cancer in Low- and Middle-Income Countries, Ann. Glob. Heal. 80 (2014) 412-417.

[10] L.A. Torre, R.L. Siegel, E.M. Ward, A. Jemal, Global cancer incidence and mortality rates and trends - An update, Cancer Epidemiol. Biomarkers Prev. 25 (2016) 16–27.

[11] R.L. Siegel, K.D. Miller, A. Jemal, Cancer statistics, 2020, CA. Cancer J. Clin. 70 (2020) 7–30.

[12] V. Gubala, L.F. Harris, A.J. Ricco, M.X. Tan, D.E. Williams, Point of Care Diagnostics: Status and Future, Anal. Chem. 84 (2012) 487–515.

[13] Y.D. Zhu, J. Peng, L.P. Jiang, J.J. Zhu, Fluorescent immunosensor based on CuS nanoparticles for sensitive detection of cancer biomarker, Analyst. 139 (2014) 649–655.

[14] N.L. Henry, D.F. Hayes, Cancer biomarkers, Mol. Oncol. 6 (2012) 140–146.

[15] S. Naylor, Biomarkers: current perspectives and future prospects, Expert. Rev. Mol. Diagnostics. 3 (2003) 525–529.

[16] T.R. Rebbeck, K. Burns-White, A.T. Chan, K. Emmons, M. Freedman, D.J. Hunter, P. Kraft, F. Laden, L. Mucci, G. Parmigiani, D. Schrag, S. Syngal, R.M. Tamimi, K. Viswanath, M.B. Yurgelun, J.E. Garber, Precision Prevention and Early Detection of Cancer: Fundamental Principles, Cancer Discov. 8 (2018) 803–811.

[17] P. Rawla, Epidemiology of Prostate Cancer, World J. Oncol. 10 (2019) 63–89.

[18] S.K. Bechis, P.R. Carroll, M.R. Cooperberg, Impact of age at diagnosis on prostate cancer treatment and survival., J. Clin. Oncol. 29 (2011) 235–41.

[19] World Health Organization (WHO), Deaths by Cause, Age, Sex, by Country and by region, 2000-2019. WHO, (2020) 2000–2019.

[20] M.S. Litwin, H.J. Tan, The Diagnosis and Treatment of Prostate Cancer, JAMA. 317 (2017) 2532 - 2542.

[21] M. Nguyen-Nielsen, M. Borre, Diagnostic and Therapeutic Strategies for Prostate Cancer, Semin. Nucl. Med. 46 (2016) 484–490.

[22] J.L. Descotes, Diagnosis of prostate cancer, Asian J. Urol. 6 (2019) 129–136.

[23] F. Pinto, A. Totaro, A. Calarco, E. Sacco, A. Volpe, M. Racioppi, A. D’Addessi, G. Gulino, P. Bassi, Imaging in Prostate Cancer Diagnosis: Present Role and Future Perspectives, Urol. Int. 86 (2011) 373–382.

[24] H.X. Zhao, C.X. Xia, H.X. Yin, N. Guo, Q. Zhu, The value, and limitations of contrast-enhanced transrectal ultrasonography for the detection of prostate cancer, Eur. J. Radiol. 82 (2013) e641–e647.

[25] M.W. Farha, S.S. Salami, Biomarkers for prostate cancer detection and risk stratification, Ther. Adv. Urol. 14 (2022) 175628722211039.

[26] P. Song, B. Yang, Z. Peng, J. Zhou, Z. Ren, K. Fang, L. Yang, L. Wang, Q. Dong, Reduced cancer-specific survival of low prostate-specific antigen in high-grade prostate cancer: A population-based retrospective cohort study, Int. J. Surg. 76 (2020) 64–68.

[27] J. Meehan, M. Gray, C. Martínez-Pérez, C. Kay, D. McLaren, A.K. Turnbull, Tissue- and Liquid-Based Biomarkers in Prostate Cancer Precision Medicine, J. Pers. Med. 11 (2021) 664.

[28] H. Farahani, M. Alaee, J. Amri, M.-R. Baghinia, M. Rafiee, Serum and Saliva Concentrations of Biochemical Parameters in Men with Prostate Cancer and Benign Prostate Hyperplasia, Lab. Med. 51 (2020) 243–251.

[29] L.I. Stowell, L.E. Sharman, K. Hamel, An enzyme-linked immunosorbent assay (ELISA) for prostate-specific antigen, Forensic Sci. Int. 50 (1991) 125–138.

[30] B. Acevedo, Y. Perera, M. Ruiz, G. Rojas, J. Benítez, M. Ayala, J. Gavilondo, Development and validation of a quantitative ELISA for the measurement of PSA concentration, Clin. Chim. Acta. 317 (2002) 55–63.

[31] S. Sarkar, M. Gogoi, M. Mahato, A.B. Joshi, A.J. Baruah, P. Kodgire, P. Boruah, Biosensors for detection of prostate cancer: a review, Biomed. Microdevices. 24 (2022) 32.

[32] L.H. Pan, S.H. Kuo, T.Y. Lin, C.W. Lin, P.Y. Fang, H.W. Yang, An electrochemical biosensor to simultaneously detect VEGF and PSA for early prostate cancer diagnosis based on graphene oxide/ssDNA/PLLA nanoparticles, Biosens. Bioelectron. 89 (2017) 598–605.

[33] X.P. Liu, N. Chang, J.S. Chen, C.J. Mao, B.K. Jin, Ultrasensitive photoelectrochemical immunosensor based on a g-C_3N_4/SnS_2 nanocomposite for prostate-specific antigen detection, Microchem. J. 168 (2021) 106337.

[34] D. Mwanza, N. Mfamela, O. Adeniyi, T. Nyokong, P. Mashazi, Ultrasensitive detection of prostate-specific antigen using glucose-encapsulated nanoliposomes anti-PSA polyclonal antibody as detection nanobioprobes, Talanta. 245 (2022) 123483.

[35] M. Kim, K. Kim, J.H. Lee, A cost-effective and rapid aptasensor with chemiluminescence detection for the early diagnosis of prostate cancer, Microchem. J. 155 (2020) 104763.

[36] V. Velonas, H. Woo, C. Remedios, S. Assinder, Current Status of Biomarkers for Prostate Cancer, Int. J. Mol. Sci. 14 (2013) 11034–11060.

[37] S. Sharma, J. Zapatero-Rodríguez, R. O’Kennedy, Prostate cancer diagnostics: Clinical challenges and the ongoing need for disruptive and effective diagnostic tools, Biotechnol. Adv. 35 (2017) 135–149.

[38] D. Damborska, T. Bertok, E. Dosekova, A. Holazova, L. Lorencova, P. Kasak, J. Tkac, Nanomaterial-based biosensors for detection of prostate specific antigen, Microchim. Acta. 184 (2017) 3049–3067.

[39] Y. Chen, X. Guo, W. Liu, L. Zhang, Paper-based fluorometric immunodevice with quantum-dot labelled antibodies for simultaneous detection of carcinoembryonic antigen and prostate-specific antigen, Microchim. Acta. 186 (2019) 112.

[40] D. Liu, X. Huang, Z. Wang, A. Jin, X. Sun, L. Zhu, F. Wang, Y. Ma, G. Niu, A.R. Hight Walker, X. Chen, Gold Nanoparticle-Based Activatable Probe for Sensing Ultralow Levels of Prostate-Specific Antigen, ACS Nano. 7 (2013) 5568–5576.

[41] D. Wu, A.C. Sedgwick, T. Gunnlaugsson, E.U. Akkaya, J. Yoon, T.D. James, Fluorescent chemosensors: the past, present and future, Chem. Soc. Rev. 46 (2017) 7105–7123.

[42] B. del Rosal, D. Jaque, Upconversion nanoparticles for in vivo applications: limitations and future perspectives, Methods Appl. Fluoresc. 7 (2019) 022001.

Chapter 2

2 Introduction and literature review

This chapter provides a comprehensive background of prostate cancer and its epidemic on a global scale. The chapter also outlines the main causes and risk factors contributing to prostate cancer development. It further discusses the current diagnostic methods and their limitations in the medical field and provides the significance of prostate-specific antigen (PSA) as a clinical diagnostic biomarker for prostate cancer. The chapter also highlights the development of biosensors and immunoassays for the detection and quantification of PSA. The use of fluorescent immunobiosensors systems towards immunosensing of PSA are discussed. Lastly, the chapter describes the use of nanomaterials such as dye-doped silica nanoparticles for signal transduction and amplification, and magnetic nanoparticles for analyte capture, and magnetic separation.

2.1 Prostate cancer

Prostate cancer (PCa) is a type of cancer that occurs in the prostate found in the male reproductive system. The prostate is a small walnut-shaped gland located below the bladder (a hollow organ used to store urine) and in front of the rectum [1,2]. The prostate gland is responsible for the production of the alkaline prostatic fluid or seminal fluid that helps to nourish and transport sperm while keeping its lifespan longer [1–3]. Surrounding the prostate gland is the seminal vesicle (ejaculatory duct) and the urethra responsible for carrying urine and semen out of the body [1–3]. PCa is characterized as an adenocarcinoma, caused by the uncontrollable and abnormal growth of the prostate gland epithelial cells located in the tissue lining of the prostate gland [2–4]. Initially, PCa first materializes as a nodular swelling on the surface of the prostate gland and grows into a cancerous tumour or mass [1]. **Figure 2.1(a)** shows the pictorial representation of the position of the prostate gland in the reproductive system of men, and a comparison of the presence of the cancerous cell mass of an affected prostate gland against a normal gland [1]. PCa is also a multifocal disease, whereby numerous tumours can arise within a single patient [5]. About 80% of PCa diagnosed patients are found to have numerous tumours of different sizes within the prostate gland [5].

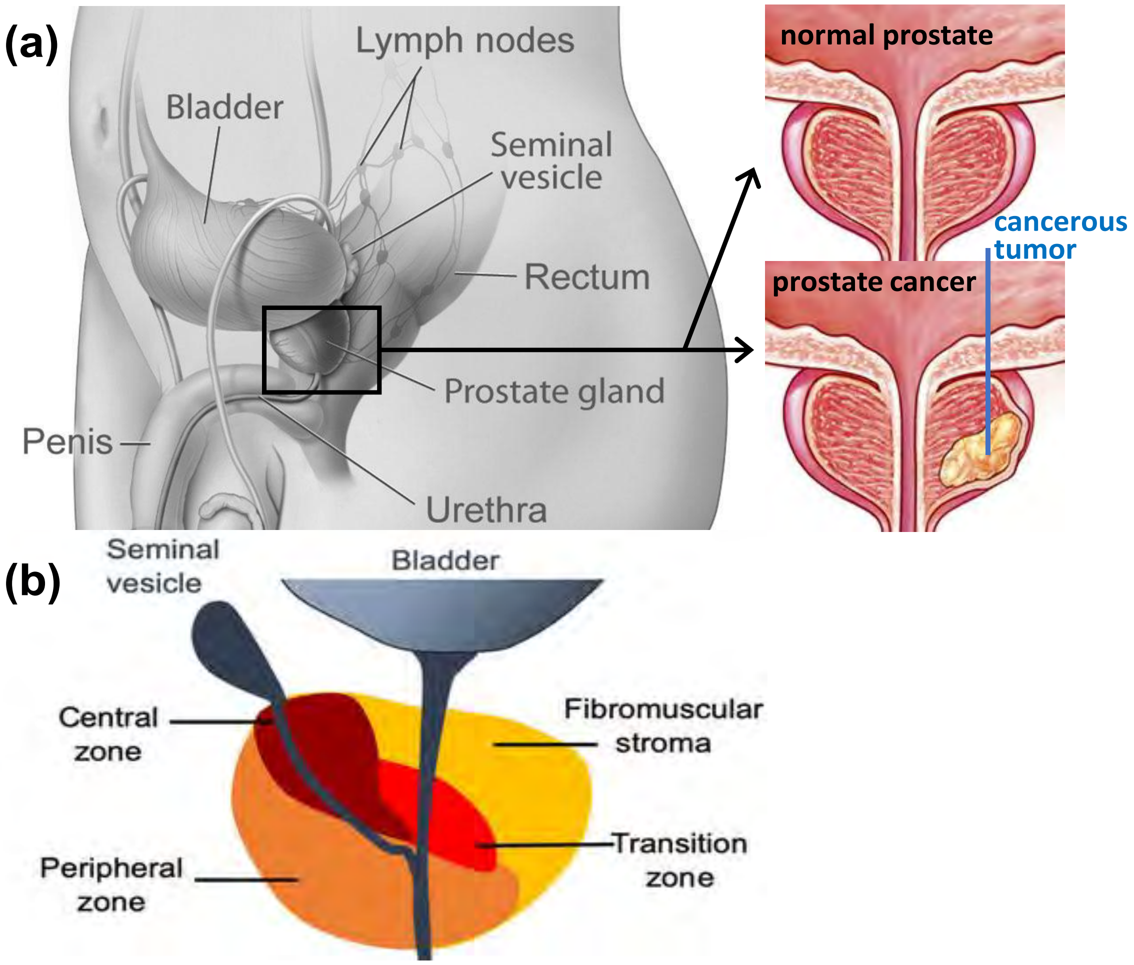

Figure 2.1: Pictorial representation of (a) the position of the prostate gland and the difference between a normal and cancer-affected prostate gland with a cancerous mass [1,6]. (b) A sagittal illustration of the anatomical position and zones of the prostate gland [7].

The average size of a man's prostate gland ranges from 28 to 47 cm^2 and is separated into four anatomic zones the central, peripheral, transition, and fibromuscular stroma [8]. **Figure 2.1(b)** shows the pictorial illustration of the anatomical positions and zones of the prostate gland. From **Fig. 2.1(b)**, the central zones surround the ejaculatory duct and comprise approximately 25% of the prostate volume [8,9]. The peripheral zones surround the central zone and the distal part of the prostatic urethra and account for about 75% of the prostate gland [8,9]. The transition zone is a small glandular zone located centrally, surrounds the urethra, and account for 10% of the normal prostate volume. The fibromuscular stroma which surrounds the inferior portion of the prostate called the apex contains the muscular and fibrous tissues [8,9]. Furthermore, tumours are characterized as either cancerous (malignant) or non-cancerous (benign) [5]. Benign tumour of the prostate can result due to benign prostate hyperplasia (BPH). BPH results due to enlargement of the prostate gland. This kind of mass development is localized (do not metastasize) and occurs at the transition zone of the prostate [8–11]. On the other hand, malignant tumours, the cancer cells develop initially at the peripheral zone of the prostate and spreads from the primary tumour site to other organs in the body (metastasizes) [8–12]. The metastatic PCa affects the close by organs such as the lymph nodes, bladder, and the urethra. The spreading of the tumour to the neighbouring body organs is characterized or diagnosed as late-stage prostatic cancer and this stage leads to poor survival rates and death [11,12]. PCa symptoms are similar to BPH at the early stages, and the current diagnostic methods only diagnose prostate cancer at late diagnosis (when a tumour has already formed) or misdiagnosis of BPH as PCa in patients [11,12]. Therefore, the development of a diagnostic system for early and accurate diagnosis of PCa is of paramount importance.

2.2 Epidemiology of prostate cancer

Globally, PCa remains the most frequently diagnosed malignant cancer in men and the second leading cause of cancer-related deaths after lung cancer [13,14]. According to the International Agency for Research on Cancer (IARC) and Global Cancer Statistics (GLOBOCAN), PCa has the highest number of incidence cases reported with about 1,4 million newly diagnosed cases and 375,000 prostate cancer-related deaths reported in 2020 [15,16]. Therefore, making PCa to account for more than 40% of cancer-related cases in men globally [17,18]. **Figure 2.2(a)** shows the global reported incidence and mortality rates of prostate cancer-related cases against other forms of cancer found in men in a total of 186 countries [15]. From **Fig. 2.2(a)**, PCa shows the highest number of reported cases in 113 countries and the second highest mortality rate in 47 countries. **Figure 2.2(b)** shows the incidence and mortality rates recorded (age standardized rate per 100,000) worldwide in 2020. From **Fig. 2.2(b)**, the African continent and the Caribbean countries showed higher mortality rates compared to Europe, America, and Asia. Furthermore, research reports showed that PCa incidences and mortality rates are increasing in less developed and low- to middle-income (economic) countries with a relative high death rate in men of African descents [19,20]. In Africa, PCa ranks higher in terms of morbidity and mortality [21]. According to the Global Cancer Statistics (GLOBOCAN), the age-standardized mortality rate (ASMR) of men due to PCa was recorded as Caribbean, 27.9 per 100,000; Middle Africa, 24.8 per 100,000; Eastern Africa, 16.3 per 1000,000; Western Africa, 20.2 per 100,000; Northern Africa, 8.2 per 100,000; and Southern Africa, 22.0 per 1000,000 as shown in **Fig. 2.2(b)** [15,16,19–23].

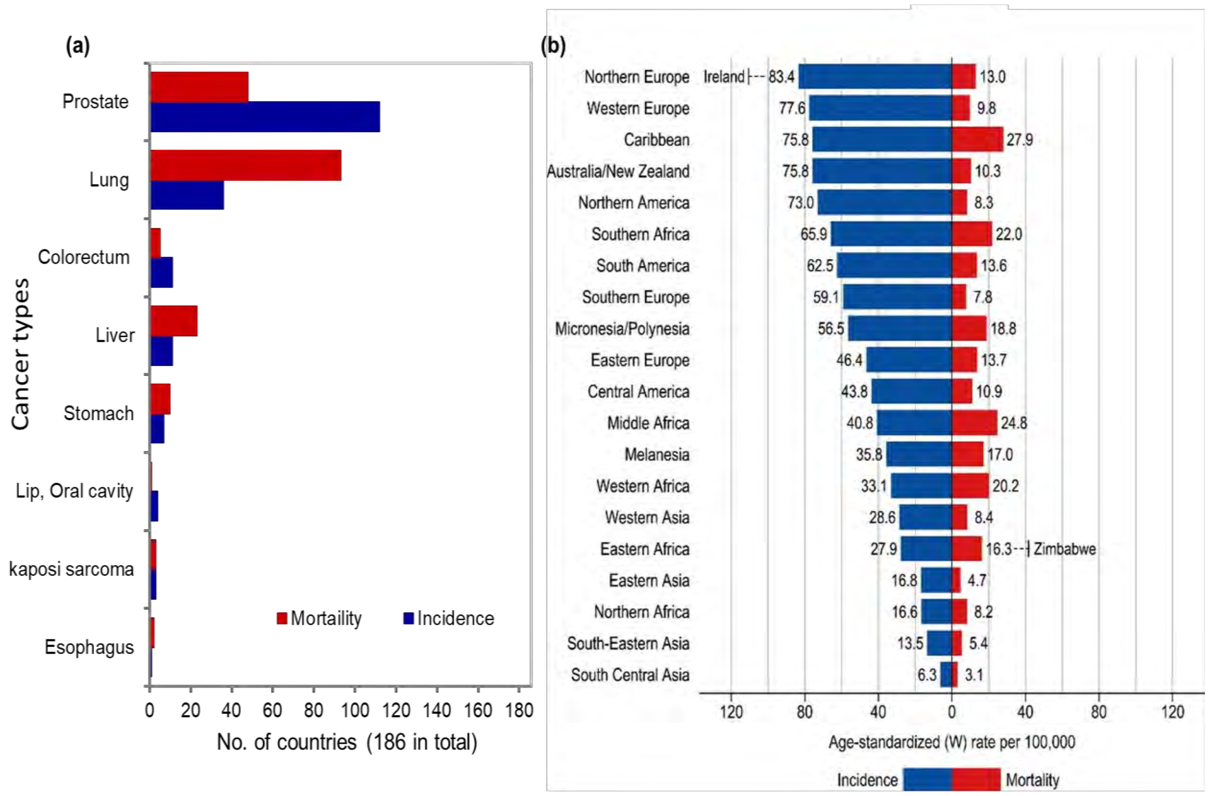

Figure 2.2: (a) Estimated incidence and mortality rates of common types of cancers found in males in the world (2020). (b) Pictorial representation of the global cancer patterns for both the incidence and mortality rate reported among men worldwide (0 to 85 years old). Source: IARC: GLOBOCAN, 2020 [15].

In most less developed and low-income (economic) countries, resources for PCa diagnosis are often limited, or inaccessible (non-existent). This leads to affected patient lacking timely treatments due to high costs of health facilities or limited treatment options, and results in high death rates being reported in those regions. Domestically, in South Africa, PCa is also the topmost diagnosed male cancer and the most common cancer among men in all provinces, with the Eastern Cape and Free State being the most affected areas [21,22,24]. According to the National Cancer Registry, 61.8 per 100,000 men are diagnosed with PCa and accounts for about 13.0% of males' deaths in South Africa [24,25]. Moreover, the global cancer observatory predicted that the incidence and mortality rates of PCa are to increase with approximately 1.7 million new cases and 499,000 deaths being reported by the year 2030 worldwide [26].

2.3 Etiology and Risk Factors

The main reason behind the cause of the onset of PCa carcinogenesis is unclear. However, several risk factors contribute to the increase in the chances of PCa development. The major etiological or risk factors for PCa are divided into two, that is the non-modifiable and modifiable risk factors. Non-modifiable risk factors are old age, race (ethnicity), family history, and inherited genetic changes. Modifiable risk factors are diet, physical inactivity, obesity, smoking, inflammation of the prostate (prostasis), sexually transmitted infections (STIs), environmental exposure, and surgical treatment (vasectomy) [27,28]. Higher PCa risks are relative to ageing, and older men are prone to develop PCa than younger men under 40 years old [27,29]. PCa is commonly diagnosed among elderly men (above the ages of 50 years old) [14,28–30]. Globally, about 34% of prostate cancer-related diagnosis are in men aged 50 and 70% in men aged 75 and above [2,31]. An increased number of the confirmed cases were observed in White men aged 50 years old or older and in Black men 40 years and older with or without family history of PCa [32]. However, some studies suggest that prostatic carcinogenesis is initiated earlier [33].

Race and ethnicity are other essential risk factors for PCa [32]. Several studies showed that PCa is more prominent among Black men. For example, African, Caribbean, South American, Indian, and African-American men are reported to have high incidence and mortality cases, and lower cases being prevalent across Asian, European, and White American men [14,27,32]. Some of the main causes were associated with both socioeconomic conditions and biological factors [26,32]. According to several studies, genetic predisposition was suggested as the root cause of PCa in men of different ethnicities. For example, the chromosome 8q24 variants, associated with an increased risk of PCa was observed to be prominent amongst Black men when compared to White men [34]. More studies have also shown that Black men, especially African-Americans have a high frequency of mutations in genes that control cell death like BCL2 [35] or inhibit malignancies EphB2 [36].

Family history and genetic changes have also been found to contribute to the development of PCa [2,37]. About 20% of patients with PCa have reported a family history of the disease, which is not only due to the shared genes but due to shared lifestyle choices and exposure to similar environmental carcinogens [37–39]. For example, families with a history of male relatives with PCa, the male children in the family have a higher risk of developing PCa [39]. Around 5% of PCa is attributed to an inherited genetic background [40]. The risks of developing PCa are also increased when high penetrance genetic “risk” alleles like BRCA1 and 2 mutations are inherited [41]. Men found to have inherited the BRCA1 and 2 mutated genes have clinically confirmed to develop an aggressive form of PCa [42].

Diet (high consumption of saturated animal fats and red meat), obesity, physical inactivity, and environmental exposure to chemical or ionization radiation also increased risk of PCa [27,43,44]. Saturated animal fat has shown a correlation between PCa mortality along with a high intake of meat, fat, and dairy products [44].

The studies reported, possibly due to a high intake of energy from meat and high fatty dietary meals, increased the basal metabolism and promoting prostate carcinogenesis via elevated androgen production [45]. Also, saturated animal fat intake promoted the growth of PCa cells by increasing the levels of androgen in the blood [46]. The over consumption of calcium (supplements) and milk (>2000 mg/day) also resulted in high chances of PCa, and this is due to calcium's key role in prostate carcinogenesis controlling the PCa cell growth and apoptosis [47]. Furthermore, obesity (a high fat diet) and lack of physical activities also contributed to elevated risks of prostate, breast, and colon cancers [46]. Lastly, environmental exposure to carcinogenic materials such as cadmium, agent orange (herbicides), and Bisphenol A (BPH, from food product containers) also increased the chances of PCa [48–51].

2.4 Stages of prostate cancer

PCa is one of the most asymptomatic cancers in oncology and is easily misdiagnosed for other prostatic diseases [1,52]. PCa is often slow growing, and some patients can be asymptomatic to signs of the cancer development for years [1,53]. The tumour growth mainly presses on the urethra and leads to a partial blockage of the flow of urine, leading to discomfort when urinating (common symptom) [52–54]. Moreover, PCa progression is grouped into four stages of carcinogenesis. The stages are classified based on the size of the tumour and the spread of the tumour as shown in **Figure 2.3**. The early stages include stages I and II. In stage I, the tumour is so small, and cannot be felt by a medical doctor during a physical examination [54]. In stage II, the tumour can be felt but has not metastasized from the tumour site in the prostate gland. Stage III (locally advanced stage), the PCa is identified by the spread of the tumour from the primary site to nearby tissues. Lastly, Stage IV (advanced stage), the tumour has spread outside the prostate gland into nearby organs and tissues such as the bladder, lymph nodes, bones, and urethra [54]. Therefore, the stages of PCa play an important role in efficient treatment, monitoring, and management of the disease.

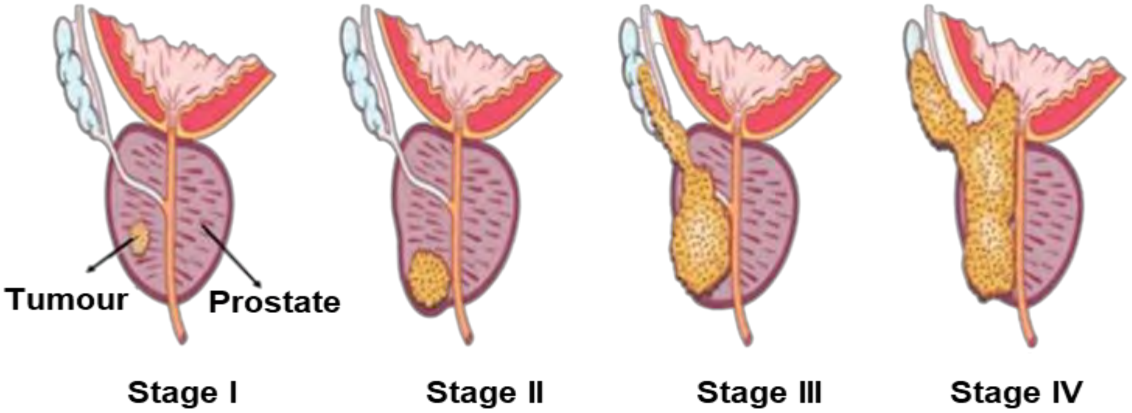

Figure 2.3: Illustration of the stages of prostate cancer based on the size and spread to nearby tissue and organs [54].

2.5 Diagnosis of prostate cancer

PCa is a major public health issue, and appropriate management of the disease is also a challenge as one in eight men are diagnosed with PCa [52–54]. However, the prognosis of PCa in its early stages of carcinogenesis makes it highly treatable. The initial symptoms of PCa may include weaker urine flow, discomfort after urinating or repeated urination or blood in urine or semen [52–55]. The primary diagnosis of PCa is done by the examination of the prostate. The most common methods of diagnosis of PCa include the digital rectum examination (DRE), tissue biopsy, magnetic resonance imaging (MRI), PET/CT-scans (ProstaScint scan), genomic testing, and blood test to measure the levels of prostate-specific antigen (PSA) [5,55–59]. DRE is a primary and common diagnostic method for the clinical examination of the prostate. A physical rectal examination procedure is conducted by an experienced doctor by inserting a gloved, lubricated finger into the rectum and feeling the presence of a tumour or mass in the surface of the prostate gland [5,58,59]. Tissue biopsy is also a very common procedure used to confirm the diagnosis and aggression (stage) of PCa, whereby a small tissue sample is removed from a patient's prostate gland [5,58]. Moreover, a transrectal ultrasound-guided needle biopsy (TRUS) is another method used for obtaining prostatic tissue. TRUS biopsies are used mainly on men with suspicious DRE results. TRUS allows for imaging of the prostate and seminal vesicles and is used to guide core needle biopsies through the rectum (transrectal biopsy), or the urethra (transurethral biopsy), or the area between the anus and scrotum (transperineal) to remove some tissue sample [60]. Then, the samples are examined under a microscope for identification of abnormal cell growth. Similarly, the genomic testing method is used to look for abnormalities in the DNA sequences of suspected cancerous tissue [5,41]. The MRI and PET/CT-scans are imagining methods used to scan and visualize the prostate and identify a tumour mass or spread of the tumour mass [57,58]. MRI is used to produce 3D images of soft tissues or infected organs of the human body but as compared with other techniques it is found to be superior. Similarly, PET/CT-scans are also imaged based techniques and primarily used to detect or locate a malignant PCa [57,58].

Overall, all these methods are invasive and give information about the tumour growth and the spread of PCa at advanced stages of development and leading to late response in diagnoses.

DRE alone is insufficient in detecting PCa, due to the high chances of misdiagnoses of PCa to BPH, and slight risk of bleeding with poor sensitivity (27.1%) and specificity (49.0%) [61–63]. Tissue biopsies (TRUS) are taken at random without targeting any cancers lesions, therefore making the methods prone to diagnostic errors [61–63]. Furthermore, both detection methods are associated with greater risks of patient infections [61–63]. On the other hand, PET/CT-scans are not sufficient for differentiating of PCa from BPH and are limited to detecting local recurrences and lymph node metastasis [63]. Meanwhile, the MRI as a diagnostic method is expensive and available only in sophisticated laboratories [63].

ELISA-blood test screening for prostate-specific antigen (PSA) is another commonly used sensitive method to detect many low and high-risk cancers. Furthermore, PSA is the most effective molecular biomarker available for the clinical detection and diagnosis of PCa. PSA is a serine protease (M.W 33 KDa) of the kallikrein family produced by the prostate [1,4,52,64–68]. It is a component of the seminal fluid necessary for ejaculation and is produced in both the normal and malignant prostate epithelial cells [64–67]. In healthy patients, the prostate releases small amounts of PSA into the blood system, and in the presence of a prostatic disease, the affected cells increase the release of PSA into the blood stream [64–67]. This is due to cell mutation and over-secretion of PSA from affected cells, leading to the cell membrane (a basal membrane) disruption, and the PSA leaking out into the bloodstream [68-70]. Generally, normal PSA levels in healthy patients range from 0 ng.mL^{-1} to 4.0 ng.mL^{-1}, and elevated levels of PSA increased above 4.0 ng.mL^{-1} could indicate the first stages of PCa. Levels greater than 10 ng.mL^{-1} results in the diagnosis of PCa [64–70]. Moreover, PSA is also found in saliva and urine [72,73]. In saliva, normal PSA levels are found between 3.0 pg.mL^{-1} to 340 pg.mL^{-1}. In urine samples, PSA levels above 1.7 ng.mL^{-1}, the patients are diagnosed with the suspicion of PCa [74].

Currently, a number of large automated high throughput immune analyzers are also used in the medical field. These analyzers are located in specialised laboratories to perform the majority of the PSA testing [75]. Some examples of these commercial immune analyzers are available for the quantification of PSA and they include they Roche Cobas® Core PSA Total enzyme immunoassay (EIA), Elecsys® total PSA, Simoa™ Total PSA (Quanterix™), Immulite 2000 XPI (Siemens Healthcare Diagnostics Inc.), ADVIA Centaur XPT (Siemens Healthcare Diagnostics Inc.), and ARCHITECT i2000SR (Abbott Diagnostics, Abbott Park, IL, USA). The immune analyzers provides advantages such as they are fully automated analysers with high throughput of samples, and providing results with lower limits of detection in ranges of 5.0 — 50 pg.mL^{-1} [75]. However, some of the limitations associated with the systems include lack of accessibility (only found in centralised laboratories) and not readily available in many communities and countries. Further, delays in samples transportation also contributes to the delays in the therapeutic turnaround time for patients (sometimes leading to late diagnosis) [75,76]. Moreover, at home-PSA lateral flow tests are also commercially available such as ‘PSA micro™’ from Pinnacle BioLabs and Novex Pharma from South Africa. However, the test systems are invasive, require a collection of 3-4 drops of blood, and exhibits lower sensitivity which results in numerous false negatives and high limits of detections ranging between 1.0 – 100 ng.mL^{-1} [75,76].

The use of PSA alone has been criticized for being non-specific, because in many asymptomatic patients mild to moderate levels of PSA can also be associated to benign conditions such as benign prostatic hyperplasia (BPH) or prostatitis [74–78]. However, as compared to other diagnostic methods, PSA remains a gold standard biomarker for PCa screening, diagnosis, monitoring, and management of PCa [5,79,80].

Several clinical diagnostic systems for the specific detection and quantification of PSA have been developed to improve the PSA tests for the early detection of PCa. These include biosensors [81] such as electrochemical immunosensors [82], colorimetric immunoassays [83,84], and dual-mode fluorescence immunosensors [85]. Reported colorimetric and electrochemical detection methods used enzyme-labelled antibodies with horseradish peroxidase (HRP), or alkaline phosphatase (ALP) as the detection probe. These studies involved the enzymatic conversion of o-phenylenediamine/H_2O_2, or 4-tert-butylcatechol (4-TBC)/H_2O_2, or tetramethylbenzidine/H_2O_2 substrates to obtain a colorimetric and/or electrocatalytic signal. Loss of enzymatic activity over time and instability of the enzymes under standard assay conditions are major disadvantages. The difficult, tedious labelling and purification procedures of the enzyme-antibody conjugates also reduce the sensitivity of the detection assay. Similarly, sensitivity issues were encountered in the dual-mode fluorescent and colorimetric immunosensor [85]. The fluorescence immunosensor uses a combination of a fluorophore linked to metal nanomaterials, which led to the quenching of the fluorescence signal through the energy transfer mechanism called Förster (fluorescence) resonance energy transfer (FRET) [85]. Therefore, the development of more reliable, low cost, and fast analytical methods for accurate detection and determination of PSA are of paramount importance. **Figure 2.4** shows different methods as discussed above in a summarized form.

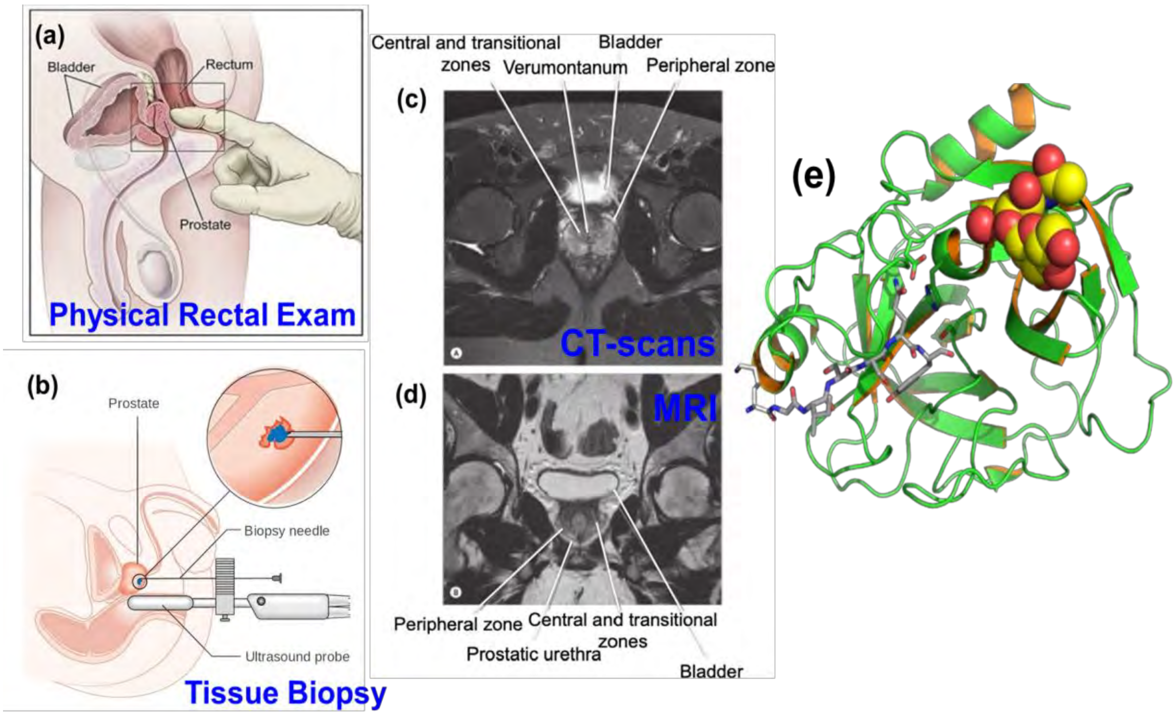

Figure 2.4: Traditional diagnostic methods for prostate cancer (PCa) (a) DRE, Transrectal ultrasound (TRUS) biopsy, (c) PET/CT-scan, and (d) MRI. (e) Single crystal X-ray structure of prostate-specific antigen (PSA) enzyme used in PSA screening [5,65,86,87].

2.6 Biosensors and immunobiosensors

Biosensors offer a wide range of applications in biotechnology, environmental protection, food industry, and medical diagnostics. Biosensors are fast, selective, and sensitive detection systems for various analytes like heavy metals (environmental monitoring), chemical warfare agents (bioterrorism), bacteria (contamination), tumour markers (cancer disease diagnosis), and cardiac biomarkers (cardiovascular diseases) [88]. According to the International Union of Pure and Applied Chemistry

(IUPAC), a biosensor is an analytical device that uses biochemical reactions to detect chemical compounds in biological samples usually by electrical, thermal, or optical signals [89]. It uses biorecognition or sensing elements such as enzymes, antibodies, nucleic acid, or biologically derived elements like aptamers, engineered proteins, and imprinted polymers to convert the concentration of the analyte (sample) into measurable signals using a transducer [88,90]. The analyte interacts with the bioreceptor or sensing element, and the signals are recorded by the transducers, and gives a quantitative or qualitative measure of the presence of the analyte [89,90].

Figure 2.5 shows the schematic representation of the components of the biosensors. Furthermore, biosensors are categorized based on the biorecognition elements (DNA biosensors) or transducer method used (electrochemical biosensors) and depending on the transducer technology (mass sensitive biosensors). Biosensors can produce electrochemical, optical, thermal, Microelectromechanical (MEMS), and piezoelectric signal outputs. Moreover, based on the biorecognition elements used, biosensors are also classified as enzymatic (containing an enzyme in the matrix), protein (using a protein in the receptor layer), nucleic (using DNA or RNA nucleic acids) biosensors, aptamer sensors, and immunobiosensors (where an antibody or antigen is used) [91,92].

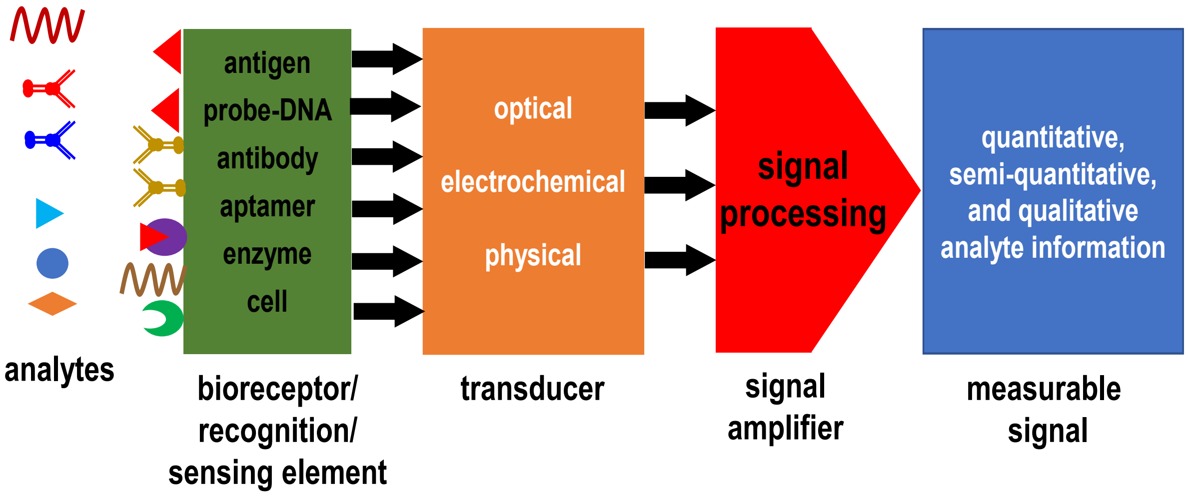

Figure 2.5: Schematic diagram representation of a biosensor outlining the principles and key components.

Immunobiosensors are a type of affinity-ligand based biosensors frequently used for clinical analyses and medical diagnosis [88]. Immunobiosensors use a biological recognition element such as antibodies or antigens to capture biologically relevant analytes like antigens or antibodies [93,94]. The biorecognition elements are interfaced or attached to a transducer for signal generation. The immunobiosensors use a specific reaction between an antibody (Ab) and an antigen (Ag) and employ a sandwich assay in the test design. The interaction between the antibody and antigen forms an immunocomplex reaction (sandwich interactions), and the interactions are translated into readable or measurable signals. The use of immunobiosensors offers advantages such as high sensitivity, specificity, selectivity, and low cost towards an analyte of interest, and rapid immunoassay results [93,94]. For the detection of PCa, biosensors and immunobiosensors have been explored due to the limitation of conventional diagnostic systems of PCa. The commercial methods of PCa diagnosis are not efficient or sensitive for the detection of PCa and are very expensive. Hence, the use of biosensors and immunobiosensors (immunoassay) is mostly due to their cost-effective, simple design, and can provide rapid results. This work investigates and discusses in detail the importance of optical biosensors and the use of fluorescence immunobiosensors for the detection and determination of PSA for early diagnosis of PCa.

2.6.1 Optical biosensors

Optical biosensors are of research interest in biotechnology, environmental studies, disease diagnosis, and medical field due to being cost effective and providing real-time, selective, rapid, highly specific, and sensitive measurements [95]. Optical biosensors are a unique set of biosensors which utilizes an optical measurement approach like absorption, reflectance, luminescence, or fluorescence for the direct detection of biological and chemical substances [95]. The biosensors utilize measurements based of the unique excitation and emission wavelengths specific to the target analyte and monitors optical changes resulting from the interactions between the biorecognition element (antibody/antigen) and analyte (antigen/antibody). Optical biosensors transducers are integrated to the biosensing element and the optical signals generated are correlated to the varying concentration of the analyte into readable measurements [95,96].

In addition, optical biosensors are classified based on two detection protocols as shown in **Fig. 2.6:**

(a) Sandwich or non-competitive (labeled) immunoassay detection protocol. In the sandwich or non-competitive immunoassay, a fluorescence probe is attached onto the detection antibody for signal generation. An analyte is captured, and a labeled detection antibody captured onto the analyte. The analyte is sandwiched between capture and labeled detecting antibody. The fluorescence signal due to the label is related to the analyte concentration.

(b) label-free or competitive immunoassay detection protocol. The fluorescence probe is attached onto the purified analyte. The sample containing the unlabeled analyte is mixed with the known concentration of the purified and labeled analyte. Both are then exposed to the capture antibody. The signal is then measured and related to the free analyte from the sample.

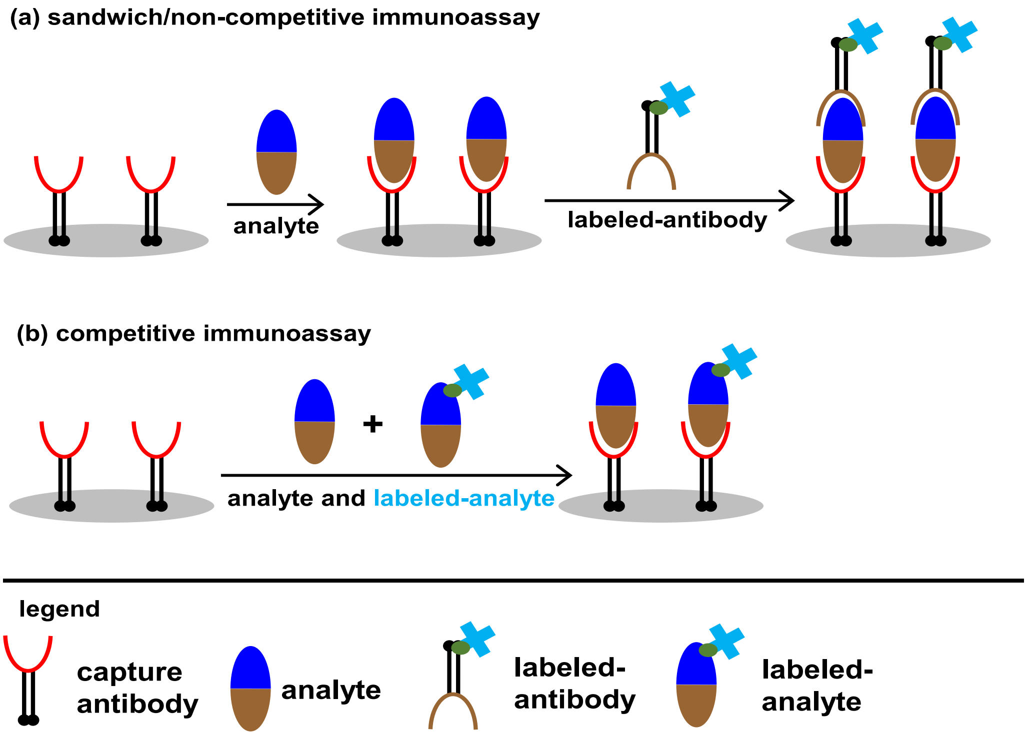

Figure 2.6: Principles of immunoassays of (a) fluorescence sandwich or non-competitive immunoassay and (b) competitive immunoassay protocols.

In label-based detection, the biosensor incorporates the fluorescence detection method, whereby the optical biosensors make use of a reporter molecule (fluorescent label/tag) and uses fluorescence emission to generate the optical signal for the detection of the analyte [95,96]. The intensity of the fluorescence is related to the concentration of the analyte of interest, and the strength between the interaction of analytes and the biorecognition elements. This detection method is extremely sensitive, selective, specific, and provides a dual confirmation of the analyte's presence, with reduced false positive readings, and results in low limits of detection [96,97]. Therefore, making optical fluorescence-based detection protocol an ideal detection method for accurate immunosensing for PSA and early diagnosis of PCa.

2.6.2 Fluorescence Immunobiosensors

Fluorescence is the most commonly used technique in optical biosensors. The fluorescence detection method is due to results of high single-molecular sensitivity, and the detectable analyte concentration is 10^6 times lower than other optical techniques, and provides immediate response [88]. Fluorescence immunobiosensors use the phenomenon of fluorescence for detection and signal generation. The phenomenon of the fluorescence properties can be described using a Jablonski diagram. Fluorescence is described when an irradiated molecule absorbs light and increases from a ground state to a singlet excited state. The excited molecules relax back to ground state through the process of fluorescence. During fluorescence, the light emitted by a molecule is of a longer wavelength compared to the absorbed light [98]. Fluorophores such as organic dyes (fluorescein, cyanine3, rhodamine, and aminoethylcoumarin), and inorganic fluorophores such as quantum dots (QDs) are commonly used in fluorescence studies. The fluorophores emit light at a longer wavelength and are used as detection fluorescent probes [98].

Figure 2.7 shows the Jablonski diagram illustrating the process involved in the creation of an excited state by optical absorption and fluorescence emission by a typical fluorescent probe. In detail, fluorescence occurs when a fluorophore is exposed to a light source (photons) and absorbs the energy of those photons of a specific wavelength and moves into an excited state (a higher level). In the excited state, the fluorophore undergoes conformational changes (interaction with the environment), and the fluorophore converts or transfers the energy and moves to a different energy state, or the energy is dissipated resulting in a relaxation of an excited state. Upon relaxation, the fluorophore emits a photon and moves back to the ground state (fluorescence emission) as shown in **Fig. 2.7**. The energy of emission or the emitted radiation is lower than that of the absorption (excitation energy) and has a longer wavelength due to the dissipation of the energy during the excited state lifetime. Furthermore, the energy and wavelength differences are known as Stokes shift and plays a significant role in the sensitivity of fluorescence immunobiosensors [88,99,100].

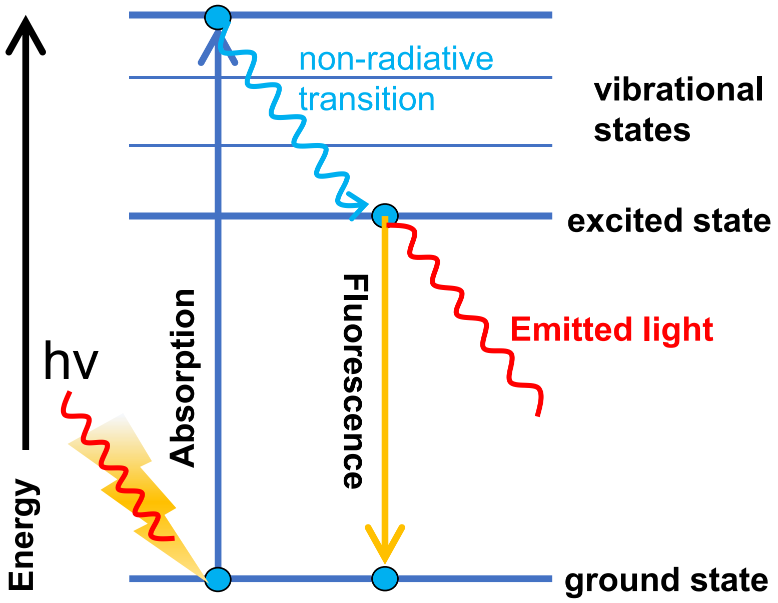

Figure 2.7: The Jablonski diagram (Jablonski, 1933) illustrating the principle of fluorescence emission of the fluorophore.

In that sense, fluorescence immunobiosensors are analytical devices that incorporate the use of fluorescence label for biomarker detection. Fluorescence immunobiosensors are frequently applied in analysis of biomolecules, especially those associated with various types of cancers due to the high affinity, sensitivity, and selectivity of fluorescence detection provided by the analyte-binding proteins (PSA) [88]. Furthermore, the fluorescence immunobiosensors are designed to use a sandwich immunoreaction format approach, which is a dual site immunoassay that occurs when the target analyte is bound to the capture antibody site, and then recognized by an antibody fluorescent bioconjugate as shown in **Fig. 2.6(a)**. In a sandwich configuration, an antigen is captured by primary antibody immobilized onto the surface and indirectly detects the bound antigens using a fluorescent labeled secondary antibody. Therefore, generating a fluorescence signal proportional to the number or concentration of antigens in the sample. **Figure 2.8** shows an illustration of the typical sandwich fluorescence immunoreaction configuration between an antibody and antigen (disease biomarker) and shows the formation of a capture antibody-antigen-antibody/fluorophore sandwich structure. In a fluorescence-based immunobiosensors, the principle of mechanism is the conversion of the biomarker response into a fluorescent signal, and organic fluorophores are commonly used as signal transduction tools for increased sensitivity towards PSA sensing [88,100].

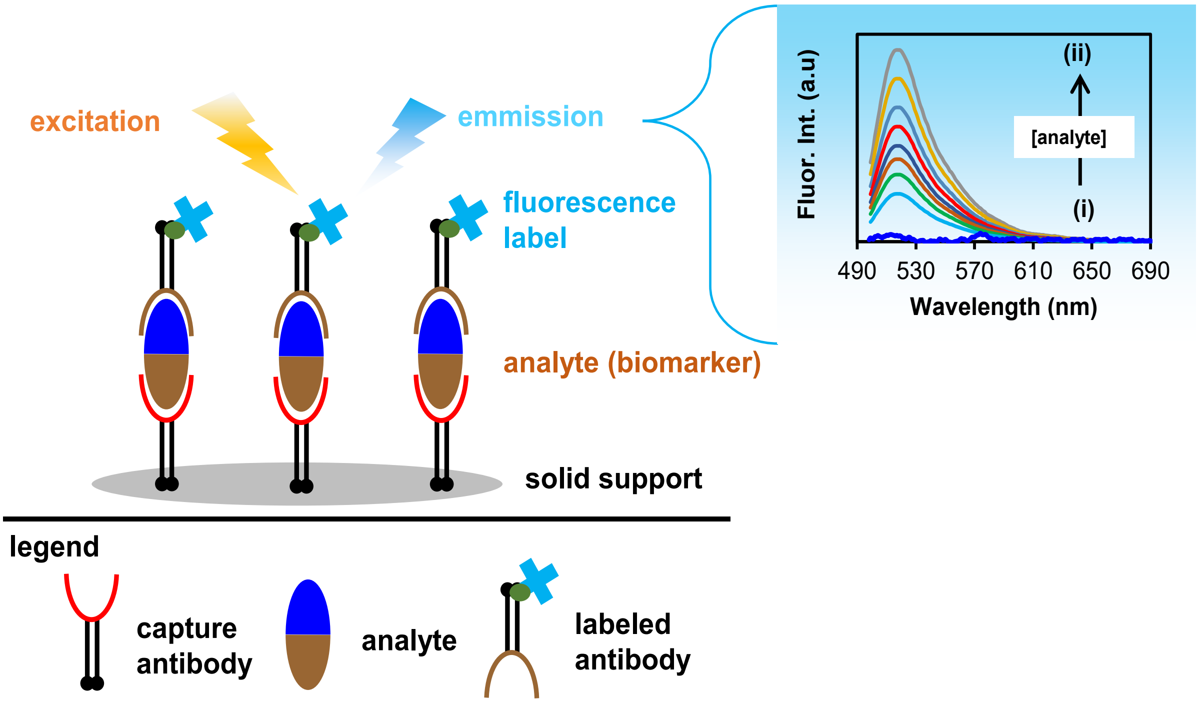

Figure 2.8: Diagram illustrating the sandwich immunoassay mechanism of a fluorescence-based immunobiosensors.

2.6.3 Fluorescent-based nanomaterials for immunosensing application

Fluorescence-based detection method has been widely used in modern biochemical research and diseases diagnosis [101]. Several studies have explored the use of fluorescence immunosensors for the detection of PSA. The immunosensors provide more sensitivity signals compared to clinical detection of PSA methods like enzyme-linked immunosorbent assay (ELISA) [97]. The research ranged from the use of enzyme-labelled antibodies with horseradish-peroxidase (HRP) or alkaline phosphatase (ALP) as the detection probes [102,103]. For example, a study by Li *et al*, [104] used silicon dioxide nanospheres loaded with horseradish peroxidase-lebelled secondary antibodies (HRP-Ab_2-SiO_2NSs) as the detection probes for PSA and the primary antibodies (Ab_1) immobilized on the walls of the microwell plates. In the presence of PSA, a sandwich-type immunocomplex was formed and composed of well/Ab_1<PSA<Ab_2-HRP. The fluorescence signal was obtained in the L-tyrosine and H_2O_2 systems [104]. However, the overall limitations of the studies included (i) tedious labelling and purification procedures (which reduced the sensitivity of the probe), and (ii) the instability of the enzyme under standard assay conditions which resulted in loss of enzymatic activity over time. Furthermore, organic fluorophores labeled antibodies are commonly used in fluorescence immunobiosensors because fluorophores are versatile and easy to use. Studies looked at the use of fluorescent organic dye molecules conjugated to antibodies such as cyanine-3, rhodamine, and fluorescein, used as fluorescence detection probes [105,106]. This is due to organic fluorophores advantages over enzymes such as higher extinction coefficient for high sensitivity and providing low limits of detection. However, organic fluorophores are prone to limitations such as poor photostability, and fluorescence quenching at high antibody-dye ratios [107,108]. These factors contribute to false-positive and false-negative signals.

To overcome such limitations several studies explored the use of nanoparticles-based detection systems incorporated for enhanced fluorescence and sensitive detection of

PSA [109]. Nanoparticles-based detection systems are advantageous due to characteristic such as unique optical properties and large surface-to-volume-ratio resulting in enhanced fluorescence signals, ease of surface modifications, and prolonged detection times (low photobleaching) [101]. These included the use of quantum dots (QDs) conjugated to antibodies as fluorescent probes which has proved popular in the construction of PSA immunosensors [110–112]. QDs present many advantages such as being ultrasmall, high fluorescence (brighter than organic fluorophores), photostable, tunable absorptions/emission, excellent quantum yield compared to organic dyes, and low limits of detection [101,112–114]. However, the toxicity of certain heavy materials like cadmium used in QDs syntheses are toxic and limit the use of QDs in biological systems [112–114]. Furthermore, the use of upconversion nanoparticles (UCNPs) and metal nanoparticles (i.e. gold nanoparticles) conjugated to fluorescent dyes were used [115,116]. However, upconversion nanoparticles (UCNPs) inherently suffered from low fluorescence and easily undergo quenching [117], and metal nanoparticles conjugated to fluorescent dye led to quenching of the fluorescence signals through Förster (fluorescence) resonance energy transfer (FRET) [112,118].

The use of 2D materials such as graphene nanostructures and graphene oxide (GO) or graphene quantum dots (GQDs) or MoS_2 nanosheets (MoO_3, $MoSe_2$) has also been explored in improving the sensitive detection of PSA. The studies employed the detection method of PSA through a dye quenching process “on” or “off” methods [119,120]. However, graphene requires tedious and energy intensive laborious procedures for synthesis. Therefore, nanocarrier platforms such as silica nanoparticles and nanoliposomes have been reported to overcome such limitations and drawbacks by reducing photobleaching, reducing fluorescence quenching upon bioconjugation with antibody, providing amplified fluorescence signals leading to highly sensitive detection of PSA at lower concentrations, and easy to prepare at low costs [102]. The work reported in this thesis investigates the use of fluorescent nanoprobes (sensing) and nanomagnets for capture, separation, and collection of the immunocomplex for amplified fluorescence detection and ultrasensitive detection of PSA.

2.7 Nanomaterial as carriers of the signal elements

The emergence of fluorescent nanomaterials as carriers for fluorescence immunosensors has enabled the development of ultrasensitive detection systems for cancer biomarkers. This was due to advantages such as low toxicity, ease in functionalization, biocompatibility, improved photostability resulting in enhanced sensitivity, selectivity through bioconjugates, and amplified fluorescence intensity [121]. Several research studies have shown the major use of nanostructures such as silica nanoparticles and liposomes for enhanced fluorescence signal generation, resulting in lower limits of detection [102,121–123]. Some examples include a study conducted by Zhao *et al* [122], which investigated the encapsulation of cadmium telluride quantum dots (CdTe-QDs) into silica nanoparticles (CdTe@SiO_2NPs) and used as carrier signal reporters for quantitative detection of PSA. Another inhouse study by Daniel *et al* [123] explored the use of nanoliposomes encapsulating glucose and bioconjugated with *anti*-PSA-pAb (GENLs-*anti*-PSA-pAb) for the ultrasensitive detection of PSA. In the detection systems ultra-low detections of PSA were achieved with limits of detections ranging from 53 fg.mL^{-1} to 3.0 pg.mL^{-1}. However, the toxicity of QDs limits their application in biosensors as these may denature the biological receptors if released as metalic ions. Similarly, the limitations for liposomal usage as nanocarriers includes the high cost of synthesis, low encapsulation efficiency for hydrophobic molecules (i.e. dyes), and short half-life as compared to the cheap synthesis of silica nanoparticles [124]. Fluorescent organic dye-doped silica nanoparticles have been extensively utilized in a broad range of fluorescent studies and biological applications due to their flexible chemistry, biocompatibility, and cheap synthesis [108,125].

2.7.1 Dye-doped silica nanoparticles

Fluorescent silica nanoparticles are commonly used in immunoassay, biosensing, and drug delivery research and have shown great results in immunodiagnostics and biomedical applications [108]. Dye-doped silica nanoparticles (DDSNs) have emerged as potential fluorescent silica nanoprobes adapted into a multitude of bio-applications that offer a higher fluorescent capability comparable to heavy metal QDs (classified as toxic) and nanoliposomes (classified as expensive) [108,124]. The incorporation of organic dyes into silica matrixes to form fluorescent dye-doped silica nanoparticles is of major research interest due to the cheap and simple chemistry for synthesis, excellent biocompatibility, and easy surface functionalization to couple to biomolecules [101,108,124]. The encapsulation of the dye molecules results in intense fluorescence signals 10,000 times brighter than fluorophores and the higher fluorescence intensity makes them suitable for ultrasensitive bioanalysis [101,108,124].

Dye-doped silica nanoparticles showed advantages over quantum dots, fluorescent dyes, up-converting nanoparticles (UCNPs) or plasmon resonant particles due to providing a higher quantum yield, photostability, size uniformity and tunability, and ease of surface modification with a variety of functional groups for oriented and random bioconjugation of antibodies (increases selectivity and specificity of the nanoparticles) [125,126]. The ability to couple various siloxane precursors with fluorescent dyes and incorporating the dyes into silica nanoparticles reduced dye leaching, improved the encapsulation efficiency (loading of dyes), photostability, amplified fluorescence upon release from the silica shells, and prolonged storage of the nanoparticles [108,126,127]. Moreover, fluorescein-5-isothiocyanate (FITC) is the most commonly prefered organic dye in fluorescent dye-doped silica nanoparticles for the detection of cancer biomarkers and bio-applications followed by cyanine (Cy3 or Cy5) and rhodamine [108,127–130].

2.7.2 FITC-doped silica nanoparticles

Fluorescent FITC-doped silica nanoparticles are employed as fluorescent nanoprobes in research for cancer biomarkers detection and related diseases [108]. Several research work reported includes work done in our research group by Omotayo *et al* [128] used fluorescent FITC-doped silica nanoprobes as an ultrasensitive detection system for anti-p53 autoantibodies (anti-p53aAbs). The research work showed excellent fluorescent sensitivity with ultra-low limits of detection in the pg.mL^{-1} ranges. Furthermore, a rapid fluorescence-based immunoassay study by Kasun *et al* [129] also used FITC-doped silica nanoparticles bioconjugated *Escherichia coli* antibody for the specific (single) detection of *E.coli* bacterial cells. From the study, an excellent sensitive fluorescent detection with low limits of detection towards *E. coli* bacterial cells was achieved [128,129]. Therefore, the studies indicated the intrinsic uses of the highly fluorescent FITC-doped silica nanoparticles advantages in bio-applications and bioanalysis. The use of FITC-doped silica nanoparticles (simple and cheap synthesis) for the ultrasensitive and selective immunobiosensing of ultra-low concentration of the PSA biomarker for early detection of PCa was investigated in this thesis.

2.7.3 Dye Overloading

The synthesis of optimally bright fluorescent silica nanoparticles is of importance in immunosensing. Optimal brightness of dye-doped silica nanoparticles depends on the concentration of the dye molecules loaded into the silica matrix [108]. Insufficient fluorophore loading into silica shell results in weaker brightness and false negative results upon detection of biological molecules [108]. However, fluorophore overloading also leads to fluorescence quenching due to Förster resonance energy transfer (FRET), fluorophore aggregation, and inner filter effects [108,131]. For example, fluorescein isothiocyanate (FITC) dye exhibits small stokes shift between the excitation and emission. Therefore, overloading of FITC-dye molecules into silica matrix results in close proximity of interactions between the FITC molecules leading to Highest Occupied Molecular Orbital-Förster Resonance Energy Transfer (HOMO-FRET) or self-quenching, and results in a reduced fluorescence intensity [131]. Hence, the work reported in the thesis also looked at the optimization of the prepared fluorescent silica nanoparticles at altered 3.0% and 6.0% concentrations of FITC-dye loading for optimal detection of PSA.

2.7.4 Nanomaterials as separators and collectors

Magnetic characteristics are present in transition metals such as Iron (Fe), cobalt (Co), and nickel (Ni) and their oxides [132]. However, magnetic iron oxides (Fe_3O_4NPs) and magnetic beads (MBs) are commonly employed in biomedical applications due to their outstanding characteristics such as superparamagnetism (magnetic property), low-cost synthesis, easily separated using a magnet, biodegradable, and large surface area that makes them biocompatible [133,134]. Magnetic nanoparticles (MNPs) can be functionalized with biological molecules that provide selectivity and are employed as capture probes to allow for the biorecognition of targets analytes with great efficiency [135]. MNPs are used to separate immunocomplexes formed, allowing for signal enhancement, bioassy repeatability, and results in high sensitivity, and lower detection limits especially when detecting ultra-low amounts of target analytes [134-136]. However, bare magnetic nanoparticles are chemically unstable, aggregate, and are susceptible to air oxidation, resulting in loss of magnetic properties [134,135]. To overcome these limitations, functionalization of MNPs is vital to their performance and applications by improving their stability and reducing aggregation [135]. For example, surface coating with inorganic materials like silica (SiO_2) is a widely used coating material due to its biocompatibility, hydrophilicity, reactivity with biological ligands, helps prevent the agglomeration, and improves the collodial stability of the nanoparticles. Thus producing interesting nanomagnetic-silica nanoparticles (Fe_3O_4@SiO_2NPs) [135,136].

2.7.5 Nanomagnetic-silica nanoparticles

Nanomagnetic-silica nanoparticles ($Fe_3O_4@SiO_2$NPs) have seen popular use in biodetection systems for ultrasensitive sensing and are advantageous because the sensitivity of the system can be increased using an external magnetic field [137]. Nanomagnetic-silica nanoparticles are magnetic nanoparticles consisting of a thin silica shell which acts as a scaffold for attachment of different functional groups [135,137]. They are advantageous for use in biodetection due to their facile synthesis, small sizes, stability, low toxicity, good monodispersity and excellent magnetic properties [135,137]. Moreover, the silica shell allows for surface functionalization, and attachment of organic molecules, ligands, and serves as the anchoring location for bioconjugates like antibody or protein [135-137]. Furthermore, other ligands are also used for surface functionalization which include and not limited to antibodies, aptamers, peptides, folate receptors, affibodies, and lectines [138]. In this thesis, nanomagnetic-silica nanoparticles were surface functionalized using boronic acid affinity ligands which allowed for a controlled molecular orientation of the monoclonal *anti*-PSA antibodies conjugation [135,137]. The bioconjugation with antibodies is advantageous in biomedical application such as in diagnostics and targeted therapy. This is due to their high specificty, selectivity in bioassay applications and allowing the antibody fucntionalized-$Fe_3O_4@SiO_2$NPs to act as caputre probes which are used for the isolation of the target analyte from complex matrices, enhances the effectiveness of analyte isolation and concentration, minimizes matrix effects due to simplified washing and separation procedures, allows faster assays kinetics, improves the sensitvity and limit of detection (LOD), and reduces the time for analysis [136-138].

Therefore, in this thesis, a cheap, simple, and ultrasensitive fluorescent system for the detection of PSA at low concentration was prepared using organic FITC-doped silica nanoparticles as sensing nanobioprobes and nanomagnetic-silica nanoparticles as capture bioprobes. The work also employed encapsulating FITC-dye into silica nanoparticles for improved photostability and reduced dye leaking. Further, altered FITC-dye loadings at 3.0% and 6.0% for enhanced fluorescence signals were investigated. Lastly, surface functionalization with boronic acid linker ligands for oriented bioconjugation to polyclonal *anti*-PSA sensing antibodies was employed to obtain high selectivity, specificity, and sensitivity towards PSA detection. Similarly, nanomagnetic-silica nanoparticles were surface modified also with boronic acid linker ligands and monoclonal *anti*-PSA capture antibodies for selectivity and specificity towards detection of PSA. Moreover, magnetic nanoparticles were employed and also used to enrich the immunocomplex formation using a magnet and amplifying the fluorescent signals, thus resulting in ultrasensitive detection of PSA at ultra-low concentrations.

2.8 References

[1] M.W. Dunn, M.W. Kazer, Prostate Cancer Overview, Semin. Oncol. Nurs. 27 (2011) 241–250.

[2] S. Belkahla, I. Nahvi, S. Biswas, I. Nahvi, N. Ben Amor, Advances and development of prostate cancer, treatment, and strategies: A systemic review, Front. Cell Dev. Biol. 10 (2022) 991330.

[3] M. Oelke, Physiology and Pharmacology of the Prostate, in: Urol. Princ. Pract., Springer International Publishing, Cham, 2020: pp. 127–150.

[4] W.G. Nelson, E.S. Antonarakis, H.B. Carter, A.M. De Marzo, T.L. DeWeese, Prostate Cancer, in: Abeloff's Clin. Oncol., Elsevier, 2020: pp. 1401-1432.e7.

[5] C. Tonry, S. Finn, J. Armstrong, S.R. Pennington, Clinical proteomics for prostate cancer: understanding prostate cancer pathology and protein biomarkers for improved disease management, Clin. Proteomics. 17 (2020) 41.

[6] M.D. Mitchell Humphreys, Prostate Cancer, Mayo Clin. Press. (2022). (Accessed August 23, 2023).

[7] A.K. Sauer, H. Vela, G. Vela, P. Stark, E. Barrera-Juarez, A.M. Grabrucker, Zinc Deficiency in Men Over 50 and Its Implications in Prostate Disorders, Front. Oncol. 10 (2020) 1293.

[8] O. Singh, S.R. Bolla, Anatomy, Abdomen and Pelvis, Prostate, 2023.

[9] J.C. Applewhite, B.R. Matlaga, D.L. Mccullough, M.C. Hall, Transrectal Ultrasound and Biopsy in the Early Diagnosis of Prostate Cancer, Cancer Control. 8 (2001) 141–150.

[10] Singapore Urological Association Clinical Guidelines for Male Lower Urinary Tract Symptoms/Benign Prostatic Hyperplasia, Singapore Med. J. 58 (2017) 473–480.

[11] L. Aaron, O.E. Franco, S.W. Hayward, Review of Prostate Anatomy and Embryology and the Etiology of Benign Prostatic Hyperplasia, Urol. Clin. North Am. 43 (2016) 279–288.

[12] N.J. Sathianathen, B.R. Konety, J. Crook, F. Saad, N. Lawrentschuk, Landmarks in prostate cancer, Nat. Rev. Urol. 15 (2018) 627–642.

[13] C. Mattiuzzi, G. Lippi, Current Cancer Epidemiology, J. Epidemiol. Glob. Health. 9 (2019) 217-222.

[14] P. Rawla, Epidemiology of Prostate Cancer, World J. Oncol. 10 (2019) 63–89.

[15] H. Sung, J. Ferlay, R.L. Siegel, M. Laversanne, I. Soerjomataram, A. Jemal, F. Bray, Global Cancer Statistics 2020: GLOBOCAN Estimates of Incidence and

Mortality Worldwide for 36 Cancers in 185 Countries, CA. Cancer J. Clin. 71 (2021) 209–249.

[16] F. Bray, J. Ferlay, I. Soerjomataram, R.L. Siegel, L.A. Torre, A. Jemal, Global cancer statistics 2018: GLOBOCAN estimates of incidence and mortality worldwide for 36 cancers in 185 countries, CA. Cancer J. Clin. 68 (2018) 394–424.

[17] D.C. Grossman, S.J. Curry, D.K. Owens, K. Bibbins-Domingo, A.B. Caughey, K.W. Davidson, C.A. Doubeni, M. Ebell, J.W. Epling, A.R. Kemper, A.H. Krist, M. Kubik, C.S. Landefeld, C.M. Mangione, M. Silverstein, M.A. Simon, A.L. Siu, C.-W. Tseng, Screening for Prostate Cancer, JAMA. 319 (2018) 1901 - 1913.

[18] K. Ito, Y. Fujizuka, K. Ishikura, B. Cook, Next-generation prostate-specific antigen test: precursor form of prostate-specific antigen, Int. J. Clin. Oncol. 19 (2014) 782–792.

[19] R. Marima, M. Mbeje, R. Hull, D. Demetriou, N. Mtshali, Z. Dlamini, Prostate Cancer Disparities and Management in Southern Africa: Insights into Practices, Norms and Values., Cancer Manag. Res. 14 (2022) 3567–3579.

[20] Y. Hamdi, I. Abdeljaoued-Tej, A.A. Zatchi, S. Abdelhak, S. Boubaker, J.S. Brown, A. Benkahla, Cancer in Africa: The Untold Story, Front. Oncol. 11 (2021) 650117.

[21] T.P. Seraphin, W.Y. Joko-Fru, B. Kamaté, E. Chokunonga, H. Wabinga, N.I.M. Somdyala, S.S. Manraj, O.J. Ogunbiyi, C.P. Dzamalala, A. Finesse, A. Korir, G. N'Da, C. Lorenzoni, B. Liu, E.J. Kantelhardt, D.M. Parkin, Rising Prostate Cancer Incidence in Sub-Saharan Africa: A Trend Analysis of Data from the African Cancer Registry Network, Cancer Epidemiol. Biomarkers Prev. 30 (2021) 158–165.

[22] M.O.A. Benedict, W.J. Steinberg, F.M. Claassen, N. Mofolo, The profile of Black South African men diagnosed with prostate cancer in the Free State, South Africa, South African Fam. Pract. 65 (2023) a5553.

[23] A. Cassell, B. Yunusa, M. Jalloh, M.M. Mbodji, A. Diallo, M. Ndoye, S.C. Kouka, I. Labou, L. Niang, S.M. Gueye, A Review of Localized Prostate Cancer: An African Perspective, World J. Oncol. 10 (2019) 162–168.

[24] T.M. Ramaliba, N. Sithole, A. Ncinitwa, N.I.M. Somdyala, Prostate Cancer Patterns and Trends in the Eastern Cape Province of South Africa; 1998–2017, Front. Public Heal. 10 (2022) 882586.

[25] C. Babb, M. Urban, D. Kielkowski, P. Kellett, Prostate Cancer in South Africa: Pathology Based National Cancer Registry Data (1986–2006) and Mortality Rates (1997–2009), Prostate Cancer. 2014 (2014) 1–9.

[26] H.E. Taitt, Global Trends and Prostate Cancer: A Review of Incidence, Detection, and Mortality as Influenced by Race, Ethnicity, and Geographic Location, Am. J. Mens. Health. 12 (2018) 1807–1823.

[27] N.R. Perdana, C.A. Mochtar, R. Umbas, A.R.A. Hamid, The Risk Factors of Prostate Cancer and Its Prevention: A Literature Review., Acta Med. Indones. 48 (2016) 228–238.

[28] P.H. Gann, Risk factors for prostate cancer., Rev. Urol. 4 Suppl 5 (2002) S3–S10.

[29] M. Nguyen-Nielsen, M. Borre, Diagnostic and Therapeutic Strategies for Prostate Cancer, Semin. Nucl. Med. 46 (2016) 484–490.

[30] G.G. Jha, V. Anand, A. Soubra, B.R. Konety, Challenges of managing elderly men with prostate cancer, Nat. Rev. Clin. Oncol. 11 (2014) 354–364.

[31] S.K. Bechis, P.R. Carroll, M.R. Cooperberg, Impact of Age at Diagnosis on Prostate Cancer Treatment and Survival, J. Clin. Oncol. 29 (2011) 235–241.

[32] I. Wu, C.S. Modlin, Disparities in prostate cancer in African American men: What primary care physicians can do, Cleve. Clin. J. Med. 79 (2012) 313–320.

[33] D.C. Miller, K.S. Hafez, A. Stewart, J.E. Montie, J.T. Wei, Prostate carcinoma presentation, diagnosis, and staging, Cancer. 98 (2003) 1169–1178.

[34] M.N. Okobia, J.M. Zmuda, R.E. Ferrell, A.L. Patrick, C.H. Bunker, Chromosome 8q24 variants are associated with prostate cancer risk in a high risk population of African ancestry, Prostate. 71 (2011) 1054–1063.

[35] D. Hatcher, G. Daniels, I. Osman, P. Lee, Molecular mechanisms involving prostate cancer racial disparity., Am. J. Transl. Res. 1 (2009) 235–48.

[36] C.M. Robbins, S. Hooker, R.A. Kittles, J.D. Carpten, EphB2 SNPs and Sporadic Prostate Cancer Risk in African American Men, PLoS One. 6 (2011) e19494.

[37] M.T. Vietri, G. D’Elia, G. Caliendo, M. Resse, A. Casamassimi, L. Passariello, L. Albanese, M. Cioffi, A.M. Molinari, Hereditary Prostate Cancer: Genes Related, Target Therapy and Prevention, Int. J. Mol. Sci. 22 (2021) 3753.

[38] S. Benafif, R. Eeles, Genetic predisposition to prostate cancer, Br. Med. Bull. 120 (2016) 75–89.

[39] L.N. Kolonel, D. Altshuler, B.E. Henderson, The multiethnic cohort study: exploring genes, lifestyle and cancer risk, Nat. Rev. Cancer. 4 (2004) 519–527.

[40] J. Ferrís-i-Tortajada, J. García-i-Castell, O. Berbel-Tornero, J.A. Ortega-García, Constitutional risk factors in prostate cancer, Actas Urológicas Españolas (English Ed. 35 (2011) 282–288.

[41] J.T. Zhen, J. Syed, K.A. Nguyen, M.S. Leapman, N. Agarwal, K. Brierley, X. Llor, E. Hofstatter, B. Shuch, Genetic testing for hereditary prostate cancer: Current status and limitations, Cancer. 124 (2018) 3105–3117.

[42] B.F. Darst, P. Wan, X. Sheng, J.T. Bensen, S.A. Ingles, B.A. Rybicki, B. Nemesure, E.M. John, J.H. Fowke, V.L. Stevens, S.I. Berndt, C.D. Huff, S.S. Strom, J.Y. Park, W. Zheng, E.A. Ostrander, P.C. Walsh, S. Srivastava, J. Carpten, T.A. Sellers, K. Yamoah, A.B. Murphy, M. Sanderson, D.C. Crawford, S.M. Gapstur, W.S. Bush, M.C. Aldrich, O. Cussenot, M. Yeager, G. Petrovics, J. Cullen, C. Neslund-Dudas, R.A. Kittles, J. Xu, M.C. Stern, Z. Kote-Jarai, K. Govindasami, A.P. Chokkalingam, L. Multigner, M.-E. Parent, F. Menegaux, G. Cancel-Tassin, A.S. Kibel, E.A. Klein, P.J. Goodman, B.F. Drake, J.J. Hu, P.E. Clark, P. Blanchet, G. Casey, A.J.M. Hennis, A. Lubwama, I.M. Thompson, R. Leach, S.M. Gundell, L. Pooler, L. Xia, J.L. Mohler, E.T.H. Fontham, G.J. Smith, J.A. Taylor, R.A. Eeles, L. Brureau, S.J. Chanock, S. Watya, J.L. Stanford, D. Mandal, W.B. Isaacs, K. Cooney, W.J. Blot, D. V. Conti, C.A. Haiman, A Germline Variant at 8q24 Contributes to Familial Clustering of Prostate Cancer in Men of African Ancestry, Eur. Urol. 78 (2020) 316–320.

[43] G. Markozannes, I. Tzoulaki, D. Karli, E. Evangelou, E. Ntzani, M.J. Gunter, T. Norat, J.P. Ioannidis, K.K. Tsilidis, Diet, body size, physical activity and risk of prostate cancer: An umbrella review of the evidence, Eur. J. Cancer. 69 (2016) 61–69.

[44] A. Kaiser, C. Haskins, M.M. Siddiqui, A. Hussain, C. D'Adamo, The evolving role of diet in prostate cancer risk and progression., Curr. Opin. Oncol. 31 (2019) 222–229.

[45] L. Arab, J. Su, S.E. Steck, A. Ang, E.T.H. Fontham, J.T. Bensen, J.L. Mohler, Adherence to World Cancer Research Fund/American Institute for Cancer Research Lifestyle Recommendations Reduces Prostate Cancer Aggressiveness Among African and Caucasian Americans, Nutr. Cancer. 65 (2013) 633–643.

[46] B. Bojková, P.J. Winklewski, M. Wszedybyl-Winklewska, Dietary Fat and Cancer - Which Is Good, Which Is Bad, and the Body of Evidence, Int. J. Mol. Sci. 21 (2020) 4114.

[47] K.M. Wilson, I.M. Shui, L.A. Mucci, E. Giovannucci, Calcium and phosphorus intake and prostate cancer risk: a 24-y follow-up study, Am. J. Clin. Nutr. 101 (2015) 173–183.

[48] J.K. Mullins, S. Loeb, Environmental exposures and prostate cancer, Urol. Oncol. Semin. Orig. Investig. 30 (2012) 216–219.

[49] C. Ledda, Cadmium exposure and prostate cancer insights mechanisms and perspectives, Front. Biosci. 23 (2018) 4667.

[50] N. Ansbaugh, J. Shannon, M. Mori, P.E. Farris, M. Garzotto, Agent Orange as a risk factor for high-grade prostate cancer, Cancer. 119 (2013) 2399–2404.

[51] M.C.R. Alavanja, Use of Agricultural Pesticides and Prostate Cancer Risk in the Agricultural Health Study Cohort, Am. J. Epidemiol. 157 (2003) 800–814.

[52] Roth-Kauffman MM, Prostate Cancer, Clin. Rev. (2011). (accessed December 23, 2023).

[53] S.H. Bradley, G. Funston, D. Jones, J. Watson, Diagnosing prostate cancer in asymptomatic patients, BMJ. (2022) e071076.

[54] Sunshine Coast Urology, What is Prostate Cancer? (2016) 1–2. (accessed August 23, 2023).

[55] J.L. Descotes, Diagnosis of prostate cancer, Asian J. Urol. 6 (2019) 129–136.

[56] M.S. Litwin, H.J. Tan, The Diagnosis and Treatment of Prostate Cancer, JAMA. 317 (2017) 2532 - 2542.

[57] F. Pinto, A. Totaro, A. Calarco, E. Sacco, A. Volpe, M. Racioppi, A. D'Addessi, G. Gulino, P. Bassi, Imaging in Prostate Cancer Diagnosis: Present Role and Future Perspectives, Urol. Int. 86 (2011) 373–382.

[58] M. Sekhoacha, K. Riet, P. Motloung, L. Gumenku, A. Adegoke, S. Mashele, Prostate Cancer Review: Genetics, Diagnosis, Treatment Options, and Alternative Approaches, Molecules. 27 (2022) 5730.

[59] A. Heidenreich, P.J. Bastian, J. Bellmunt, M. Bolla, S. Joniau, T. van der Kwast, M. Mason, V. Matveev, T. Wiegel, F. Zattoni, N. Mottet, EAU Guidelines on Prostate Cancer. Part 1: Screening, Diagnosis, and Local Treatment with Curative Intent—Update 2013, Eur. Urol. 65 (2014) 124–137.

[60] N. Borley, M.R. Feneley, Prostate cancer: diagnosis and staging, Asian J. Androl. 11 (2009) 74–80.

[61] O.T. Okotie, K.A. Roehl, M. Han, S. Loeb, S.N. Gashti, W.J. Catalona, Characteristics of Prostate Cancer Detected by Digital Rectal Examination Only, Urology. 70 (2007) 1117–1120.

[62] C. Gosselaar, M.J. Roobol, S. Roemeling, F.H. Schröder, The Role of the Digital Rectal Examination in Subsequent Screening Visits in the European Randomized Study of Screening for Prostate Cancer (ERSPC), Rotterdam, Eur. Urol. 54 (2008) 581–588.

[63] S. Sharma, J. Zapatero-Rodríguez, R. O'Kennedy, Prostate cancer diagnostics: Clinical challenges and the ongoing need for disruptive and effective diagnostic tools, Biotechnol. Adv. 35 (2017) 135–149.

[64] R.J. Rebello, C. Oing, K.E. Knudsen, S. Loeb, D.C. Johnson, R.E. Reiter, S. Gillessen, T. Van der Kwast, R.G. Bristow, Prostate cancer, Nat. Rev. Dis. Prim. 7 (2021) 9.

[65] N.L. Henry, D.F. Hayes, Cancer biomarkers, Mol. Oncol. 6 (2012) 140–146.

[66] U.H. Stenman, J. Leinonen, W.-M. Zhang, P. Finne, Prostate-specific antigen, Semin. Cancer Biol. 9 (1999) 83–93.

[67] E.A. Stura, B.H. Muller, M. Bossus, S. Michel, C. Jolivet-Reynaud, F. Ducancel, Crystal Structure of Human Prostate-Specific Antigen in a Sandwich Antibody Complex, J. Mol. Biol. 414 (2011) 530–544.

[68] L. Wu, X. Qu, Cancer biomarker detection: recent achievements and challenges, Chem. Soc. Rev. 44 (2015) 2963–2997.

[69] K. Jung, B. Brux, M. Lein, B. Rudolph, G. Kristiansen, S. Hauptmann, D. Schnorr, S.A. Loening, P. Sinha, Molecular Forms of Prostate-specific Antigen in Malignant and Benign Prostatic Tissue: Biochemical and Diagnostic Implications, Clin. Chem. 46 (2000) 47–54.

[70] H.J. Linton, L.S. Marks, L.S. Millar, C.L. Knott, H.G. Rittenhouse, S.D. Mikolajczyk, Benign Prostate-specific Antigen (BPSA) in Serum Is Increased in Benign Prostate Disease, Clin. Chem. 49 (2003) 253–259.

[71] V. Velonas, H. Woo, C. Remedios, S. Assinder, Current Status of Biomarkers for Prostate Cancer, Int. J. Mol. Sci. 14 (2013) 11034–11060.

[72] M.S. Khan, K. Dighe, Z. Wang, I. Srivastava, E. Daza, A.S. Schwartz-Dual, J. Ghannam, S.K. Misra, D. Pan, Detection of prostate specific antigen (PSA) in human saliva using an ultra-sensitive nanocomposite of graphene nanoplatelets with diblock- co -polymers and Au electrodes, Analyst. 143 (2018) 1094–1103.

[73] J.T. Kearns, D.W. Lin, Improving the Specificity of PSA Screening with Serum and Urine Markers, Curr. Urol. Rep. 19 (2018) 80.

[74] H. Farahani, M. Alaee, J. Amri, M.R. Baghinia, M. Rafiee, Serum and Saliva Concentrations of Biochemical Parameters in Men with Prostate Cancer and Benign Prostate Hyperplasia, Lab. Med. 51 (2020) 243–251.

[75] B. Srinivasan, D.M. nanus, D. Erickson, S. Mehta, “hughly poertable quntitative screening test for prostate-specific antigen at point of care”, Curr. Res. Biotechnol. 3 (2021) 288–299.

[76] K. Vaidyanathan, D.M. Vasudevan, Organ Specific Tumor Markers: What’s New?, Indian J. Clin. Biochem. 27 (2012) 110–120.

[77] H.J. Linton, L.S. Marks, L.S. Millar, C.L. Knott, H.G. Rittenhouse, S.D. Mikolajczyk, Benign Prostate-specific Antigen (BPSA) in Serum Is Increased in Benign Prostate Disease, Clin. Chem. 49 (2003) 253–259.

[78] J. Meehan, M. Gray, C. Martínez-Pérez, C. Kay, D. McLaren, A.K. Turnbull, Tissue- and Liquid-Based Biomarkers in Prostate Cancer Precision Medicine, J. Pers. Med. 11 (2021) 664.

[79] M.W. Farha, S.S. Salami, Biomarkers for prostate cancer detection and risk stratification, Ther. Adv. Urol. 14 (2022) 175628722211039.

[80] Y. Wu, Y. Wang, Z. Huang, Q. Liu, Recent advances in analysis technology for detection of prostate cancer biomarkers, Microchem. J. 190 (2023) 108740.

[81] D. Sadighbayan, K. Sadighbayan, M.R. Tohid-kia, A.Y. Khosroushahi, M. Hasanzadeh, Development of electrochemical biosensors for tumor marker determination towards cancer diagnosis: Recent progress, TrAC Trends Anal. Chem. 118 (2019) 73–88.

[82] S. Zhang, P. Du, F. Li, Detection of prostate specific antigen with 3,4-diaminobenzoic acid (DBA)–H_2O_2–HRP voltammetric enzyme-linked immunoassay system, Talanta. 72 (2007) 1487–1493.

[83] X.H. Pham, E. Hahm, K.-H. Huynh, B.S. Son, H.-M. Kim, B.H. Jun, Sensitive Colorimetric Detection of Prostate Specific Antigen Using a Peroxidase-Mimicking Anti-PSA Antibody Coated Au Nanoparticle, BioChip J. 14 (2020) 158–168.

[84] N. Xia, D. Deng, Y. Wang, C. Fang, S.J. Li, Gold nanoparticle-based colorimetric method for the detection of prostate-specific antigen, Int. J. Nanomedicine. Volume 13 (2018) 2521–2530.

[85] P.Y. You, F.C. Li, M.H. Liu, Y.H. Chan, Colorimetric and Fluorescent Dual-Mode Immunoassay Based on Plasmon-Enhanced Fluorescence of Polymer Dots for Detection of PSA in Whole Blood, ACS Appl. Mater. Interfaces. 11 (2019) 9841–9849

[86] P. D’Orazio, Biosensors in clinical chemistry - 2011 update, Clin. Chim. Acta. 412 (2011) 1749–1761.

[87] E.A. Stura, B.H. Muller, M. Bossus, S. Michel, C. Jolivet-Reynaud, F. Ducancel, Crystal structure of human prostate-specific antigen in a sandwich antibody complex, J. Mol. Biol. 414 (2011) 530–544.

[88] A. Kłos-Witkowska, The phenomenon of fluorescence in immunosensors., Acta Biochim. Pol. 63 (2016) 215 - 221.

[89] B. Jurado-Sánchez, Nanoscale Biosensors Based on Self-Propelled Objects, Biosensors. 8 (2018) 59.

[90] A. Koyun, E. Ahlatcolu, Y. Koca, Biosensors and Their Principles, in: A Roadmap Biomed. Eng. Milestones, InTech, 2012.

[91] S. Sarkar, M. Gogoi, M. Mahato, A.B. Joshi, A.J. Baruah, P. Kodgire, P. Boruah, Biosensors for detection of prostate cancer: a review, Biomed. Microdevices. 24 (2022) 32.

[92] N. Bhalla, P. Jolly, N. Formisano, P. Estrela, Introduction to biosensors, Essays Biochem. 60 (2016) 1–8.

[93] A. Victorious, S. Saha, R. Pandey, T.F. Didar, L. Soleymani, Affinity-Based Detection of Biomolecules Using Photo-Electrochemical Readout, Front. Chem. 7 (2019) 617.

[94] K.R. Rogers, Principles of Affinity-Based Biosensors, Mol. Biotechnol. 14 (2000) 109–130.

[95] P. Damborský, J. Švitel, J. Katrlík, Optical biosensors, Essays Biochem. 60 (2016) 91–100.

[96] A.K. Singh, S. Mittal, M. Das, A. Saharia, M. Tiwari, Optical biosensors: a decade in review, Alexandria Eng. J. 67 (2023) 673–691.

[97] S. Mehrabani, A. Maker, A. Armani, Hybrid Integrated Label-Free Chemical and Biological Sensors, Sensors. 14 (2014) 5890–5928.

[98] Y.H. Shin, M. Teresa Gutierrez-Wing, J.W. Choi, Review - Recent Progress in Portable Fluorescence Sensors, J. Electrochem. Soc. 168 (2021) 017502.

[99] David M. Jameson, Intoduction to Fluorescence, CRC Press Taylor & Francis Group, 2014.

[100] A.P. Das, P.S. Kumar, S. Swain, Recent advances in biosensor based endotoxin detection, Biosens. Bioelectron. 51 (2014) 62–75.

[101] L. Wang, K. Wang, S. Santra, X. Zhao, L.R. Hilliard, J.E. Smith, Y. Wu, W. Tan, Watching Silica Nanoparticles Glow in the Biological World, Anal. Chem. 78 (2006) 646–654.

[102] G. Perry, F. Cortezon-Tamarit, S.I. Pascu, Detection and monitoring prostate specific antigen using nanotechnology approaches to biosensing, Front. Chem. Sci. Eng. 14 (2020) 4–18.

[103] M. Kim, K. Kim, J.H. Lee, A cost-effective and rapid aptasensor with chemiluminescence detection for the early diagnosis of prostate cancer, Microchem. J. 155 (2020) 104763.

[104] L. Li, W. Zhang, Y. Wei, L. Yu, D. Feng, A Sensitive Fluorescent Immunoassay for Prostate Specific Antigen Detection Based on Signal Amplify Strategy of Horseradish Peroxidase and Silicon Dioxide Nanospheres, J. Anal. Methods Chem. 2022 (2022) 1–9.

[105] S. Vira, E. Mekhedov, G. Humphrey, P.S. Blank, Fluorescent-labeled antibodies: Balancing functionality and degree of labeling, Anal. Biochem. 402 (2010) 146–150.

[106] C.L. O’Connell, R. Nooney, C. McDonagh, Cyanine5-doped silica nanoparticles as ultra-bright immunospecific labels for model circulating tumour cells in flow cytometry and microscopy, Biosens. Bioelectron. 91 (2017) 190–198.

[107] D. Damborska, T. Bertok, E. Dosekova, A. Holazova, L. Lorencova, P. Kasak, J. Tkac, Nanomaterial-based biosensors for detection of prostate specific antigen, Microchim. Acta. 184 (2017) 3049–3067.

[108] V. Gubala, G. Giovannini, F. Kunc, M.P. Monopoli, C.J. Moore, Dye-doped silica nanoparticles: synthesis, surface chemistry and bioapplications, Cancer Nanotechnol. 11 (2020) 1.

[109] Z. Yin, L. Zhu, Z. Lv, M. Li, D. Tang, Persistent luminescence nanorods-based autofluorescence-free biosensor for prostate-specific antigen detection, Talanta. 233 (2021) 122563.

[110] X. Li, W. Li, Q. Yang, X. Gong, W. Guo, C. Dong, J. Liu, L. Xuan, J. Chang, Rapid and Quantitative Detection of Prostate Specific Antigen with a Quantum Dot Nanobeads-Based Immunochromatography Test Strip, ACS Appl. Mater. Interfaces. 6 (2014) 6406–6414.

[111] J. Wang, T.J. Mountziaris, Homogeneous immunoassays based on fluorescence emission intensity variations of zinc selenide quantum dot sensors, Biosens. Bioelectron. 41 (2013) 143–149.

[112] G. Annio, T.L. Jennings, O. Tagit, N. Hildebrandt, Sensitivity Enhancement of Förster Resonance Energy Transfer Immunoassays by Multiple Antibody Conjugation on Quantum Dots, Bioconjug. Chem. 29 (2018) 2082–2089.

[113] Y. Chen, X. Guo, W. Liu, L. Zhang, Paper-based fluorometric immunodevice with quantum-dot labeled antibodies for simultaneous detection of carcinoembryonic antigen and prostate specific antigen, Microchim. Acta. 186 (2019) 112.

[114] R. Lehner, X. Wang, S. Marsch, P. Hunziker, Intelligent nanomaterials for medicine: Carrier platforms and targeting strategies in the context of clinical application, Nanomedicine Nanotechnology, Biol. Med. 9 (2013) 742–757.

[115] T. Hao, X. Wu, L. Xu, L. Liu, W. Ma, H. Kuang, C. Xu, Ultrasensitive Detection of Prostate-Specific Antigen and Thrombin Based on Gold-Upconversion Nanoparticle Assembled Pyramids, Small. 13 (2017) 1603944.

[116] J.H. Choi, H.S. Kim, J.W. Choi, J.W. Hong, Y.K. Kim, B.K. Oh, A novel Au-nanoparticle biosensor for the rapid and simple detection of PSA using a sequence-specific peptide cleavage reaction, Biosens. Bioelectron. 49 (2013) 415–419.

[117] B. del Rosal, D. Jaque, Upconversion nanoparticles for in vivo applications: limitations and future perspectives, Methods Appl. Fluoresc. 7 (2019) 022001.

[118] P.Y. You, F.C. Li, M.H. Liu, Y.H. Chan, Colorimetric and Fluorescent Dual-Mode Immunoassay Based on Plasmon-Enhanced Fluorescence of Polymer Dots for Detection of PSA in Whole Blood, ACS Appl. Mater. Interfaces. 11 (2019) 9841–9849.

[119] R.M. Kong, L. Ding, Z. Wang, J. You, F. Qu, A novel aptamer-functionalized MoS2 nanosheet fluorescent biosensor for sensitive detection of prostate specific antigen, Anal. Bioanal. Chem. 407 (2015) 369–377.

[120] H. Pei, S. Zhu, M. Yang, R. Kong, Y. Zheng, F. Qu, Graphene oxide quantum dots@silver core–shell nanocrystals as turn-on fluorescent nanoprobe for ultrasensitive detection of prostate specific antigen, Biosens. Bioelectron. 74 (2015) 909–914.

[121] M. Holzinger, A. Le Goff, S. Cosnier, Nanomaterials for biosensing applications: a review, Front. Chem. 2 (2014) 63.

[122] Y. Zhao, W. Gao, X. Ge, S. Li, D. Du, H. Yang, CdTe@SiO$_2$ signal reporters-based fluorescent immunosensor for quantitative detection of prostate specific antigen, Anal. Chim. Acta. 1057 (2019) 44–50.

[123] D. Mwanza, N. Mfamela, O. Adeniyi, T. Nyokong, P. Mashazi, Ultrasensitive detection of prostate-specific antigen using glucose-encapsulated nanoliposomes anti-PSA polyclonal antibody as detection nanobioprobes, Talanta. 245 (2022) 123483.

[124] R. Taléns-Visconti, O. Díez-Sales, J.V. de Julián-Ortiz, A. Nácher, Nanoliposomes in Cancer Therapy: Marketed Products and Current Clinical Trials., Int. J. Mol. Sci. 23 (2022) 4249.

[125] R.P. Bagwe, L.R. Hilliard, W. Tan, Surface Modification of Silica Nanoparticles to Reduce Aggregation and Nonspecific Binding, Langmuir. 22 (2006) 4357–4362.

[126] X. Zhao, R.P. Bagwe, W. Tan, Development of Organic-Dye-Doped Silica Nanoparticles in a Reverse Microemulsion, Adv. Mater. 16 (2004) 173–176.

[127] L. Min, L. Zhao-Yue, L. Qiang, Y. Hang, M. Lan, L. Jing-Hong, B. Yu-Bai, L. Tie-Jin, Functionalized Fluorescein-doped SiO_2 Nanoparticles for Immunochromatographic Assay, Chinese J. Chem. 23 (2005) 875–880.

[128] O.K. Adeniyi, A. Ngqinambi, P.N. Mashazi, Ultrasensitive detection of anti-p53 autoantibodies based on nanomagnetic capture and separation with fluorescent sensing nanobioprobe for signal amplification, Biosens. Bioelectron. 170 (2020) 112640.

[129] P.D.K.P. Ananda, A. Tillekaratne, C. Hettiarachchi, N. Lalichchandran, Sensitive detection of E.coli using bioconjugated fluorescent silica nanoparticles, Appl. Surf. Sci. Adv. 6 (2021) 100159.

[130] S. Veeranarayanan, A. Cheruvathoor Poulose, S. Mohamed, A. Aravind, Y. Nagaoka, Y. Yoshida, T. Maekawa, D.S. Kumar, FITC Labeled Silica Nanoparticles as Efficient Cell Tags: Uptake and Photostability Study in Endothelial Cells, J. Fluoresc. 22 (2012) 537–548.

[131] G. Battistelli, A. Cantelli, G. Guidetti, J. Manzi, M. Montalti, Ultra-bright and stimuli-responsive fluorescent nanoparticles for bioimaging, WIREs Nanomedicine and Nanobiotechnology. 8 (2016) 139–150.

[132] J. Xu, J. Sun, Y. Wang, J. Sheng, F. Wang, M. Sun, Application of Iron Magnetic Nanoparticles in Protein Immobilization, Molecules. 19 (2014) 11465–11486.

[133] J. Wallyn, N. Anton, T.F. Vandamme, Synthesis, principles, and properties of magnetite nanoparticles for in vivo imaging applications—A review, Pharmaceutics. 11 (2019) 1–29.

[134] O. Adeniyi, S. Sicwetsha, A. Adesina, P. Mashazi, Immunoassay detection of tumor-associated autoantibodies using protein G bioconjugated to nanomagnet-silica decorated with Au@Pd nanoparticles, Talanta. 226 (2021) 122127.

[135] A. Adesina, O. Adeniyi, P. Mashazi, Nanomagnet Bioconjugates with anti -CRP Polyclonal Antibodies as Nanobioprobes for Enhanced Impedimetric Detection of CRP, Electroanalysis. 35 (2023) 120 - 130.

[136] K. Wu, J. Liu, V. K. Chugh, S. Liang, R. Saha, V. D. Krishna, M.C. Cheerran, J. Wang, Magnetic nanopaticles and magnetic particles spectroscopy-based bioassys: a 15 yearr recap, Nano. Futur. 6 (2022) 022001.

[137] L. Lu, X. Wang, C. Xiong, L. Yao, Recent advances in biological detection with magnetic nanoparticles as a useful tool, Sci. China Chem. 58 (2015) 793–809.

[138] S. Carinelli, M. Luis-Sunga, J. L. González-Mora, P. A. Salazar-Carballo, Synthesis and modification of magnetic nanoparticles for biosensing and bioassay application: A review. Chemosenr, 11 (2023) 533.

Chapter 3

3 Antibody fluorescence dye-doped silica nanobioconjugate for ultrasensitive detection of prostate specific antigen

Abstract

An ultrasensitive fluorescent silica nanobioprobe was modified with *anti*-PSA polyclonal antibodies (*anti*-PSA-pAb) for the detection of prostate-specific antigen (PSA). The fluorescent dye used was fluorescein-5-isothiocyanate (FITC). The *anti*-PSA-pAb was bioconjugated onto the surface of the FITC-doped silica nanoparticles using boronate ester. In the design, the FITC-APTES organosilane precursor was doped into the silica nanoparticles to form fluorescent silica nanoparticles (FITC@SiO_2NPs). The silica shell prevented dye leaching and promoted fluorescent signal amplification. Surface modification of the fluorescent silica nanoparticles was achieved by attaching triethoxysilanepropyl-3-amido phenylboronic acid (TES-prAmPBA) for oriented antibody immobilization. Optimization of the as-prepared fluorescent silica nanoparticles was investigated at altered 3% and 6% FITC-dye loadings. The fluorescent silica nanobioconjugates exhibited a strong excitation-dependent emission property with a strong emission at 518 nm and showed photostable properties over time. The fluorescent silica nanoparticles exhibited a dye retention of above 65% in the silica shell. The fluorescent nanobioconjugates' performance was evaluated using black 96-well microplates. A fluorescence sandwich-type immunoreaction was achieved via the antibody-antigen reaction of the FITC@SiO_2-prAmPBA-*anti*-PSA-pAb/glucose binding to the captured PSA analyte. NaOH was used for alkali hydrolysis of the sensing nanobioconjugates to release the FITC-APTES molecules, leading to fluorescence signal amplification. The proposed fluorescence immunobiosensor exhibited a linear relationship between the fluorescent

signals and the concentration of PSA obtained in the range of 2.0 pg.mL^{-1} to 50 ng.mL^{-1}, with limit of detection (LOD) of 0.70 pg.mL^{-1} and a limit of quantification (LOQ) of 2.12 pg.mL^{-1} in PBS buffer (pH 7.4). Following this protocol, the fluorescence immunobiosensor was prepared for the detection of PSA in spiked serum samples, and an LOD of 1.07 pg.mL^{-1} and a LOQ of 3.23 pg.mL^{-1} were calculated. Further, the proposed fluorescence immunoassay exhibited high selectivity and specificity for the detection of PSA. This method can be used for sensitive detection of prostate-specific antigen (PSA) in serum samples with no matrix interferences.

3.1 Introduction

Sensitive systems for prostate cancer (PCa) early diagnosis are in high demand due to poor prognosis and late diagnosis leading to increased mortality [1,2]. For example, the digital rectal exam (DRE), magnetic resonance imaging (MRI), and tissue biopsy are non-specific and diagnose prostate cancer at late stages of development when the tumour has formed and metastasized. [3–5]. Therefore, there is a need for early detection and diagnosis of prostate cancer before it metastasizes. Early and accurate diagnosis of PCa would allow for timely and effective chemotherapeutic treatment for the patient and this is of great importance [6–8]. The diagnosis of prostate cancer at an early stage requires detecting and quantifying low concentrations of the biomarkers produced during carcinogenesis (early stages of cancer development) [8–10]. The detection of prostate cancer biomarkers expressed at the early stages of carcinogenesis results in an increased survival rate and reduction in mortality rates amongst men [11,12]. The mutation of the human prostate-specific antigen (PSA) found at the early stages of prostate carcinogenesis results in abnormalities of cell growth in the prostate gland [13]. It serves as a reliable clinical biomarker for early diagnosis, screening, prognosis, monitoring, and prostate cancer recurrence [13–15]. Prostate-specific antigen (PSA), is an androgen-dependent glycoprotein serine protease (M.W 30-33 kDa) produced by prostate epithelial cells from the prostate gland into the seminal fluid [14–16]. Low concentrations of PSA are found in different molecular forms, such as uncomplexed free-PSA (fPSA), and complexed PSA (cPSA) that are bound to serine protease inhibitors called α-1-*anti*-chymotrypsin (PSA-ACT) in the bloodstream [13–18]. Clinical identification of PCa is measured as the total PSA (tPSA). Total PSA is the sum of both fPSA and cPSA found in the patient's serum or seminal fluid. During the early stages of PCa development, the tPSA levels are significantly increased in the serum of prostate cancer patients between 2.5 ng.mL^{-1} to 10 ng.mL^{-1} [17–19]. This is due to the cell's mutations and over-secretion of PSA, leading to the cell membrane disruption (a basal membrane), allowing for PSA to leak into the bloodstream [20,21].

ELISA PSA screening is the common method used for the diagnosis of prostate cancer [22–24]. Several clinical diagnostic systems for the detection and quantification of PSA have been developed to improve the PSA tests for the early detection of PCa. These include biosensors [25] such as electrochemical immunosensors [13,26], colorimetric immunoassays [27,28], and dual-mode fluorescence immunosensors [29]. Reported colorimetric and electrochemical detection methods used enzyme-labelled antibodies with horseradish peroxidase (HRP), or alkaline phosphatase (ALP) as the detection probe. These studies involved the enzymatic conversion of o-phenylenediamine/H_2O_2, or 4-tert-butylcatechol (4-TBC)/H_2O_2, or tetramethylbenzidine/H_2O_2 substrates to obtain a colorimetric and/or electrocatalytic signal. Loss of enzymatic activity over time and instability of the enzymes under standard assay conditions are major disadvantages. The difficult, tedious labelling and purification procedures of the enzyme-antibody conjugates also reduce the sensitivity of the detection assay. Similarly, sensitivity issues were encountered in the dual-mode fluorescent and colorimetric immunosensor [29]. The fluorescence immunosensor uses a combination of a fluorophore linked to metal nanomaterials, which led to the quenching of the fluorescence signal through the energy transfer mechanism called Förster (fluorescence) resonance energy transfer (FRET) [29].

Research in enzyme-free and fluorescence immunoassays has seen an increase in use for quantitative and qualitative analysis of PSA [30]. Most biosensors incorporate fluorophores which a distinct provide characteristics such as high extinction coefficients for high sensitivity, low limits of detection, and are easy to prepare at very low costs [31]. Many conventional fluorescence-based biosensors use fluorophore-labelled antibodies with quantum dots (QDs) [32–34], organic dyes [35,36], and up-conversion nanoparticles [37]. However, fluorophores experience inherent limitations such as poor photostability, cytotoxicity, low fluorescent intensity, and fluorescence quenching upon bioconjugation [38]. The traditional use of organic fluorophores (organic dyes) such as fluorescein, Cyanine-3, and rhodamine are environmentally friendly dyes that suffer from chemical instability and photobleaching over time [38,39]. Quantum dots (QDs) are chemically stable with high fluorescence intensity and less photobleaching compared to fluorescent dyes. However, QDs are classified as toxic due to the use of heavy metals such as cadmium (Cd) used for their preparations [38–40]. The encapsulation of fluorophores into nanostructures such as silica nanoparticles and liposomes has been reported to overcome such limitations [41–44]. Dye-doped nanostructures have been reported to show high photostability, reduced fluorescence quenching during bioconjugation, and an intense fluorescence signal upon dissolution [38,39,41–44]. However, dye overloading into the nanomaterials systems results in fluorescence quenching [41–46]. The dye molecules become too close, resulting in the phenomenon called HOMO-FRET (highest occupied molecular orbital-Förster resonance energy transfer) [46]. Hence, optimized fluorescent dye-loaded silica nanobioprobes is important. Fluorescent (fluorescein-5-isothiocyanate, FITC) dye-doped silica nanoparticles have emerged as potential fluorescent nanobioprobes for a multitude of fluorescence bio-applications. The dye-doped silica nanoparticles are favourable because of their good water solubility, biocompatibility, photostable characteristics, and high fluorescent signal [39,41–47].

In this chapter, we report the preparation of a highly fluorescent FITC-doped silica antibody nanoparticles (FITC@SiO_2NPs) as sensing nanobioconjugates. The FITC@SiO_2NPs are surface functionalized with phenylboronic acid conjugate for oriented attachment of the antibody. Therefore, the bioconjugation of polyclonal *anti*-PSA antibodies (*anti*-PSA-pAb) allowed for selective and sensitive detection of PSA. A simple ultrasensitive fluorescence immunobiosensor for the detection of PSA is investigated. NaOH dissolution was used to release fluorophores from the nanoparticles for signal amplification leading to enhanced sensitive detection of PSA (intact and dissolution studies). The use of FITC@SiO_2NPs was reported here for the detection of PSA for the first time according to our knowledge.

This chapter was set out to achieve the following objectives of the thesis

(a) Preparation of lysable fluorescent FITC-doped silica nanoparticles (FITC@SiO_2NPs).

(b) Optimisation of the as-prepared fluorescent silica nanoparticles at altered FITC-dye loading of 3.0% and 6.0% (for high loading).

(c) Immobilization of triethoxysilanepropyl-3-amido phenylboronic acid conjugate (TES-prAmPBA) onto FITC@SiO_2NPs surface to yield FITC@SiO_2-prAmPBANPs for oritented antibody bioconjugation.

(d) Bioconjugaton of polyclonal *anti*-PSA antibodies (*anti*-PSA-pAb) onto FITC@SiO_2-prAmPBANPs and non-specific binding sites blocked with glucose to yield FITC@SiO_2-prAmPBA-*anti*-PSA-pAb/glucose sensing nanobioconjugates.

(e) Detection of PSA using intact and dissolution studies of FITC@SiO_2-prAmPBA-*anti*-PSA-pAb/glucose in an ELISA immunobiosensor set up in both buffer solution and serum samples (Newborn Calf Serum, NCS).

3.2 Experimental

3.2.1 Materials and reagents

Fluorescien-5-isothiocyanate Isomer 1 (FITC, 90 %), (3-aminopropyl)triethoxysilane (APTES, 98 %), tetraethyl orthosilicate (TEOS, 99.9%), 4-carboxyphenylboronic acid, sodium chloride (NaCl), 4-(1,1,3,3-tetramethylbutyl)-phenyl polyethylene glycol (Triton X-100), sodium hydroxide (NaOH), N-hydroxysuccinimide (NHS), 1-ethyl-3-(3-dimethylaminopropyl) carbodiimide hydrochloride (EDC), sodium hydroxide (NaOH), Bovine serum albumin (BSA), disodium hydrogen phosphate (Na_2HPO_4), and sodium dihydrogen phosphate (NaH_2PO_4), were purchased from Sigma-Aldrich (USA). Sodium hydrogen carbonate ($NaHCO_3$), sodium carbonate anhydrous (Na_2CO_3), absolute ethanol (98.6 %, w/v), and D-glucose were purchased from SAARChem (South Africa). Deuterated dimethyl sulfoxide (d_6-DMSO) and cyclohexane (99.5 %) were purchased from Merck (Germany). Hexan-1-ol was purchased from B&M Scientific (South Africa). Ammonium hydroxide (NH_4OH, 25 % wt) was purchased from Minema Chemicals (South Africa). The Bradford reagent (for Bradford assay), polyclonal sheep *anti*-human prostate-specific antibody (*anti*-PSA-pAb, 7820-0154), monoclonal mouse *anti*-human prostate-specific antibody (*anti*-PSA-mAb, 7820-0370), and prostate-specific antigens (PSA) were purchased from Bio-rad Laboratory Ltd (USA). The serum samples were prepared using calf serum purchased from Sigma-Aldrich (USA). Ultra-pure water with a resistivity of 18 MΩ.cm (at 25°C) was obtained from a Milli-Q Water Purification System (Millipore Corp. Bedford, MA, USA) and was used for the preparations of aqueous solutions throughout the experiments. Coupling buffer used, phosphate buffer solution (PBS, pH 7.4, 10 mM) was prepared using 0.63 g disodium hydrogen phosphate (Na_2HPO_4), 0.06 g sodium dihydrogen orthophosphate (NaH_2PO_4) in 400 mL of ultra-pure Millipore water. Sodium carbonate buffer (pH 9.6, 10 mM) was prepared using 0.17g sodium bicarbonate ($NaHCO_3$) and 0.21g sodium carbonate (Na_2CO_3) in 200 mL of ultra-pure Millipore water. Washing buffer, (PBST, pH 7.4, 10 mM) was prepared using 1.2 g disodium hydrogen phosphate (Na_2HPO_4), 0.12 g sodium dihydrogen orthophosphate (NaH_2PO_4), and 100µL of Tween 20 in 100 mL of Ultra-pure Millipore water. All reagents and solvents in this study were of analytical grade and used as received from the supplier.

3.2.2 Equipment

Infra-red spectra were collected on a Perkin-Elmer Universal AT08-98-u98-R Sampling accessory spectrum 100 FT-IR spectrometer. UV-Vis spectroscopy analysis was acquired on a SHIMADZU UV-2550 spectrometer. Zeta potential was obtained with dynamic light scattering Malvern Zetasizer Nano series, Nano ZS90 series S equipped with a 633 nm He/Ne laser. ^{1}H NMR spectra analysis was recorded using a Bruker AVANCE 600 MHz NMR spectrometer in DMSO-d_6. Transmission electron microscope (TEM) micrographs were obtained using a Zeiss Libra 120 TEM operating at 80 kV accelerating voltage. Energy dispersive X-ray spectroscopy (EDS) elemental mapping was collected in a high vacuum on a Tescan Vega 2 Scanning Electron Microscopy (SEM) with a W-filament and EDS data was collected on an Oxford INCA Penta-FET-X3 Si(Li) detector, at 20 kV. Black Nuc 96-well Maxisorp microplates were used to obtain the fluorescence emission spectra for the detection studies. Fluorescence spectra were recorded using a Spectramax Multitude Spectrofluorometer and Synergy MX microplate reader.

3.2.3 Preparation of FITC-doped silica nanoparticles

3.2.3.1 Synthesis of fluorescein-isothiocyanito-3-propyltriethoxysilane (FITC-APTES) precursor, Scheme 3.1

The fluorescent silica precursor (FITC-APTES) was prepared following a reported method with some modifications [48]. FITC (5.3 mg, 13.5 μmol.L^{-1}) dissolved in dry ethanol (2.0 mL) was stirred at room temperature for 30 mins. APTES (60 μL, 0.26 mmol.L^{-1}) was added to the FITC ethanol solution. The reaction was followed using thin layer chromatography until reagents have reacted. The colour of the mixture turned from bright yellow to a darker orange. The mixture was stirred for 24 hours at room temperature in darkness (to prevent photobleaching). The ethanol was evaporated and the product dried in a desiccator overnight to obtain the FITC-APTES organosilane precursor. The FITC-APTES was obtained as an orange-yellowish crystal powder.

Yield: 80.1%. FT-IR [(ATR), τ_{max}/cm^{-1}]: 3175 (NH & OH), 1570 (C=S), (1103) O-Si-O; 1054 (Si-O-C), and 913 (Si-C). UV-Vis [λ (nm) log (ε)]: 492 (3.8). ^{1}H NMR (600 MHz, DMSO-d6) δ [ppm]: 1.05 (9 H, CH_3), 2.10 (8H, CH_2), 7.85 (6H, d, Ph), 8.52 (3H, d, Ph).

3.2.3.2 Synthesis of FITC-doped silica nanoparticles (FITC@SiO_2NPs)

The fluorescent FITC-doped silica nanoparticles were prepared using an in-house water-in-oil microemulsion method with some modifications [49]. The microemulsion solution was prepared by mixing n-hexanol (3.5 mL), cyclohexane (15.0 mL), Triton X-100 (3.2 mL), and water (1.5 mL). The solvent mixture was stirred for 20 min to form a stable microemulsion. FITC-APTES (2.68 mg, 6.75 mol), TEOS (0.60 mL, 2.70 mmol), and NH_4OH (0.060 mL, 1.50 mmol) were added to the microemulsion, and the solvent mixture was stirred at room temperature in the dark for 24 hours. Acetone (30.0 mL) was added to break the microemulsion and isolate the nanoparticles from the solution. Silica nanoparticles were collected by centrifugation and washed with a 1:1 mixture of ethanol/water with repeated sonication and centrifugation (3000 rpm, 5 min, three times) to remove unreacted reagents. The isolated yellow orange FITC@SiO_2NPs were dried at 40°C overnight in the oven. The FITC-APTES dye loadings to the microemulsion were achieved by adding 1.31 mg (3.0%, 3.37 μmol) and 2.63 mg (6.0%, 6.75 μmol) [49]. Other concentratons of FITC-APTES, which will result in lower than 3% or higher than 6%, will be investigated in future.

FT-IR [(ATR), τ_{max}/cm^{-1}]: 3287 (O-H), 1036 (Si-O-Si), 948 (Si-OH), 786 (Si-O). UV-Vis [λ (nm), log (ε)]: 495 (3.8).

3.2.4 Dye-leaking study

The dye leakage studies of the synthesized FITC-doped silica nanoparticles were monitored using the fluorescence spectrofluorometer measurements. The FITC@SiO_2NPs suspension (1.0 $mg.mL^{-1}$) was sonicated and the fluorescence intensity (I_o) of the suspension was measured. The suspension solution was centrifuged (3000 rpm, 5 min) and the fluorescence intensity of the supernatant solutions (I) was measured over time at 10 mins intervals. The amount of the dye retained in the silica matrix was defined as $1-(\frac{I}{I_o})$ as reported [44,45].

3.2.5 Photostability study

The photostability of the FITC-doped silica nanoparticles and photobleaching experiments were performed following a simple experiment. An aqueous solution of FITC (1.0 mg.mL^{-1}), FITC-APTES (1.0 mg.mL^{-1}), and FITC@SiO$_2$NPs (1.0 mg.mL^{-1}) was prepared and the fluorescence intensity was measured overtime. The suspensions were radiated under a 300 W xenon lamp for 50 min and fluorescence spectra recorded at 5 min intervals.

3.2.6 Effects of pH conditions

To evaluate the effects of pH conditions on the dissolution of FITC-doped silica nanoparticles, pH study experiments were performed. An aqueous suspension of FITC@SiO$_2$NPs (1.0 mg.mL^{-1}) were prepared into varying PBS buffer (10 mM) solutions ranging from pH 2.0 to 11.0 . Fluorescence measurements of the solutions were obtained.

3.2.7 Dye-loading study (3.0% and 6.0% w/w)

A dye-loading test was used to estimate the number of FITC-APTES molecules encapsulated per fluorescent silica nanoparticle. In the dye-loading experiment, an aqueous suspension of FITC@SiO$_2$NPs (1.0 mg.mL^{-1}) was sonicated for 10 min and incubated for 1 hour at 37^{o}C. Then, the ground state absorption and fluorescence emission spectra of the solution were measured before and after dissolution with

NaOH (1.0 mL, 10 mM). The absorption intensities and TEM sizes (diameter, d) of the silica nanoparticles were used to estimate the numbers of FITC-APTES molecules loaded in a per nanoparticle for each altered loading and were calculated as reported [46] and explained in section 3.3.5.5.

3.2.8 Fluorescence Quantum Efficiency

The fluorescence quantum efficiency studies of the as-prepared 3.0 and 6.0 (%, w/w) FITC-doped silica nanoparticles against the standard FITC dye were monitored using fluorescence measurements. A standard solution of FITC (1.0 $mg.mL^{-1}$) and an aqueous solution of FITC@SiO_2NPs (1.0 $mg.mL^{-1}$) at altered dye loadings were prepared and sonicated for 10 min. The absorption and fluorescence intensity (***I***$_o$) of the suspensions were measured. After, a solution of NaOH (1.0 mL, 10 mM) was added to the 3.0% and 6.0 % (w/w) FITC@SiO_2NPs suspensions and allowed to react for 30 min. The dissolution of FITC@SiO_2NPs occurred and released FITC molecules. FITC and FITC@SiO_2NPs after dissolution were measured. A linear calibration curve of the integrated fluorescence intensity (emission peak area) as a function of solution absorbance was obtained. The quantum yield measurements were obtained using the gradients and determined using **Equation (3.1)**.

$$\% \, \Phi_{NPs} = 100 \, (\Phi_{Fstd} \, x \, \frac{m_{NPs}}{m_{Fstd}} \, x \, \frac{{\eta^2}_{NPs}}{{\eta^2}_{Fstd}}) \qquad \textbf{(3.1)}$$

where Φ_{NPs} is the quantum yield of the nanoparticles, m_{NPs} and m_{Fstd} integrated fluorescence intensity slopes of the FITC@SiO_2NPs and the fluorescein standard Φ_{Fstd} (Φ_{Fstd}= 0.97), respectively. η_{NPs} and η_{Fstd} are the refractive indexes of the medium [50].

3.2.9 Boronic acid functionalization of FITC-doped silica nanoparticles

3.2.9.1 Synthesis of triethoxysilanepropyl-3-amido phenylboronic acid conjugate (TES-prAmPBA), Scheme S3.1

4-Carboxyphenylboronic acid (166 mg, 1.0 mmol) was added to the solution of EDC (31.0 mg, 0.20 mmol) and NHS (57.5 mg, 0.50 mmol) in dry ethanol (5.0 mL) and stirred for 15 min. APTES (0.5 mL, 2.0 mmol) was added dropwise into the solution. The reaction was followed using the thin layer chromatography until reagents completely reacted. The solution mixture was stirred further overnight at room temperature until TES-prAmPBA resulted, separated (centrifuged), washed with ethanol, and oven dried at 60°C. The product was obtained as a white precipitate. Yield 66 %.

FT-IR [(ATR), τ_{max}/cm^{-1}]: 3228 (OH), 3265 (NH), 1643 (C=O), 1260 (B-O), and 1063 (O-Si-O). ^{1}H NMR (600 MHz, DMSO-d_6) δ [ppm]: 0.78 (2H, $SiCH_2$), 1.25 (t, 9H, CH_3), 1.96 (2H, CH_2), 2.61 (2H, NCH_2), 4.10 (q, 6H, CH_2), 7.88 (d, 2H, H-Ph), 8.18 (d, 2H, H-Ph).

3.2.9.2 Boronic acid functionalization to form FITC@SiO_2-prAmPBANPs

FITC@SiO_2NPs (20.0 mg) were dispersed in ethanol (5.0 mL) under stirred for 20 min. TES-prAmPBA (40.0 mg, 0.10 mmol) in ammonium solution was added to the nanoparticle ethanol solution. The resulting solution was continuously mixed at room temperature overnight in the dark. The product, phenylboronic acid functionalized-silica nanoparticles (FITC@SiO_2-prAmPBANPs) was obtained after centrifugation as a dry product. It was washed several times with a 1:1 mixture of water/ethanol to remove unreacted reagents. The FITC@SiO_2-prAmPBANPs were dried for 48 hours in the dark.

FT-IR [(ATR), τ_{max}/cm^{-1}]: 3303 (NH & OH), 1647 (C=O), 1395 (B-O), 1062 (Si-O-Si), 949 (Si-O), and 785 (Si-OH). UV-Vis [λ (nm) log (ε)]: 495 (3.8).

3.2.9.3 Bioconjugation of *anti*-PSA-pAb onto FITC@SiO2-prAmPBANPs

The bioconjugation of *anti*-PSA-pAb onto FITC@SiO_2-prAmPBANPs was achieved via boronate ester bonds. The N-glycans on the Fc region of the anti-PSA-pAb reacted with the boronic acids of fluorescence nanoparticles. FITC@SiO_2-prAmPBANPs (2.0 mg) was dispersed in cold PBS buffer (2.0 mL, pH 7.4,10 mM) and stirred for 10 min. Polyclonal *anti*-PSA antibody (50 μL, 1.0 mg.mL^{-1}) was added to the solution. The mixture was kept at 4°C under continuous slow stirring and allowed to react for 6 hours. The *anti*-PSA-pAb bioconjugated FITC-doped silica nanoparticles were centrifuged and washed with 4°C cold PBS buffer (pH 7.4) to remove the unbound antibodies. The unreacted boronic acid sites were blocked by incubating the purified FITC@SiO_2-prAmPBA-*anti*-PSA-pAbNPs in 4°C cold PBS (pH 7.4) containing D-glucose solution (50.0 µg.mL^{-1}, 60 mg, 0.334 mmol). After 2 hours, the mixture was centrifuged and washed three times with 4°C cold PBS buffer (pH 7.4, 10 mM). This yielded *anti*-PSA-pAb/glucose modified FITC-doped silica nanobioconjugates, represented as FITC@SiO_2-prAmPBA-*anti*-PSA-pAb/glucose. FITC@SiO_2-prAmPBA-*anti*-PSA-pAb/glucose was suspended in PBS buffer (2.0 mL, pH 7.4, 10 mM) and kept at 4°C before use.

FT-IR [(ATR), τ_{max}/cm^{-1}]: 3348 (N-H), 1639 (amide I), 1580 (amide II), and 1322 (B-O). UV-Vis [λ (nm), log (ε)]: 495 (3.8).

3.2.9.4 Bradford assay for *anti*-PSA-pAb onto FITC@SiO$_2$-prAmPBANPs

The polyclonal antibody (*anti*-PSA-pAb) was covalently attached to the surface of the boronic acid functionalized FITC@SiO$_2$NPs.The bioconjugation of polyclonal *anti*-PSA antibodies onto FITC@SiO$_2$-prAmPBANPs was achieved through the affinity boronate ester reaction. The reaction targets the carbohydrate moiety of (N-glycan) on the Fc region of the *anti*-PSA polyclonal antibody. The glycosylation found in the Fc region of the antibody was used to react with the boronic functionalized FITC-doped silica nanoparticles to form cyclic ester bonds. Bradford assay was used as a quantitative colorimetric assay, to confirm the immobilization of the *anti*-PSA polyclonal antibodies (*anti*-PSA-pAbs). The *anti*-PSA-pAb in the bioconjugation solution before and after the reaction with the nanoparticles was measured. The FITC@SiO$_2$-prAmPBA-*anti*-PSA-pAbs after conjugation were centrifuged and the supernatant was used for protein determination. Bovine Serum Albumin (BSA) standard solutions and the supernatant obtained from FITC@SiO$_2$-prAmPBA-*anti*-PSA-pAbNPs were made to react with Bradford reagent at room temperature for 30 mins. UV-Vis spectra were used to follow the bioconjugation of the polyclonal *anti*-PSA antibodies.

3.2.10 Microwell modification and PSA detection, Scheme 3.2

The detection of PSA followed three steps, (1) attachment of *anti*-PSA-mAb as capture on the microplate and BSA to block for non-specific binding. (2) Capture of the PSA, and (3) reaction of PSA with fluorescence nanobioconjugates and detection using spectrofluorometer. The details are as follows:

3.2.10.1 Attachment of capture monoclonal antibody (*anti*-PSA-mAb)

For the positive control, the wells of the black 96-well microplates were modified with monoclonal *anti*-PSA antibodies (*anti*-PSA-mAb) as the capture antibody, following this method. *anti*-PSA-mAb (100 µL, 10.0 µg.mL^{-1}) diluted in sodium-bicarbonate buffer (pH 9.5) was added into the microwells, and incubated for 12 hours at 4°C. This resulted in the physical adsorption of *anti*-PSA-mAb onto the microwell. The modified wells were washed three times with washing buffer (PBST, pH 7.4) to remove loosely bound and adsorbed *anti*-PSA-mAb. For blocking of non-specific binding sites on the microwells, PBST blocking buffer (300 µL, pH 7.4, 10 mM) containing 2% BSA was incubated at room temperature for 3 hours. The modified wells were represented as well/*anti*-PSA-mAb/BSA. The modified *anti*-PSA-mAb/BSA wells were washed with PBST (pH 7.4) three times followed by a final rinse with PBS (pH 7.4). The negative control wells were modified with only PBST blocking buffer (300 µL, pH 7.4) containing 2% BSA.

3.2.10.2 Detection of PSA using FITC@SiO_2-prAmPBA-*anti*-PSA-pAb/glucose

A sandwich-type immunoassay protocol was used for PSA detection. For analyte capture, PSA (50 µL) in cold PBS buffer (pH 7.4, 10 mM) of varying concentrations was added to corresponding microplate wells. The microplate wells were incubated for

2 hours to yield well/*anti*-PSA-mAb/BSA>PSA. After the incubation period, the microplate wells were washed 3 times with 4°C cold PBS (pH 7.4) to remove unbound PSA antigens. For detection and sensing studies, the nanobioconjugates solution (FITC@SiO_2-prAmPBA-*anti*-PSA-pAb/glucose, 100 µL, 200 µg.mL^{-1}) was added to the wells and incubated for 50 min at room temperature, to yield the sandwich immunoassay. The wells were washed three times with PBST (pH 7.4, 10 mM) to remove unbounded nanobioconjugates (FITC@SiO_2-prAmPBA-*anti*-PSA-pAb/glucose). The negative control wells were treated the same as the positive wells except the *anti*-PSA-mAb step was omitted. In the negative control wells, no PSA capture is expected to occur and hence no capture of FITC@SiO_2-prAmPBA-*anti*-PSA-pAb/glucose. NaOH (20 µL, 10 mM) was used for the dissolution of the silica shell, and this released FITC molecules. The fluorescence measurements were then conducted.

3.3 Results and Discussion

3.3.1 Synthesis of FITC@SiO_2-prAmPBA-*anti*-PSA-pAb/glucose

The preparation of fluorescent silica nanobioconjugates was via a four-step process: (1) synthesis of fluorescein-isothiocynaito-3-propyltriethoxysilane (FITC-APTES), (2) preparation of fluorescent FITC-doped silica core-shell nanoparticles (FITC@SiO_2NPs), (3) surface functionalization with triethoxysilanepropyl-3-amido phenylboronic acid (TES-prAmPBA), and (4) bioconjugation with *anti*-PSA-pAb. **Scheme 3.1** shows (a) the synthesis of fluorescein-isothiocynaito-3-propyltriethoxysilane (FITC-APTES) precursor and (b) a step-by-step synthesis of the

FITC@SiO_2-prAmPBA-*anti*-PSA-pAb/glucose sensing nanobioconjugates. Initially, the successful synthesis of the organosilane precursor was achieved by covalently coupling FITC with APTES through a thiourea linkage to yield the fluorescent organosilane precursor (FITC-APTES) as shown in **Scheme 3.1(a)**. Then, a quaternary water-in-oil microemulsion system was used to covalently attach and encapsulate the FITC-APTES into the silica shell to form the fluorescent FITC-doped silica nanoparticles (FITC@SiO_2NPs) as shown in **Scheme 3.1(b)**. The preparations of the FITC@SiO_2NPs with different % w/w of FITC-APTES loading were accomplished by covalently attaching FITC-APTES into the silica shell via hydrolysis and co-polymerization of tetraethyl orthosilicate (TEOS) with ammonium solution (NH_4OH).

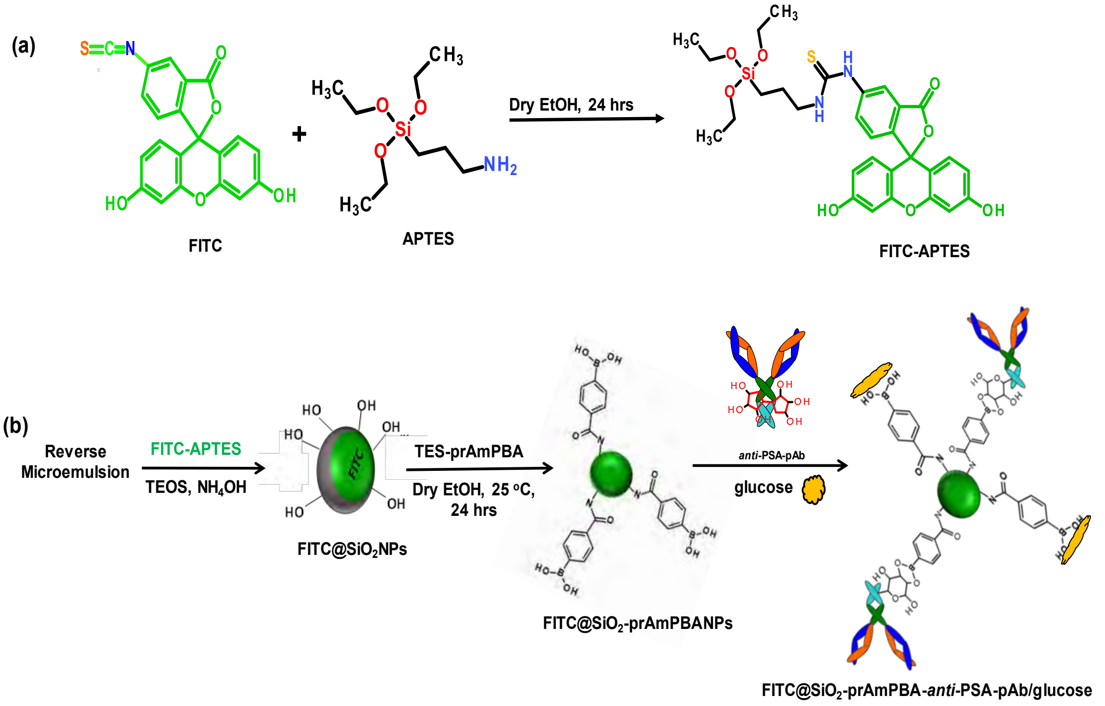

Scheme 3.1: (a) Synthesis of fluorescein-isothiocynaito-3-propyltriethoxysilane (FITC-APTES) and (b) step-by-step synthesis of the FITC@SiO_2-prAmPBA-*anti*-PSA-pAb/glucose sensing nanobioconjugates.

In the reverse microemulsion, TEOS and FITC-APTES simultaneously hydrolysed to silanol groups and followed by the nucleation and polymerization to silica nanoparticles covalently bonded to FITC molecules. The reverse microemulsion is a robust and efficient method that affords the synthesis of monodispersed FITC@SiO_2NPs [39]. Furthermore, surface functionalization of the fluorescent FITC@SiO_2NPs was modified by covalent binding triethoxysilanepropyl-3-amido phenylboronic acid (TES-prAmPBA) conjugate onto the silica surface, forming phenylboronic acid-functionalized FITC-doped silica nanoparticles, FITC@SiO_2-prAmPBANPs. The TES-prAmPBA allowed for an oriented conjugation of the polyclonal *anti*-PSA antibody. Through the boronate formation, the carbohydrates moiety within Fc domain of the antibody can specifically and covalently link to the boronic acid of the functionalized FITC@SiO_2-prAmPBANPs without hindering the antigen binding domain [51]. Therefore, the FITC@SiO_2-prAmPBANPs were bioconjugated with *anti*-PSA-pAbs and non-specific binding sites blocked with D-glucose to yield FITC@SiO_2-prAmPBA-*anti*-PSA-pAb/glucose nanobioconjugates. The bioconjugation of polyclonal *anti*-PSA antibodies onto FITC@SiO_2-prAmPBANPs was achieved through the affinity boronate ester reaction. The reaction targets the carbohydrate moiety of (N-glycan) on the Fc region of the *anti*-PSA polyclonal antibody and the glycosylation found in the Fc region of the antibody is used to react with the boronic acid functionalized FITC-doped silica nanoparticles to form cyclic ester bonds [51]. The effects of dye-loading into silica nanoparticles play a crucial role in the high sensitivity of fluorescent nanobioconjugates, and their effects on the ultra-low detection of biomarkers [46,52,53]. A step-by-step preparation, and characterization of 3.0% and 6.0% FITC@SiO_2NPs and photophysical properties were investigated.

The chapter also looked at the intact and dissolution FITC@SiO2NPs studies towards the detection for PSA.

3.3.2 Characterization of FITC@SiO2-prAmPBA-*anti*-PSA-pAb/glucose

3.3.2.1 Fourier transform infrared (FT-IR) characterization

Figure 3.1(a) shows the FT-IR spectra of (i) Fluorescein-5-isothiocyanate (FITC), (ii) (3-aminopropyl)triethoxysilane (APTES), and (iii) fluorescein-isothiocyanito-3-propyltriethoxysilane (FITC-APTES). From **Fig. 3.1(a)(i)** the FITC shows the characteristics of isothiocyanate (N=C=S) stretching peaks at 2017 $cm^{-1.}$ In addition, the aromatic CH (Φ-CH) stretching peaks are exhibited at 2971 cm^{-1} and the vibrations due to the xanthene ring (C=C) stretch at 1545 cm^{-1}, 1536 cm^{-1}, and 1458 cm^{-1}.

Lastly, the carbonyl group of lactone (Φ-O-C=O) vibration peak is exhibited at 1619 cm^{-1}, a (C-O-C) group at 1052 cm^{-1} and (O-H) peaks at 3677 cm^{-1}. **Figure 3.1(a)(ii)**, APTES shows the characteristics of siloxane (O-Si-C) stretching vibrational bands at 1019 cm^{-1}, (O-Si-O) stretching vibrations at 1103 cm^{-1}, and (Si-O) stretching vibration at 949 cm^{-1}. Additionally, the N-H asymmetric and symmetric stretching vibrations characteristics peaks of the propylamine group of APTES are found at 3289 cm^{-1} and 3350 cm^{-1}, along with the bending vibrations at 1603 cm^{-1}. Aliphatic (CH) peaks are found at 2926 cm^{-1} and 2928 cm^{-1}. The formation of FITC-APTES conjugate was monitored by the disappearance of the isothiocyanate (N=C=S) stretching vibrations of FITC. **Figure 3.1(a)(iii)**, the FITC-APTES shows the characteristic peaks corresponding to both the FITC and APTES. The disappearance of the isothiocyanate

(N=C=S) at 2027 cm^{-1} is observed and the formation of the thiourea bond (-N-CS-N) at 1309 cm^{-1} [54]. Further, the band at 1570 cm^{-1} is the thioamide (N-C=S) stretch vibrations [55]. The bands at 3359 cm^{-1} were due to N-H stretching vibrations of the thiourea group. Lastly, the (O-Si-O) stretching at 1103 cm^{-1}, and (Si-C) bending vibrations at 949 cm^{-1}. The aliphatic (CH) peaks are observed at 2869 cm^{-1} and 2930 cm^{-1} from APTES. Therefore, the observed spectra changes confirmed the successful synthesis of FITC-APTES conjugate.

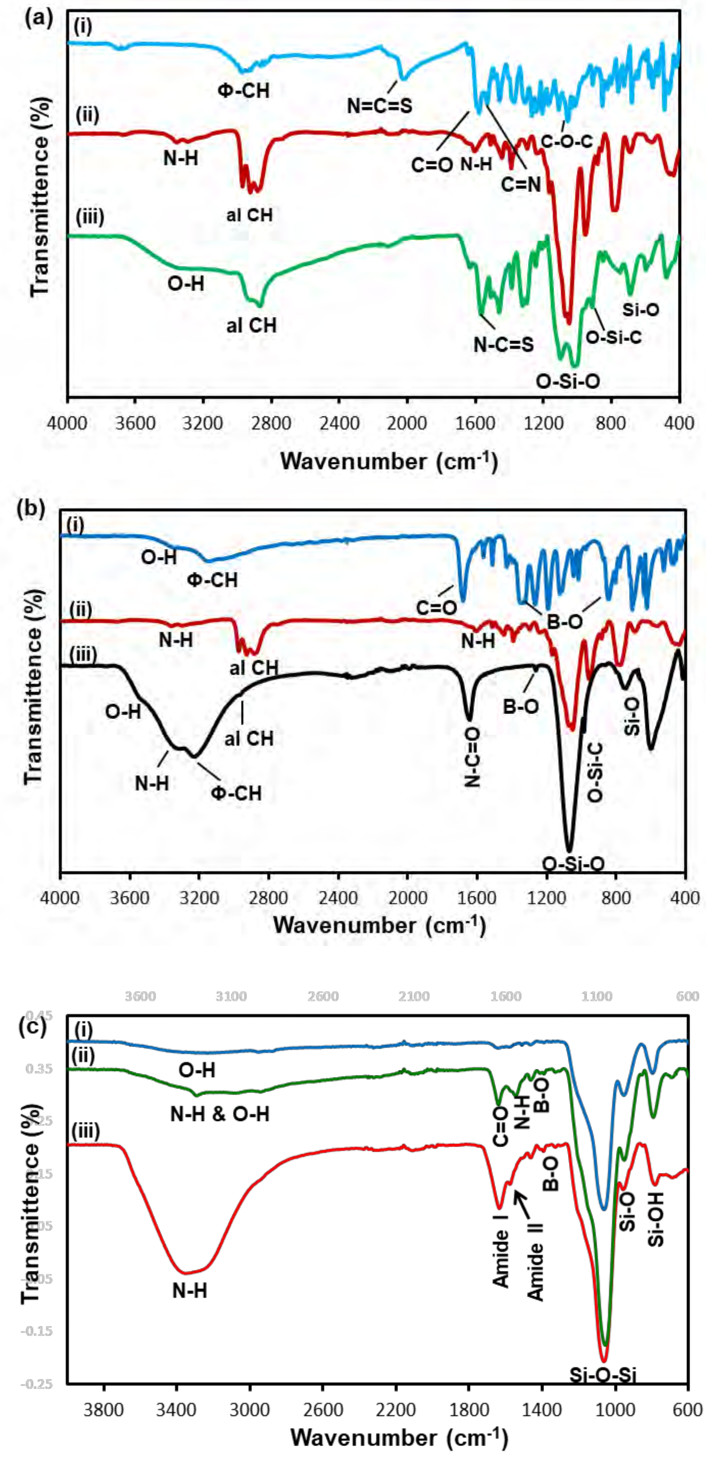

Figure 3.1: (a) FT-IR spectra of (i) FITC, (ii) APTES, and (iii) FITC-APTES. (b) FT-IR of (i) 4-CPBA, (ii) APTES, and (c) TES-prAmPBA. (c) The FT-IR of (i) FITC@SiO_2NPs, (ii) FITC@SiO_2-prAmPBANPs, and (iii) FITC@SiO_2-prAmPBA-*anti*-PSA-pAb.

Figure 3.1(b) shows the FT-IR spectra of (i) 4-carboxyphenylboronic acid (4-CPBA), (ii) APTES, and (iii) triethoxysilanepropyl-3-amido phenylboronic acid (TES-prAmPBA). **Figure 3.1(b)(i)** the FT-IR spectrum of 4-CPBA shows the (O-H) stretch of the boronic acid at 3342 cm^{-1}, aromatic C-H (Φ-CH) stretching peak at 3124 cm^{-1}, and an intense (C=O) from the carboxylic acid (COOH) peak at 1680 cm^{-1}. The B-O vibrational stretches were observed at 1321 cm^{-1} and 849 cm^{-1}. **Figure 3.1(b)(iii)**, shows the spectrum of the TES-prAmPBA. TES-prAmPBA was obtained by reacting APTES to 4-CPBA via an amide bond formation. From the spectrum, the disappearance of the primary amine (NH_2) from APTES at 1575 cm^{-1} as shown in **Fig. 3.1(a)(ii) and (b)(ii)**, and the appearance of the carbonyl (C=O) stretch for an amide bond (N-C=O) at 1639 cm^{-1}. Also, the (O-H) stretch of the boronic acid remained at 3526 cm^{-1} and shifted from 3342 cm^{-1} from 4-CPBA. The secondary amide stretch (N-H) at 3316 cm^{-1} is observed. This indicated the presence of the amide bond formation between APTES and 4-CPBA. The C-H stretches due to aromatic (Φ-CH) and aliphatic (al-CH) were observed at 3226 cm^{-1} and 2955 cm^{-1}, respectively. The B-O stretch was also retained and observed at 1317 cm^{-1}, and this slightly shifted in TES-prAmPBA when compared to 4-CPBA. The presence of the characteristic peak at 1060 cm^{-1} was attributed to the O-Si-O from the APTES moiety. The observed changes confirm the successful synthesis of triethoxysilanepropyl-3-amido phenylboronic acid (TES-prAmPBA).

Figure 3.1(c) shows the FT-IR spectra of (i) FITC@SiO_2NPs, (ii) FITC@SiO_2-prAmPBANPs, and (iii) FITC@SiO_2-prAmPBA-*anti*-PSA-pAb. The FT-IR spectra in **Figure 3.1(c)(i)**, show the vibrational bands at 1036 cm^{-1}, 948 cm^{-1}, and 786 cm^{-1}. The bands indicate the absorption asymmetric stretching of siloxane (Si-O-Si), (Si-O) groups, and the presence of silanol (Si-OH) groups, respectively. The presence of broad (O-H) peaks at 3287 cm^{-1} and small peaks exhibited at 1323 cm^{-1}, 1462 cm^{-1}, 1502 cm^{-1}, and 1642 cm^{-1} are assigned to the aromatic and aliphatic functional groups of the FITC-APTES. Therefore, confirming the successful encapsulation of FITC-APTES and the preparations of fluorescent silica nanoparticles. After surface modification with TES-prAmPBA to form FITC@SiO$_2$-prAmPBNPs. **Figure 3.1(c)(ii)** the FT-IR spectrum showed the presence of characteristic peaks at 3303 cm^{-1} corresponding to the O-H stretching of the phenylboronic acid, and the N-H bending from the APTES to the carbonyl oxygen of the phenylboronic acid, respectively. This was accompanied by the presence of a C=O stretch at 1647 cm $^{-1}$ and the emergence of the B-O vibrational stretch at 1395 cm^{-1} from the phenylboronic acid. Then, the bioconjugation of FITC@SiO$_2$-prAmPBANPs to *anti*-PSA-pAbs was achieved via boronate ester bonds. The boronate ester bonds were formed between the cis-diol of the N-glycan moieties on the Fc region of the antibody covalently linked to the boron-bound hydroxyl (O-H) groups on the phenylboronic acid. The boronic acid bioconjugation route helps maintain the orientation of the antibody for enhanced antigen binding. **Figure 3.1(c)(iii)** shows the FT-IR spectrum of the FITC@SiO$_2$-prAmPBA-*anti*-PSA-pAb/glucose. The FT-IR spectrum shows the appearance of an intense stretching vibration at 1639 cm^{-1} and 1580 cm^{-1}, assigned to the amide I and amide II from the boronate ester bonds of the *anti*-PSA-pAb antibody. The broad absorption peak at 3328 cm^{-1}, was assigned to the presence of the NH$_2$ from the antibody. The peak shifts of B-O at 1322 cm^{-1} confirm the successful bioconjugation of the antibody to the phenylboronic acid.

3.3.2.2 Zeta potential analysis

The modification steps of the FITC@SiO_2NPs with TES-prAmPBA and *anti*-PSA-pAb were further confirmed by zeta potential. The changes in the zeta potential at different pH values confirmed the surface modification and surface charges of the fluorescent silica nanobioconjugates. **Figures 3.2** show the zeta potential measurements (surface charges) of the fluorescent silica nanoparticles as a function of pH. **Figure 3.2(a)** shows the zeta potential (mV) plot at different pH values (1-10) and **Figure 3.2(b)** the bar graph of zeta potential at pH (7.0) of 6.0% w/w (i) FITC@SiO_2NPs, (ii) FITC@SiO_2-prAmPBANPs, and (iii) FITC@SiO_2-prAmPBA-*anti*-PSA-pAb. The FITC-doped silica nanoparticles exhibited pH-dependent zeta potential values. The zeta potential of (i) FITC@SiO_2NPs shows that the nanoparticles have a negative charge at higher pH values. The isoelectric point (IEP) of FITC@SiO_2NPs was at pH 4.8. A zeta potential value at pH 7.0 was -25.9 mV due to the deprotonated hydroxyl (-OH) groups from the silica and FITC. After surface functionalization of FITC@SiO_2NPs with TES-prAmPBA to form (ii) FITC@SiO_2-prAmPBANPs, the isoelectric point is shifted to pH 5.3 and at pH 7.0 the zeta potential was -19.1 mV. This decrease in the zeta potential was from -25.9 mV for FITC@SiO_2NPs to -19.1 mV for FITC@SiO_2-prAmPBANPs confirmed the successful functionalization with TES-prAmPBA. After bioconjugation with *anti*-PSA-pAb, the isoelectric point was observed at pH 6.8. The zeta potential of FITC@SiO_2-prAmPBANPs decreased to -3.6 mV. The decrease in zeta potential was attributed to the binding of the *anti*-PSA-pAb to phenylboronic acid via boronate ester to form FITC@SiO_2-prAmPBA-*anti*-PSA-pAb. Bioconjugation of *anti*-PSA-pAb did not occur in the absence of TES-prAmPBA as the zeta potential remained the -19.1 mV and similar to FITC@SiO_2-prAmPBANPs. The change in zeta potential at different pH solutions confirmed the preparations of the fluorescent FITC@SiO2-prAmPBA-*anti*-PSA-pAb nanobioconjugates.

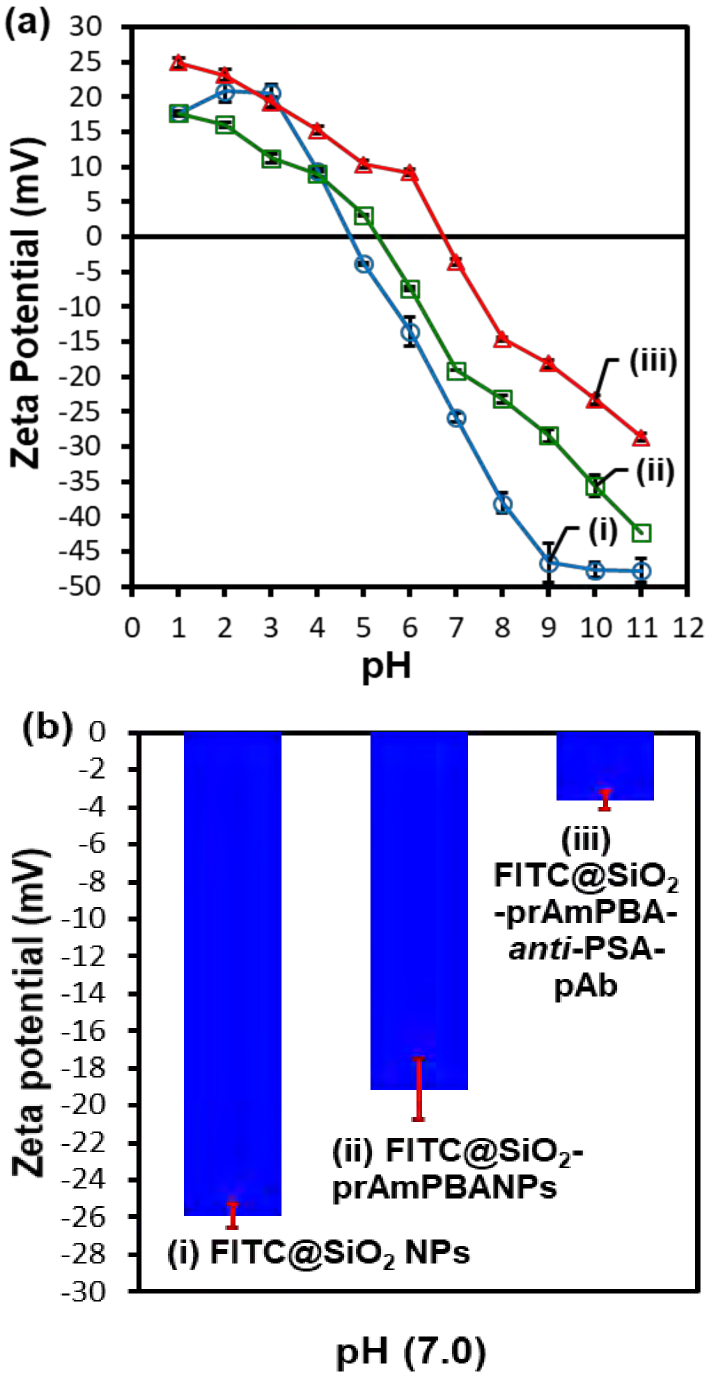

Figure 3.2: (a) Zeta potential (mV) vs pH, and (b) bar graph of zeta-potential at pH (7.0) of (i) FITC@SiO2NPs, (ii) FITC@SiO2-prAmPBANPs, and (iii) FITC@SiO2-prAmPBA-*anti*-PSA-pAb. The data were measured in triplicates (n = 3).

3.3.2.3 Microscopic characterization

The synthesis of FITC@SiO_2NPs with different (w/w) of FITC-APTES loading was prepared following the in-house modified water-in-oil (W/O) microemulsion method [49]. To confirm the successful synthesis of FITC@SiO_2NPs at different (%, w/w) of FITC-APTES loading and the effects of surface modification with TES-prAmPBA, TEM and EDS analysis were performed.

3.3.2.4 Transmission electronic microscopy (TEM) micrographs

TEM micrographs confirm the morphology and size distribution of the fluorescent silica nanoparticles. **Figure 3.3** shows the TEM images and size distribution histograms of 3.0% and 6.0% FITC@SiO_2NPs before and after surface functionalization with phenylboronic acid. From **Fig. 3.3**, the TEM images, the nanoparticles were spherical and exhibited good monodispersity. For 3.0% loading, the average size distributions were 30 ± 3 nm for FITC@SiO_2NPs shown in **Fig. 3.3(a)** and 32 ± 4 nm for FITC@SiO_2-prAmPBANPs shown in **Fig. 3.3(b).** For 6.0% loading, the average sizes were 46 ± 2 nm for FITC@SiO_2NPs shown in **Fig. 3.3(c)** and 48 ± 10 nm FITC@SiO_2-prAmPBANPs shown in **Fig. 3.3(d)**. A 16 nm increase in the average size from 3.0% to 6.0%, w/w loading confirmed higher loading due to increased concentration of FITC-APTES. In addition, the high concentration of FITC-APTES will result in high fluorescence. A 2 nm average size increase was observed for the different (%, w/w) loadings after functionalization with TES-prAmPBA to form FITC@SiO_2-prAmPBANPs. The size distribution of FITC@SiO_2-prAmPBA-*anti*-PSA-pAb shown in

Fig. S3.3, showed no size variation compared to the FITC@SiO_2-prAmPBANPs. This was due to the antibody being a protein molecule and under TEM measurement does not show the increase in diameter.

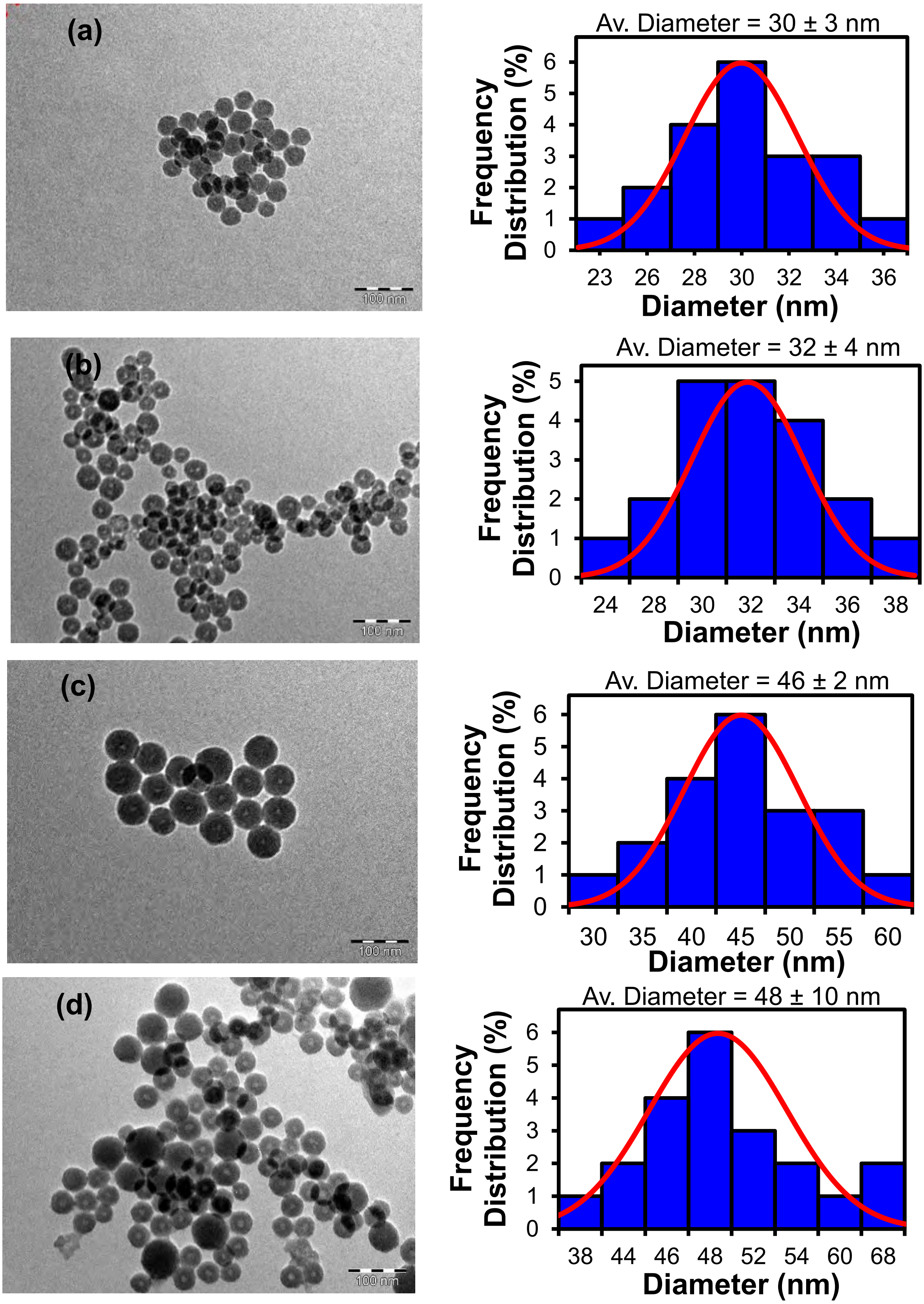

Figure 3.3: TEM micrographs of fluorescent silica nanoparticles of (a) 3.0% FITC@SiO_2NPs and (b) 3% FITC@SiO_2-prAmPBANPs. (c) 6.0% FITC@SiO_2NPs and (d) 6% FITC@SiO_2-prAmPBANPs and their corresponding size distribution histograms.

3.3.2.5 Energy dispersive X-ray spectroscopy (EDS analysis)

Moreover, the encapsulation of FITC-APTES and modification of FITC@SiO_2NPs with TES-prAmPBA and *anti*-PSA-pAb were confirmed by EDS. In **Fig. 3.4**, shows the EDS spectra of (a) FITC-APTES, (b) FITC@SiO_2NPs, (c) FITC@SiO_2-prAmPBANPs, and (d) FITC@SiO_2-prAmPBA-*anti*-PSA-pAb nanobioconjugates. From **Fig. 3.4(a)**, the silica peak (Si K) is from FITC-APTES was observed. The sulfur (S K), oxygen (O K), nitrogen (N K), and carbon (C K) are from the FITC (thiourea group) after the successful synthesis of conjugate FITC-APTES. The elemental composition confirmed the successful synthesis of the FITC-APTES conjugate, especially the sulfur peak (S K, 1.6%) and nitrogen peak (N K, 3.7%) ration of 1:2 as per the chemical structure. **Figure 3.4(b)** shows an increase in the silica (Si K) and oxygen peaks (O K) peaks after the encapsulation of FITC-APTES, which resulted from the treatment of FITC-APTES with tetraethyl orthosilicate (TEOS) to form FITC@SiO_2NPs. The hydrolysis of TEOS introduces the presence of the silica (Si K) and oxygen (O K) during the formation of the FITC@SiO_2NPs. In addition, the increase in the silica (Si K) and oxygen peak (O K) are due to the -OH from TEOS and FITC-APTES in the silica nanoparticles. The results also show an intense decrease in nitrogen (N K) and carbon peaks (C K) attributed to the encapsulation of FITC-APTES into the silica nanoparticles. The increase in the elemental composition for silica (Si K) from 11.9% to 39,1% and for oxygen (O K) from 30.6% to 50.0% was attributed to the formation of the silica shell and confirming the successful synthesis of FITC@SiO_2NPs. **Figure 3.4(c)** shows the presence of the boron peak (B K, 15.7%) attributed to the phenylboronic acid, which reveals the successful synthesis of FITC@SiO_2-prAmPBANPs. An increase in the carbon peak (C K) elemental composition from 7.8%

to 15.5% confirmed the surface functionalization of FITC@SiO_2NPs with TES-prAmPBA to form FITC@SiO_2-prAmPBANPs. Similarly, **Fig. 3.4(d)** shows the EDS spectrum of FITC@SiO_2-prAmPBA-*anti*-PSA-pAb after the bioconjugation of FITC@SiO_2-prAmPBANPs with *anti*-PSA-pAb. After the bioconjugation, the oxygen (O K) and nitrogen peaks (N K) elemental position increased confirming the antibody attachment. The oxygen (O K) elemental composition increased 45.7% to 47.3% and the nitrogen (N K) from 0% to 4.3% due to the protein (*anti*-PSA-pAb). Moreover, the presence of the silica peak in all materials was an indication that the silica nanomaterial coating was not affected by subsequent functionalization with TES-prAmPBA, *anti*-PSA-pAb, and that FITC-APTES remains encapsulated

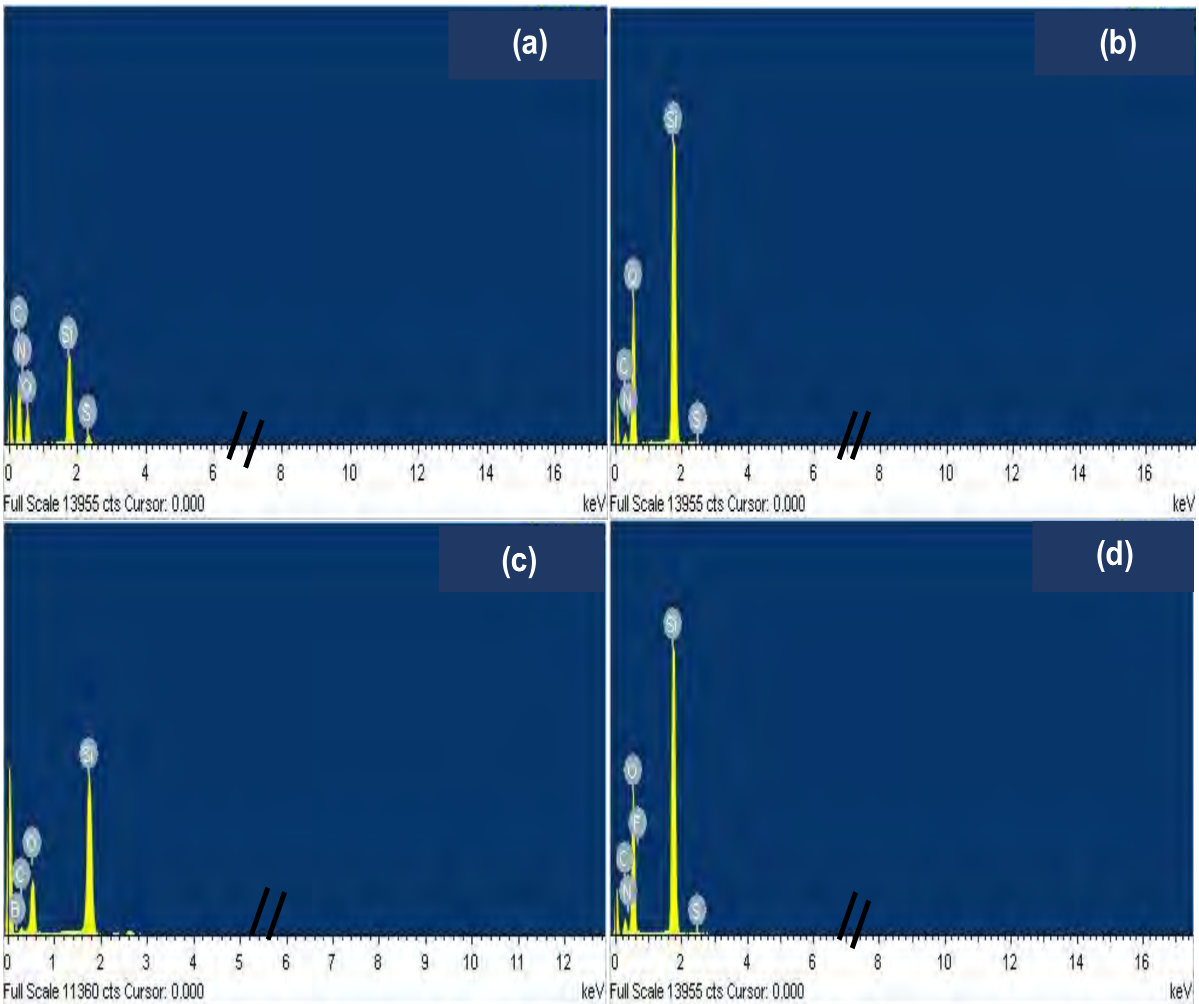

Elemental Composition (wt%)								
	C K	N K	O K	Si K	S K	B K	F K	Total
FITC-APTES	52.24	3.70	30.55	11.87	1.64	-	-	100
FITC@SiO$_2$NPs	7.81	3.02	50.04	39.13	-	-	-	100
FITC@SiO$_2$-prAmPBANPs	15.52	-	45.70	23.13	-	15.65	-	100
FITC@SiO$_2$-prAmPBA-*anti*-PSA-pAb/glucose	15.82	4.32	47.25	21.66	-	9.12	1.83	100

Figure 3.4: The EDS images of (a) FITC-APTES, (b) FITC@SiO$_2$NPs, (c) FITC@SiO$_2$-prAmPBANPs, and (d) FITC@SiO$_2$-prAmPBA-*anti*-PSA-pAb. The Table shows the elemental composition.

3.3.3 Bradford assay *anti*-PSA-pAb onto FITC@SiO_2-prAmPBANPs

The Bradford assay was used to determine the protein quantification of *anti*-PSA polyclonal antibodies (*anti*-PSA-pAbs) onto FITC@SiO_2-prAmPBANPs. UV-Vis measurements were obtained at 595 nm which corresponded to the BSA standard solutions and protein (*anti*-PSA-pAb) in solution. The calibration curve of known BSA concentrations as shown in **Fig. 3.5(b)** was used to extrapolate and determine the concentrations of the *anti*-PSA-pAb in the supernatant solution. The absorbance of the used volumes of the BSA standard solutions and protein suspension were recorded in triplicates. Mean values were determined and found to range from 0.25 ± 0.09 to 0.34 ± 0.09 a.u with very low standard deviations. The mean value of the unknown concentration of the *anti*-PSA-pAbs suspension was 0.27 ± 0.02 a.u and recorded as a representative value of the absorbance of *anti*-PSA-pAbs. Then, this value was fitted into the calibration curve, along with the BSA standard solutions mean values, and used to calculate the concentration of the unknown protein x (*anti*-PSA-pAbs) after bioconjugation with FITC@SiO_2-prAmPBANPs. The linear equation used was ΔAbs = 0.003 [*anti*-PSA-pAb] + 0.256 with $R^2 = 0.971$ was used to determine the concentration of the unknown protein x (*anti*-PSA-pAbs) and which was found to be 8.70 $\mu g.mL^{-1}$.

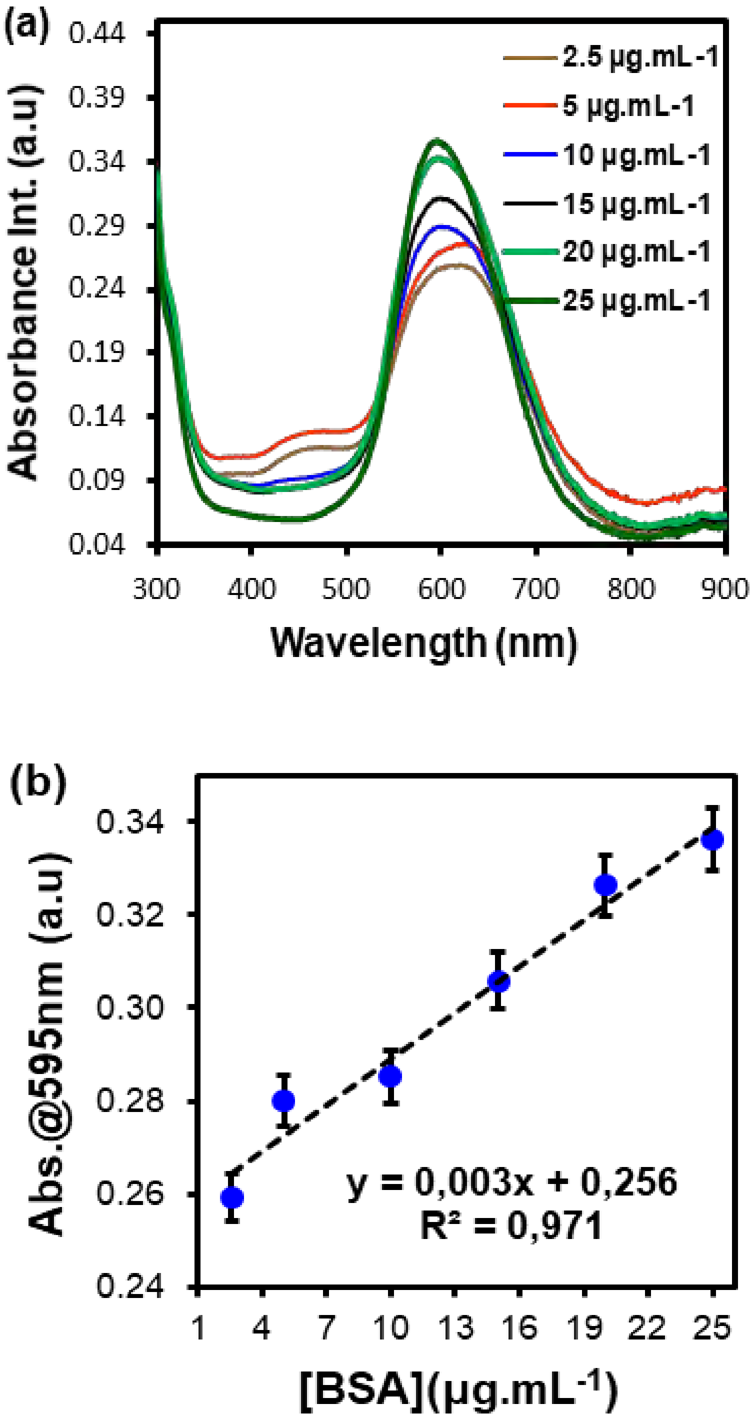

Figure 3.5: (a) UV-Vis spectra of different BSA standards and *anti*-PSA-pAbs concentrations, and (b) the corresponding calibration curve (n = 3).

Further, UV-Vis spectra and the Bradford assay were used to confirm the immobilization of *anti*-PSA-pAb. The Bradford assay was used to monitor and quantify *anti*-PSA-pAb bioconjugated onto FITC@SiO$_2$-prAmPBANPs. The UV-Vis absorbance measurements were obtained at 595 nm and corresponded to the BSA standard solutions and a solution of the protein (*anti*-PSA-pAb). The concentration of *anti*-PSA-pAb was measured before and after bioconjugation. The difference gave the amount of *anti*-PSA-pAb conjugated. The percentage of the conjugation efficiency (%CE) was calculated using **Equation (3.2)**:

$$\%\boldsymbol{CE} = \frac{[anti\mathrm{-PSA-pAb}]_0 - [anti\mathrm{-PSA-pAb}]_\mathrm{f}}{[anti\mathrm{-PSA-pAb}]_0} \text{ x } 100 \qquad \textbf{(3.2)}$$

where the $[anti - \mathrm{PSA} - \mathrm{pAb}]_0$ and $[anti - \mathrm{PSA} - \mathrm{pAb}]_\mathrm{f}$ shows the initial and final concentrations of the *anti*-PSA-pAb before and after bioconjugation. The %CE was found to be 79.3% corresponding to the amount of protein conjugated to form FITC@SiO$_2$-prAmPBA-*anti*-PSA-pAb nanobioconjugates. The Bradford assay as shown in **Fig. 3.5** confirmed the successful preparations of FITC@SiO$_2$-prAmPBA-*anti*-PSA-pAb nanobioconjugates. Then, the non-specific boronic acid sites were blocked with D-glucose solution to yield FITC@SiO$_2$-prAmPBA-*anti*-PSA-pAb/glucose nanobioconjugates and used for intact and dissolution FITC@SiO$_2$-prAmPBA-*anti*-PSA-pAb/glucose for the detection (signal generation) of PSA.

3.3.4 Photophysical properties of the fluorescent silica nanobioconjugates

To analyse the enhanced fluorescence properties of the FITC@SiO$_2$NPs, the excitation and fluorescence emissions properties of the fluorescent silica nanobioconjugates were compared to FITC and FITC-APTES. **Figure 3.6** shows the

UV-Vis and fluorescence measurements observed for the ground-state absorption and fluorescence emission of (a) FITC, (b) FITC-APTES, (c) FITC@SiO$_2$NPs, (d) FITC@SiO$_2$-prAmPBANPs, and (e) FITC@SiO$_2$-prAmPBA-*anti*-PSA-pAb/glucose. The UV-Vis spectra were used to confirm the encapsulation of FITC-APTES, the effects of coupling to TES-prAmPBA, and the attachment of *anti*-PSA-pAb onto FITC@SiO$_2$NPs. **Figure 3.6**, shows that all the fluorescent dyes and silica nanoparticles exhibited strong ground-state absorptions. In **Fig. 3.6(a)** and **(b)**, the UV-Vis spectra exhibited a single absorption peak at 493 nm. The nanoparticles, FITC@SiO$_2$NPs in **Fig. 3.6(c)**, **(d)**, and **(e)** exhibited a 2 nm shift. The Stokes shift (red shift) was due to the interactions between FITC-APTES in the silica nanoparticles matrix with absorption peaks observed at 495 nm. From the fluorescence spectra, the maximum fluorescence emission wavelength for FITC was observed at 520 nm. The maximum emission intensities at 518 nm were recorded for both the FITC-APTES and the functionalized FITC@SiO$_2$NPs as shown in **Fig. 3.6(b)** - **(e)**, respectively. After the immobilization of *anti*-PSA-pAb, the same emission wavelength of 518 nm was observed. Therefore, confirming FITC-APTES was successfully conjugated with APTES and encapsulated into the silica nanoparticles. The dye did not leak from the silica nanoparticles, and surface modification had no effects on the absorptivity and emission of FITC-APTES.

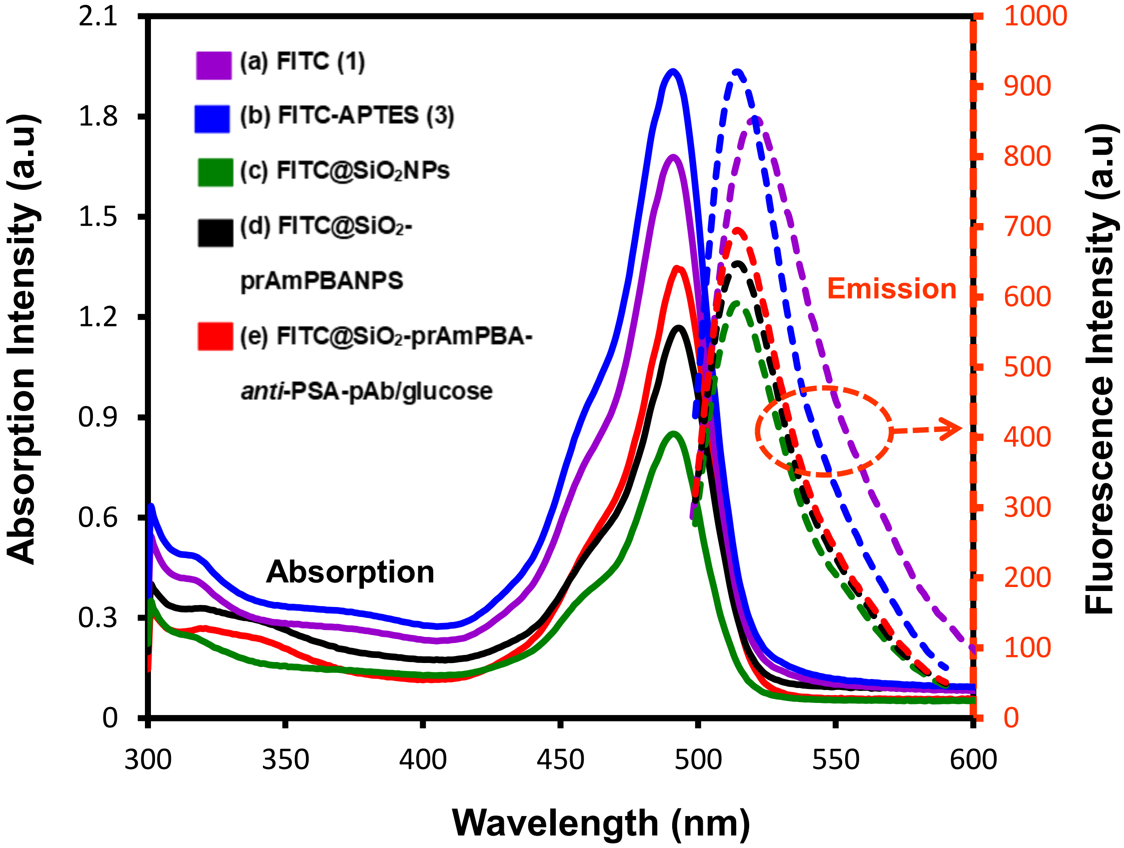

Figure 3.6: Ground state absorption and fluorescence emission spectra of (a) FITC, (b) FITC-APTES, (c) FITC@SiO_2NPs, (d) FITC2SiO_2-prAmPBANPs, and (e) FITC@SiO_2-prAmPBA-*anti*-PSA-pAb/glucose.

3.3.5 Optimization of the fluorescent sensing nanobioconjugates

3.3.5.1 Dye-leakage study

Figure 3.7 shows the normalized fluorescence intensity over time of dye-leaking studies of FITC@SiO_2NPs in PBS buffer (pH 7.4, 10 mM). The nanoparticles were subjected to sonication to assess for mechanical dye leakage and the supernatant was measured. The study was conducted to compare the effects of binding and encapsulation of the FITC-APTES into FITC@SiO2NPs. The degree of dye leakage from the silica matrix was investigated by measuring the fluorescence emission of the supernatant of FITC@SiO2NPs after sonication. From **Fig. 3.7**, about 65 % of the dye was retained in the silica nanoparticles after sonication over a period of 50 min. In correlation with the literature [44,45], the study showed that coupling FITC-APTES into the silica nanoparticles to form FITC@SiO2NPs. There was no encapsulation or doping of FITC dyes without using FITC-APTES. The synthesized FITC@SiO2NPs were suitable to be used in further studies.

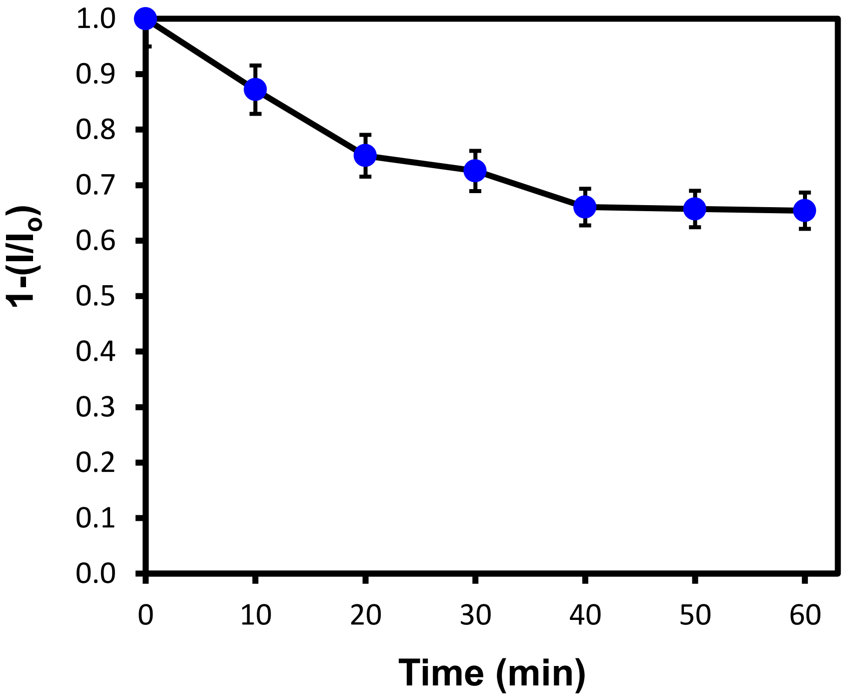

Figure 3.7: Fluorescence intensity over time for a dye-leaking study of FITC@SiO2NPs in 10 mM PBS.

3.3.5.2 Photostability Study

The photostability of the encapsulated fluorescent dye was investigated. **Figure 3.8** shows the normalized fluorescence intensity over time of photostability studies of (a) FITC, (b) FITC-APTES, and (c) FITC@SiO$_2$NPs in PBS buffer (pH 7.4, 10 mM). **Figure 3.8** shows the normalized fluorescence intensity as a function of time. **Figure 3.8(a)** exhibited a sharp decrease in intensity due to photobleaching, and after 40 min there was very low (<10%) fluorescence intensity left. The same was observed for FITC-APTES in **Fig. 3.8(b)**. **Figure 3.8(c)** exhibited excellent stability with 70% of FITC fluorescence intensity still intact. The FITC fluorophores within the silica nanoparticles retained their excellent fluorescence intensity. These results indicated that the incorporation of FITC-APTES into silica nanoparticles improved the photostability of the FITC dye molecules.

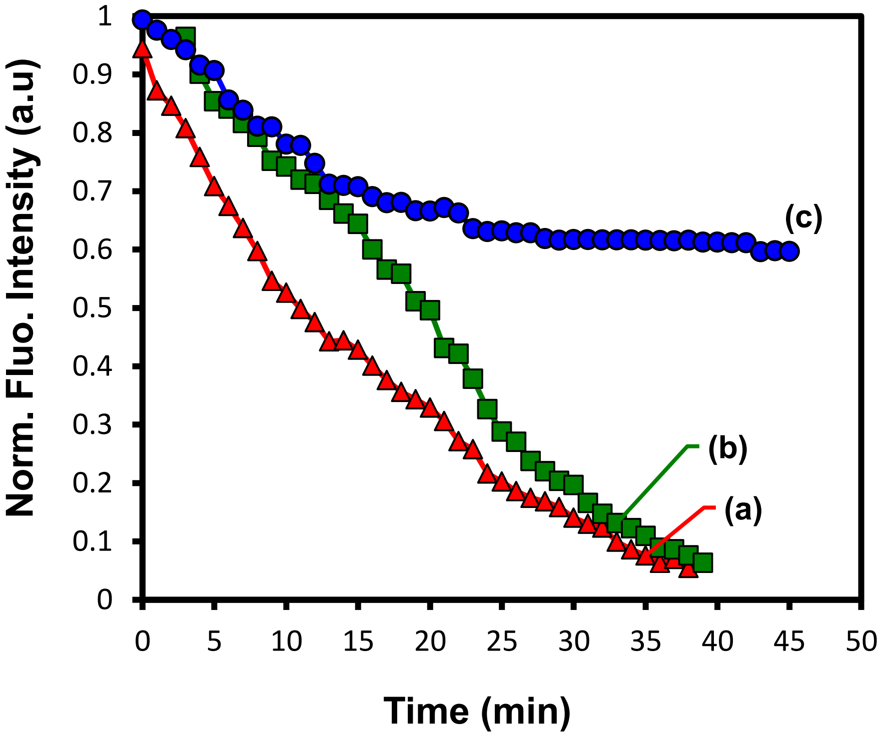

Figure 3.8: Fluorescence intensity over time for photostability study of (a) FITC, (b) FITC-APTES, and (c) FITC@SiO$_2$NPs in 10 mM PBS.

3.3.5.3 Effects of pH conditions

Figure 3.9 shows (a) fluorescence spectra, and (b) the corresponding pH response curve of FITC@SiO_2NPs in varied PBS buffer (pH 2.0 - 11.0, 10 mM). **Figures 3.9(a)** and **(b)** evaluated the effects of pH on the photostability of the FITC@SiO_2NPs and the optimum buffer pH for the dissolution of the sensing nanobioconjugates. This is to find the optimum pH that will not affect the integrity of the fluorescence properties of the FITC@SiO_2NPs leading to false positive readings for the proposed fluorescent immunosensor. From **Fig. 3.9(a)** and **(b)**, the fluorescence intensity increased with increasing pH values of 10 mM PBS buffer pH 6.0 to 11.0. The results indicated that at higher pH values above pH 7.0, the fluorescent silica nanoparticle shell becomes unstable and releases FITC as has been reported [56]. The dissociation and complete hydrolysis of the FITC@SiO_2NPs is observed at pH 11.0. Therefore, considering the results, the FITC dye is released into the solution at higher (alkaline) pH conditions. NaOH (10 mM, pH 12) was adopted as the dissolution solution for the release of FITC-APTES for enhanced fluorescence measurements. The choice of NaOH is due to dissolution of the silica matrix being accelerated at higher pH and enhanced in the presence of cations (that easily ionises) such as sodium (Na^+) and potassium (K^+) ions [56].

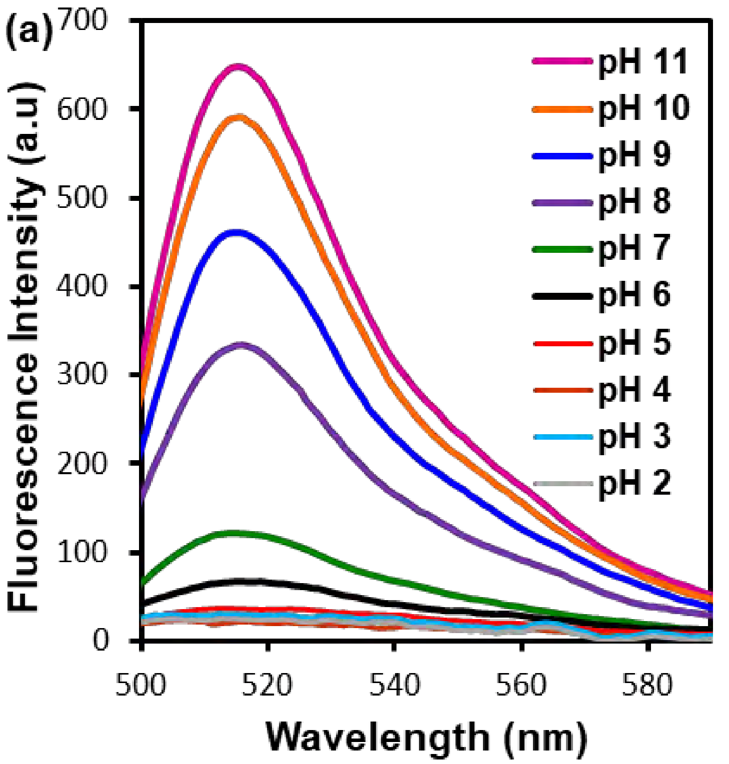

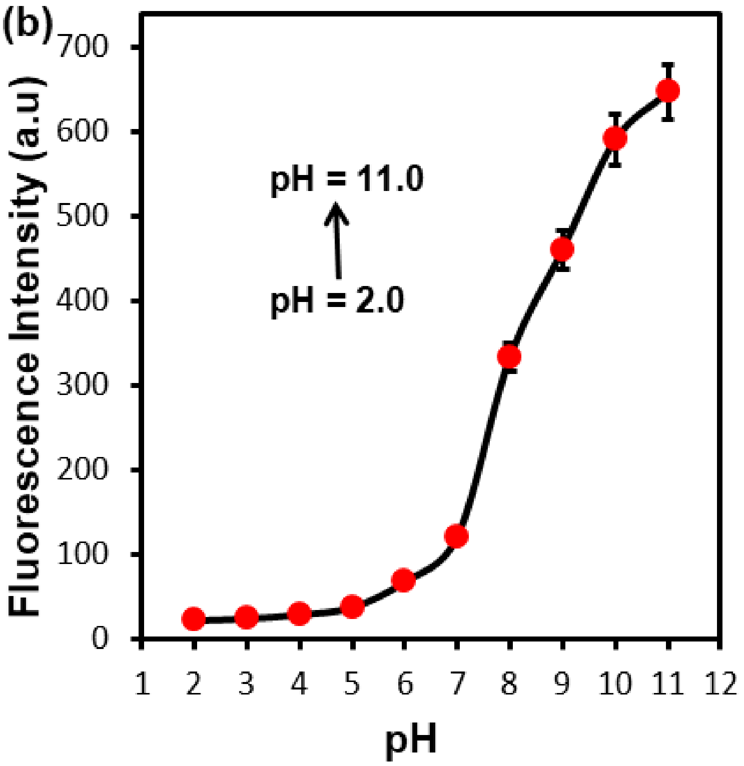

Figure 3.9: (a) Fluorescence spectra, and (b) corresponding fluorescence intensity of FITC@SiO_2NPs in varied pH (2.0 - 11.0) in 10 mM PBS.

3.3.5.4 Dye-loading study

The dye-loading experiment was carried out to determine the possible occurrence of the Highest Occupied Molecular Orbital-Fluorescence Resonance Energy Transfer (HOMO-FRET) upon loading of FITC-APTES into the silica nanoparticles. The optimization of the altered dye-loaded fluorescent silica nanoparticles for high sensitivity and signal amplification studies was observed. **Figure 3.10** shows the ground-state absorption and fluorescence emission spectra of the 3.0% and 6.0%, w/w dye-loaded FITC@SiO_2NPs, respectively. The absorption intensity increases with an increase in the %, w/w of FITC-APTES loaded. The increase in the intensity is related to the number of FITC-APTES molecules incorporated within the FITC@SiO_2NPs. An increase in %, w/w indicated that more FITC-APTES molecules were loaded into the 6.0% fluorescent silica nanoparticles. Furthermore, the number of FITC-APTES molecules per FITC@SiO_2NPs was estimated to be 6.02×10^{26} for 3.0% and 3.23×10^{27} for 6.0% w/w loadings, respectively, as shown in **Table 3.1**. The fluorescence emission intensity also increased with increasing %, w/w FITC-APTES loading in nanoparticles from 3.0% to 6.0%. The 6 (%, w/w) exhibited a higher fluorescence intensity as compared with the 3 (%, w/w) FITC@SiO_2NPs. Both silica nanoparticles exhibited negligible quenching, indicating a reduced dye-dye intermolecular interaction. Therefore, the FITC-APTES was substantially loaded into the both the 3.0% and 6.0% FITC@SiO_2NPs and no fluorescence quenching (HOMO-FRET) was observed. The fluorescence quantum efficiency for both the 3.0% and 6.0% (w/w) FITC@SiO_2NPs was measured to determine the fluorescence efficiency of the FITC-APTES before and after dissolution.

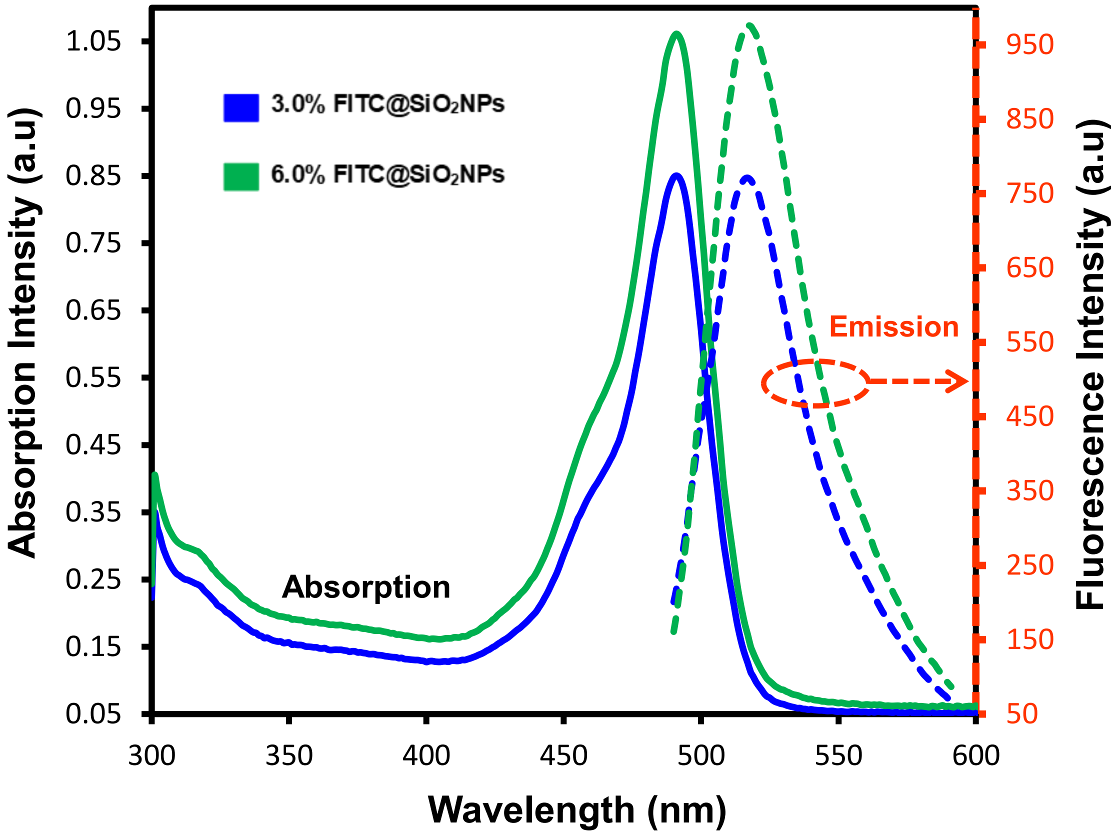

Figure 3.10: Ground-state absorption and fluorescence emission spectra of FITC@SiO2NPs before and after the addition of NaOH (10 mM). All samples were diluted in 10 mM PBS buffer pH (7.4) (n =3).

3.3.5.5 FITC-APTES loading ratio

The number of FITC-APTES molecules encapsulated per FITC@SiO2NPs was estimated from absorption readings. The estimations were investigated by dissolving an equal amount of the FITC@SiO2NPs of (3.0% and 6.0%, w/w) dye loadings with NaOH (10 mM). The absorption intensity reading of the dissolved FITC@SiO2NPs was recorded. The adsorption intensity was used to calculate the number of FITC-APTES molecules per silica nanoparticles using a molar extinction coefficient (∑) of FITC and the TEM size. From the TEM size (diameter, d), the average volume of a single FITC@SiO2NP was obtained using **Equation (3.3)**:

$$V_{FITC@SiO2NP} = \frac{4}{3}\,\pi\,(\frac{d}{2})^{3} \qquad \textbf{(3.3)}$$

The total number of FITC@SiO2NP in the suspension was calculated based on the dry weight and the density of the amorphous silica matrix (2.22 g.cm^{-3}) [42]. The total number of FITC-APTES, FITC-APTES$_{tot}$ from the dissolved nanoparticles was determined from the absorption intensity after the dissolution using **Equation (3.4)**:

$$\mathrm{FITC-APTES_{tot}} = \frac{(6.022 \text{ x } 10^{23})(A)}{\varepsilon l} \qquad \textbf{(3.4)}$$

where *l* is the path length (1 cm), A is the absorption intensity, and *ε* is the molar absorptivity of FITC (73,000 cm^{-1}M^{-1}). The number of FITC-APTES molecules per FITC@SiO2NP is equal to FITC-APTES per unit volume divided by the number of FITC@SiO2NP per unit volume as expressed in **Equation (3.5)**:

$$n_{FITC-APTES} = \frac{\mathrm{FITC-APTES_{tot}}}{n_{FITC@SiO2NP}} \qquad \textbf{(3.5)}$$

where $n_{FITC-APTES}$ is the number of FITC-APTES molecules per FITC@SiO2NP, FITC-APTES$_{tot}$ is the total number of FITC-APTES molecules and $n_{FITC@SiO2NPs}$ is the number of FITC@SiO2NP in suspension. The total number of FITC@SiO2NP in suspension, the average volume of the as-synthesized FITC@SiO2NP, and the number of FITC-APTES per FITC@SiO2NP at 3.0% and 6.0% FITC-APTES loading are summarised in **Table 3.1**. The average volume of the FITC@SiO2NP increased with an increase in TEM size. The number of FITC molecules per FITC@SiO2NP also increased from 3.0% to 6.0% loading, confirming that with an increase in FITC molecules doped into the silica nanoparticles, more fluorophores are encapsulated.

Table 3.1: Determination of the number of FITC-APTES molecules loaded per fluorescent silica nanoparticle using TEM and UV-absorption values.

% w/w	TEM Size (nm)	Average Volume (cm^3)	Nanoparticles in suspension (particles)	FITC-APTES molecules in suspension (moles)	FITC-APTES per nanoparticle (moles)
3.0	30	1.56×10^{-17}	7.05×10^{15}	7.15×10^{18}	6.07×10^{26}
6.0	46	5.79×10^{-15}	1.89×10^{15}	1.02×10^{19}	3.23×10^{27}

3.3.6 Fluorescence quantum efficiency study

Figure 3.11 shows the fluorescence quantum efficiency of FITC@SiO_2NPs (before and after dissolution) against FITC. From **Fig. 3.11**, the fluorescence quantum efficiency of FITC@SiO_2NPs increased with increasing %, w/w FITC-APTES loading. The standard FITC was used as a 100% quantum efficiency. The fluorescence efficiency of 3.0% w/w FITC@SiO_2NPs was 57% and 77% for the 6.0% w/w. The fluorescence efficiency of both silica nanoparticles was lower than that of FITC before the addition of NaOH solution (10 mM). The results showed that at a higher % w/w, loading, a higher fluorescent emission is expected due to increased FITC-APTES molecules in the silica nanoparticles. The quantum efficiency results corresponded to the trend observed for fluorescence emission intensity in **Fig. 3.10**. The quantum efficiency of the FITC@SiO_2NPs with different FITC-APTES loading after dissolution with NaOH increased. The NaOH leads to the breaking up of the silica nanoparticles and dissolution of the silica shell for FITC@SiO_2NPs releasing the FITC-APTES molecules into solution. The FITC-APTES molecules in solution fluorescence without interference. The result as shown in **Fig. 3.11**, the 6.0% FITC@SiO_2NPs exhibited an increase in its fluorescence quantum efficiency from 77% to 96.0% as compared to the 3.0% FITC@SiO2NPs loading. The quantum efficiency of the 6.0% FITC@SiO2NPs was close to 100% as compared to the efficient quantum efficiency of FITC. Therefore, the 6.0% FITC@SiO2NPs with a uniform monodispersed morphology shown in the TEM images in **Fig. 3.3**, and an efficient fluorescence quantum efficiency (96.0%) after dissolution with NaOH solution, the 6.0% FITC@SiO2-prAmPBA-*anti*-PSA-pAb/glucose was favourable as sensing nanobioconjugates for PSA detection.

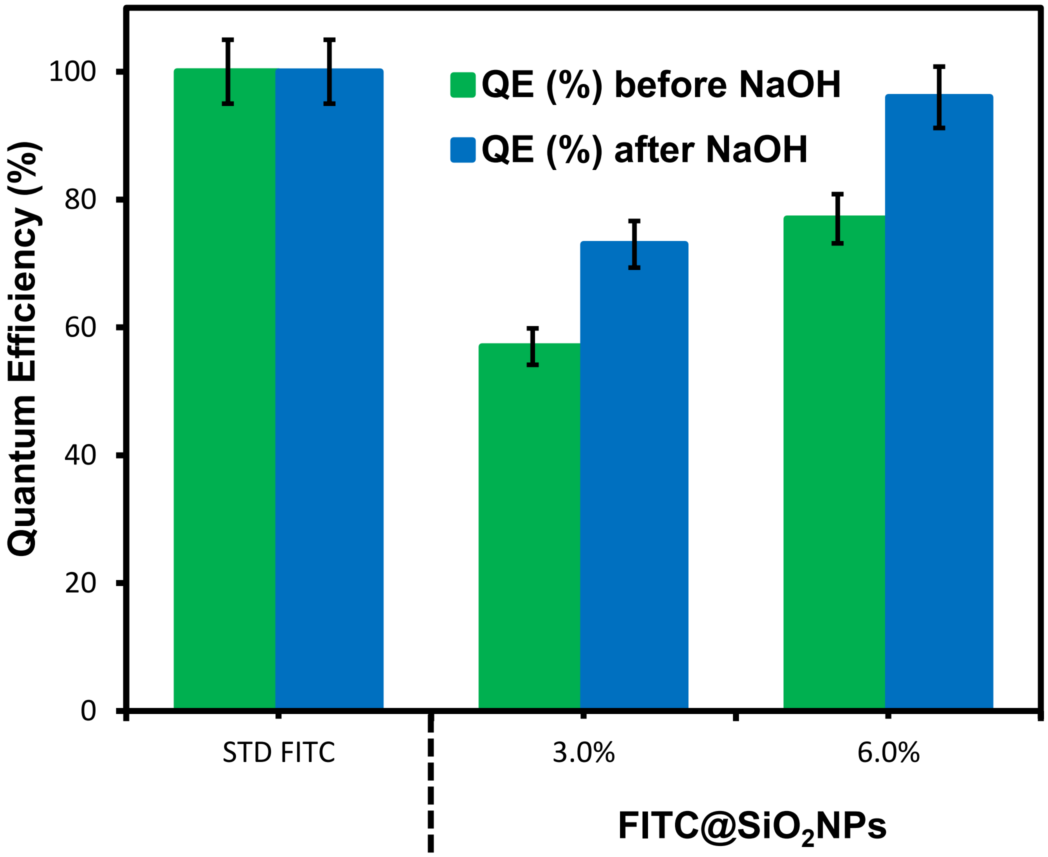

Figure 3.11: The fluorescence quantum efficiency of FITC@SiO2NPs before and after the addition of NaOH (10 mM). All samples were diluted in 10 mM PBS buffer pH (7.4) (n =3).

3.3.7 Detection of prostate-specific antigen (PSA) in buffer

The quantitative analysis of the fluorescence immunobiosensor was conducted under optimum conditions. The fluorescence-linked immunosorbent assay (FLISA) used modified black Nuc 96 microwell plates (MTP) functionalized with monoclonal *anti*-PSA-mAb as capture. The microwells were blocked for non-specific binding using 2% BSA. The sensing microwells were represented as well/*anti*-PSA-mAb/BSA. Different concentrations of the PSA were prepared and added to the modified wells to form a well/*anti*-PSA-mAb/BSA>PSA immunocomplex. Then, 6.0% FITC@SiO_2-prAmPBA-*anti*-PSA-pAb/glucose nanobioconjugates were added. The *anti*-PSA-pAb on the 6.0% FITC@SiO_2-prAmPBA-*anti*-PSA-pAb/glucose recognizes the PSA antigen leading to the formation of well/*anti*-PSA-mAb/BSA<PSA>pAb-PSA-*anti*-prAmPBA-SiO_2@FITC sandwich immunocomplex. **Scheme 3.2** shows the schematic representation of the modification of the black microwell plates with monoclonal *anti*-PSA capture antibodies and detection of PSA. The immunocomplex was washed three times to remove unbound and excess FITC@SiO_2-prAmPBA-*anti*-PSA-pAb/glucose.

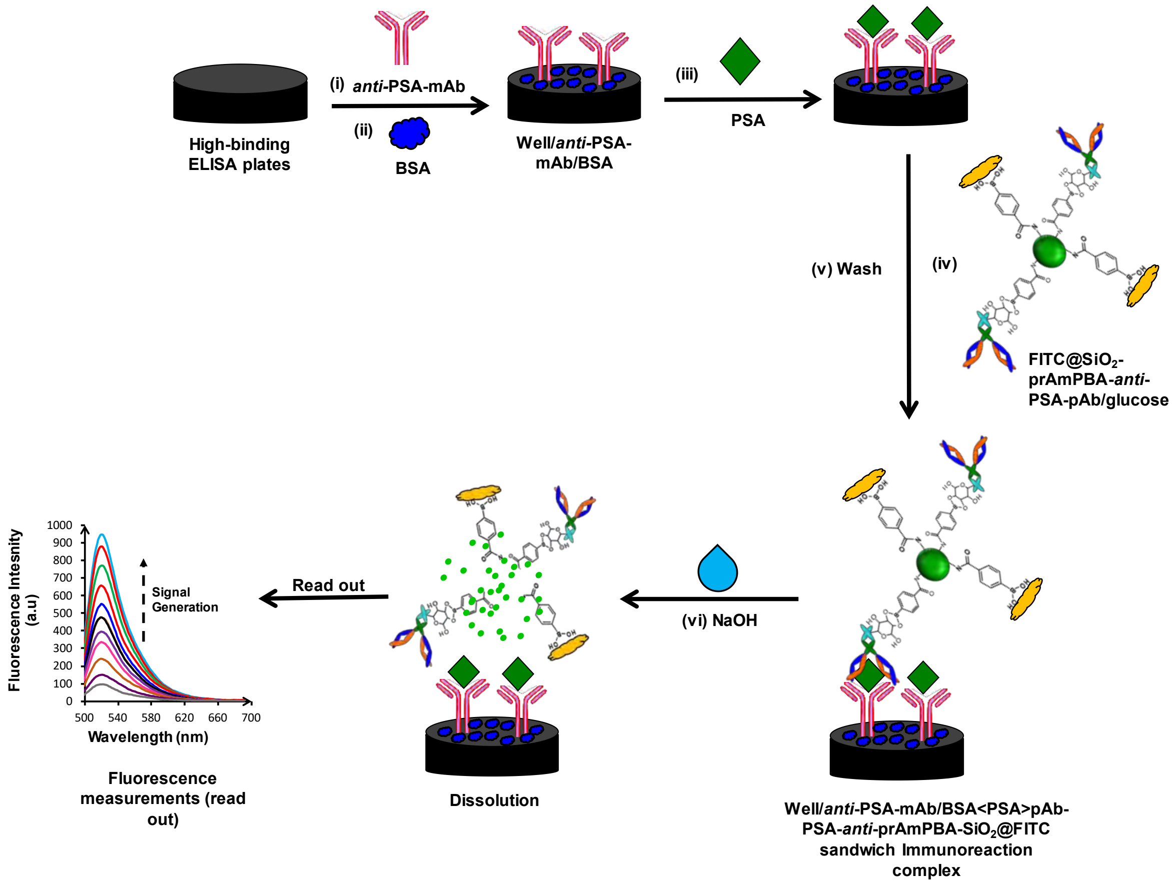

Scheme 3.2: Schematic representation of fluorescent immunobiosensor illustrating sandwich immunocomplex system. The immobilization of monoclonal antibody (*anti*-PSA-mAb), and non-specific binding sites blocked with BSA, followed by capture of PSA and sensing nanobioconjugates for PSA detection and fluorescence signal detection.

First, the fluorescence of a nanoparticle (FITC@SiO2-prAmPBA-*anti*-PSA-pAb/glucose) was measured as intact. Then, NaOH (10 mM) was added and incubated for 30 min to dissolve the silica matrix for enhanced fluorescence signals. The fluorescence signals were directly related to PSA concentration and used to quantify PSA. For the negative control, no immunocomplex formation is expected, no FITC@SiO2-prAmPBA-*anti*-PSA-pAb/glucose is captured, and no fluorescent signals are detected. **Figure 3.12** shows the fluorescence emission spectra of the fluorescent silica nanobioconjugates detection at varied concentrations of PSA (a) before, and (b) after the addition of NaOH (10 mM), and (c) the dose-response curves of the change in fluorescence intensity (ΔFI_{max}) against PSA for the varied concentrations of PSA (i) before and (ii) after the addition of NaOH (10 mM) from 2.0 pg.mL^{-1} to 50 ng.mL^{-1}. (d) The calibration curve of ΔFI_{max} against PSA concentrations. **Figure 3.12(a)** and **(b)** shows an increase in fluorescence intensity with an increase in PSA concentration from 2.0 pg.mL^{-1} to 50 ng.mL^{-1}.

Similarly, in **Fig. 3.12(c)**, the results showed a gradual increase in the fluorescence emission intensity with an increase in the PSA concentration from 2.0 pg.mL^{-1} to 50 ng.mL^{-1}. A 26-fold increase in fluorescence emission signal was observed after the addition of NaOH (10 mM). The exponential increase in signal after dissolution is as a result of the release of the encapsulated FITC-APTES fluorophores into solution. The FITC@SiO_2-prAmPBA-*anti*-PSA-pAb/glucose nanobioconjugates dissolution-based detection yielded a fluorescent intensity enhancement factor higher than the intact. **Figure 3.12(d)** shows a calibration curve obtained in the linear relationship between the relative fluorescence intensity ($\Delta FI_{max} = FI_i - FI_o$) and PSA concentrations in the range of 2.0 pg.mL^{-1} to 50 pg.mL^{-1}. The linear regression equations of both the intact and dissolution studies are expressed by **Equation (3.6)** before and **Equation (3.7)** after the dissolution.

$$\Delta FI_{max} = 48.79 \log [PSA] + 72.02, R^2 = 0.92 \qquad \textbf{(3.6)}$$

$$\Delta FI_{max} = 1290 \log [PSA] + 937.1, R^2 = 0.99 \qquad \textbf{(3.7)}$$

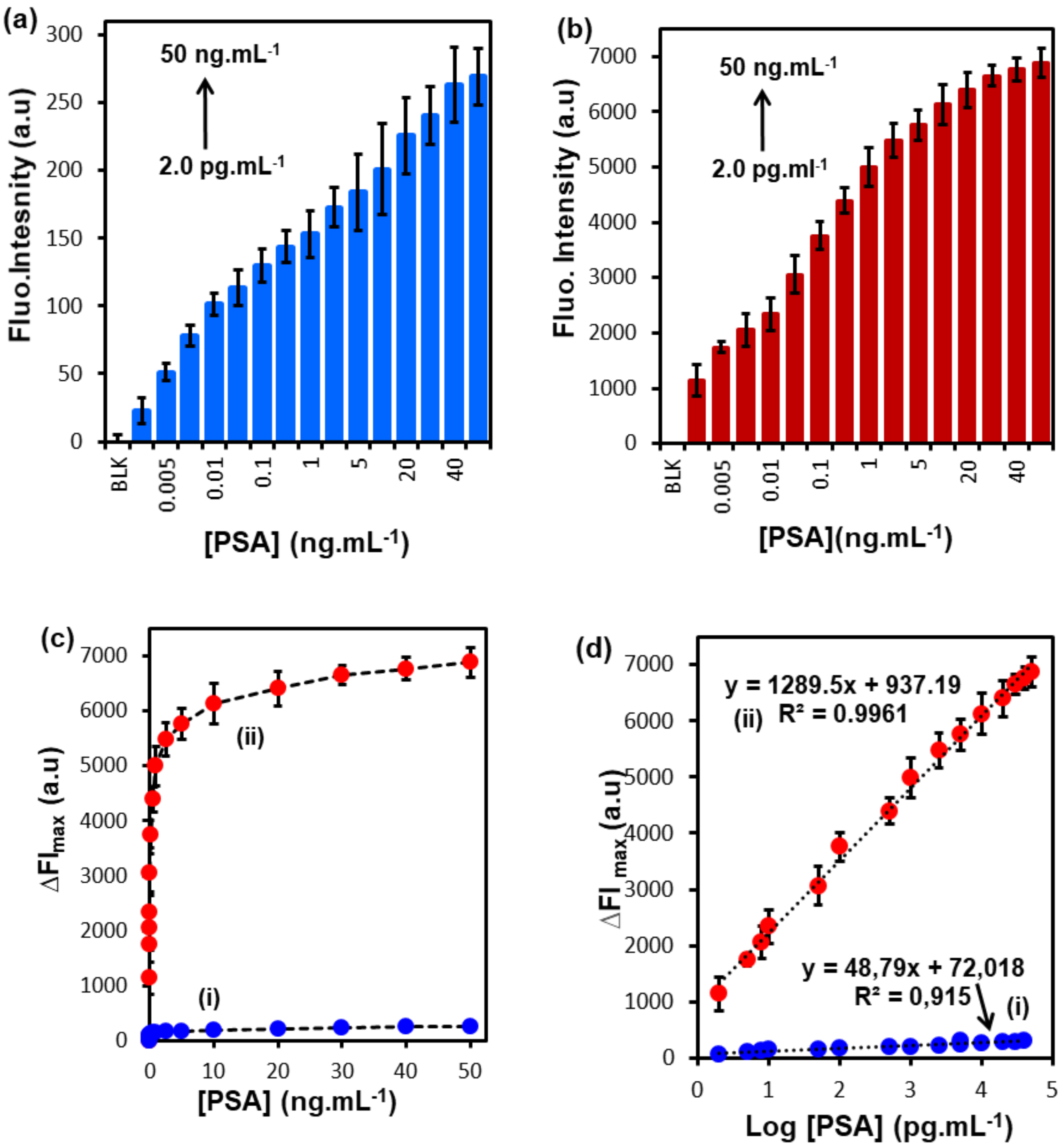

Figure 3.12: Bar graph for fluorescence emission signals for different concentrations of PSA ranging from 2.0 pg.mL^{-1} to 50 ng.mL^{-1} (a) before and (b) after dissolution with NaOH (10 mM). (c) dose-response curve of relative fluorescence intensity (ΔFI_{max}) (i) before (ii) after dissolution with NaOH (10 mM) and (d) calibration curve of relative fluorescence intensity (ΔFI_{max}) against the PSA concentrations (n = 3).

The sensitivity detection for both systems was 48.79 (a.u) pg.mL^{-1} before (intact) and 1290 (a.u) pg.mL^{-1} after adding NaOH (dissolution). This indicated that the sensitivity of the fluorescence immunobiosensor was 26-fold higher after the dissolution of the fluorescent silica nanobioconjugates. The LOD of the intact studies was calculated to be 3.43 pg.mL^{-1} with an LOQ of 10.4 pg.mL^{-1}. On the other hand, the LOD of the dissolution studies was calculated to be 0.70 pg.mL^{-1} with a LOQ of 2.12 pg.mL^{-1}. The dissolution route resulted in a higher sensitivity resulting from amplified emission fluorescence signals from released FITC molecules. The dissolution route served as the ultrasensitive detection method for PSA sensing.

3.3.8 Detection of PSA in Newborn Calf Serum (NSC) samples

The applicability of the fluorescent immunobiosensor in spiked newborn calf serum (NCS) samples was investigated. The dissolution fluorescence-linked immunosorbent assay (dissolution-FLISA) method was employed for the detection of PSA. The serum samples were diluted 10-fold with PBS buffer pH (7.4) and spiked with known concentrations of PSA ranging from 2.0 pg.mL^{-1} to 100 ng.mL^{-1}. Serum samples without the addition of PSA were used as negative controls. **Figure 3.13** shows **(a)** the fluorescence emission of different concentrations of PSA in spiked serums, **(b)** the PSA dose-response curves, and **(c)** the calibration curve of the detection of PSA in diluted serum samples (2.0 pg.mL^{-1} - 100 ng.mL^{-1}). **Figure 3.13(a)**, the fluorescence emission intensity increased with an increase in the amount of PSA concentrations spiked in the serum. The average fluorescent signal of the negative controls was 128 ± 5.3 a.u (n = 3) and the intensity with the lowest concentrations of PSA (2.0 pg.mL^{-1}) was 1202 ± 43.4 a.u (n = 3). This indicated that the method proposed could discriminate between positive and negative sera samples at low concentrations of PSA. An increase in fluorescence emission intensity relative to the increase in PSA concentration is shown in **Fig. 3.13(b)**. The calibration curve of the change in fluorescent intensity ($\Delta FI_{max} = FI_i - FI_o$) vs. the [PSA], obtained from the PSA was linear between 2.0 pg.mL^{-1} to 100 ng.mL^{-1}. A linear regression equation on the semi-log plot and the linear regression coefficient (R^2) as shown in **Equation (3.8)**.

$$\Delta FI_{max} = 1101.1 \log [PSA] + 1199.8, R^2 = 0.99 \quad \textbf{(3.8)}$$

The LOD and LOQ in newborn calf serum were calculated following a similar method as reported above. The linear concentration range of PSA detection was from 2.0 pg.mL^{-1} to 100 ng.mL^{-1}. The fluorescence immunosensor LOD was calculated to be 1.07 pg.mL^{-1} and a LOQ of 3.23 pg.mL^{-1} (n = 3). The linear ranges and LODs of the proposed fluorescence-linked immunosorbent assay (FLISA) dissolution method for detection of PSA were compared between the serum samples and PSA buffer solutions, along with previously reported methods of detection for PSA.

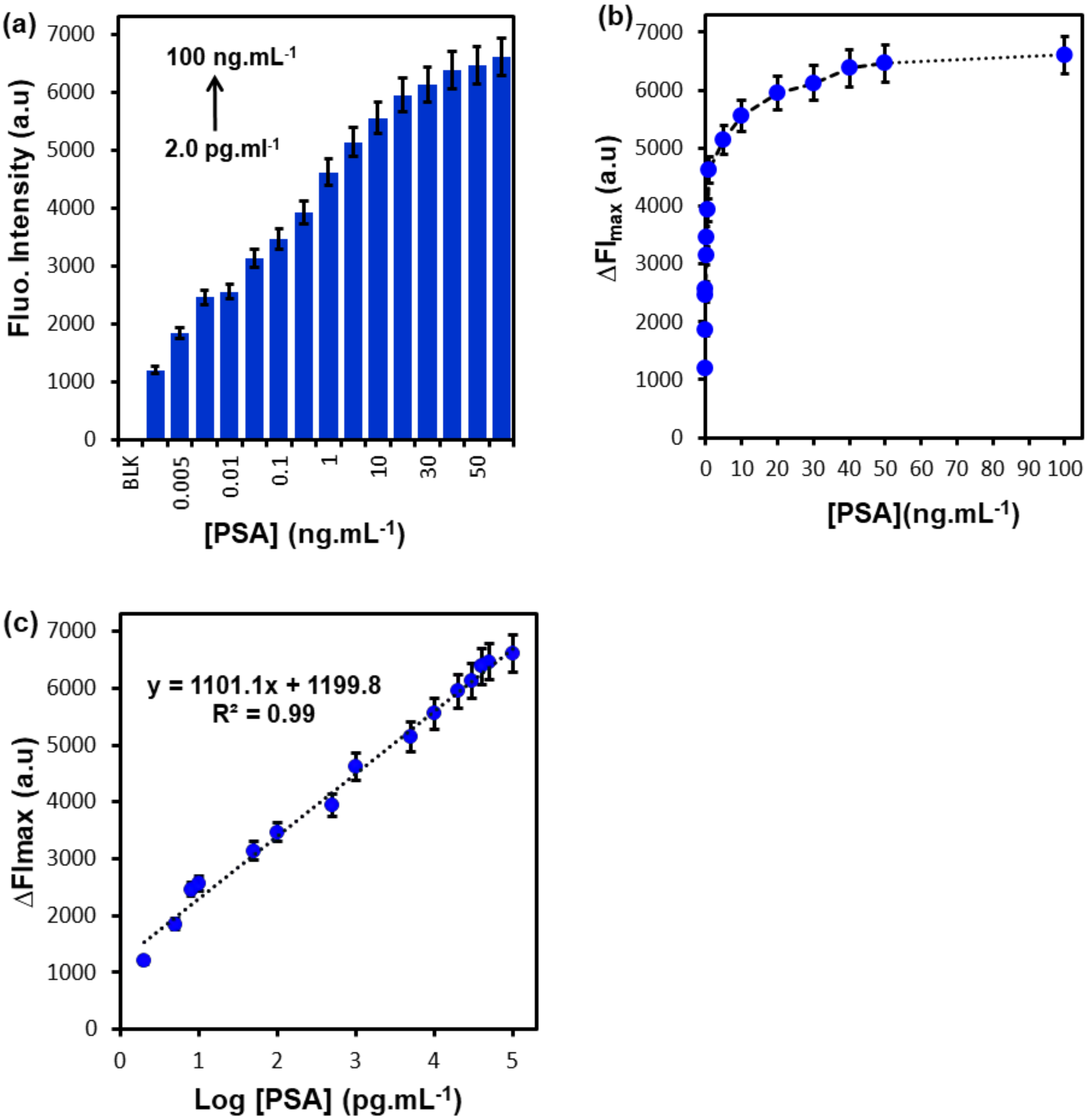

Figure 3.13: (a) Bar graph for fluorescence emission signals for different concentrations of PSA ranging from 2.0 pg.mL^{-1} to 100 ng.mL^{-1}, (b) dose-response curve of relative fluorescence intensity (ΔFI$_{max}$), and (c) calibration curve of relative fluorescence intensity (ΔFI$_{max}$) against PSA concentrations in spiked serum.

Further comparison was done with previously reported methods of detection for PSA as summarized in **Table 3.2**. The LOD of the intact studies was found to be 3.43 pg.mL^{-1} with an LOQ of 10.4 pg.mL^{-1}, and the dissolution detection method had an LOD of

0.70 pg.mL^{-1} and a LOQ of 2.12 pg.mL^{-1} in buffer (pH 7.4). The dissolution method was further employed for the detection of PSA in spiked serum samples and a LOD of 1.07 pg.mL^{-1} and a LOQ of 3.23 pg.mL^{-1} were calculated. As compared to other previously reported methods of PSA detection with LODs of 30 pg.mL^{-1} [58], 10 pg.mL^{-1} [59], and 3.0 pg.mL^{-1} [60] which employed the use of detection probes such as Mutli-CAT-AuNPs-Ab$_2$, HRP-Ab$_2$-SiO$_2$NSs, CdTe@SiO$_2$-Ab$_2$, and rGO-Ca:CdSe-Ab$_2$, respectively. In this work, the proposed FLISA biosensor gave a lower LOD of 1.07 pg.mL^{-1} for PSA detection. However, when compared to the LOD of a study by Mwanza *et al,* [61] with an LOD of 53 fg.mL^{-1} it was higher. The study employed detection probe of GENLs-anti-PSA-pAb. However, as compared to the other studies, the proposed FLISA in this study offered several advantages such as (i) simple preparation of highly fluorescent nanoparticles, (ii) photostable FITC in the silica nanoparticles, and (iii) amplified fluorescence signals after alkaline (NaOH) dissolution. Compared to the GENLs detection nanobioconjugates, fluorescein-doped silica nanobioconjugates followed a simple preparation route.

Table 3.2: A comparison of different analytical biosensors' performance for the detection of PSA.

Detection Probe	Capture substrate	Signal Monitored	Linear concentration range (LCR)	LOD	Ref.
FITC@SiO_2-prAmPBA-*anti*-PSA-pAb\glucose	well/*anti*-PSA-mAb/BSA	Fluorescence (buffer)	2.0 $pg.mL^{-1}$ - 50 ng. mL^{-1}	0.70 $pg.mL^{-1}$	[TW]
FITC@SiO_2-prAmPBA-*anti*-PSA-pab/glucose	well/*anti*-PSA-mAb/BSA	Fluorescence (serum)	2.0 $pg.mL^{-1}$ - 100 $ng.mL^{-1}$	1.07 $pg.mL^{-1}$	[TW]
Multi-CAT-AuNPs-Ab_2	MB-Ab_1	Colorimetric	50 $pg.mL^{-1}$ - 20 ng. mL^{-1}	30 pg. mL^{-1}	[58]
HRP-Ab_2-SiO_2NSs	well/Ab_1/BSA	Fluorescence	30 $pg.mL^{-1}$ - 100 ng. mL^{-1}	10 pg. mL^{-1}	[59]
CdTe@SiO_2-Ab_2	Fe_3O_4-Ab_1	Fluorescence	10 $pg.mL^{-1}$ – 5.0 $ng.mL^{-1}$	3.0 $pg.mL^{-1}$	[60]
GENLs-*anti*-PSA-pAb	well/*anti*-PSA-mAb/BSA	Colorimetric (HRP)	0.10 pg. mL^{-1} - 0.10 $g.mL^{-1}$	53 fg. mL^{-1}	[61]

TW: This work; **Multi-CAT-AuNP-Ab_2**: Polyclonal Goat *anti*-Human PSA/catalase-labelled gold nanoparticles; **HRP-Ab_2-SiO_2NSs**: Horseradish peroxidase-labelled monoclonal *anti*-PSA antibody/silicon dioxide nanospheres; **CdTe@SiO_2-Ab_2**: PSA-labelled cadmium telluride@silica core-shell nanoparticles; **GENLs-*anti*-PSA-pAb**: Polyclonal sheep *anti*-Human PSA/Glucose encapsulated nanoliposomes.

3.3.9 Selectivity and specificity for PSA detection

The specificity and selectivity of the proposed FLISA was investigated by determining the assay responses to PSA and other interfering analytes. The experimental procedure followed is similar to that of commercial ELISA assays. The serum samples were spiked with 50 ng.mL^{-1} concentration of L-Cysteine, BSA, IgG, and PSA (20 ng.mL^{-1}), respectively. Un-spiked serum samples were used as blanks. **Figure 3.14** shows the specificity and selectivity studies of the proposed fluorescence immunoassay in the presence of PSA and other analytes like proteins i.e., BSA and IgG, and other molecules like L-Cysteine. From **Fig. 3.14**, the study showed that only PSA spiked serum samples gave a significant fluorescence response, as compared to other analytes, demonstrating the excellent specificity and selectivity of the immunosensor to PSA detection.

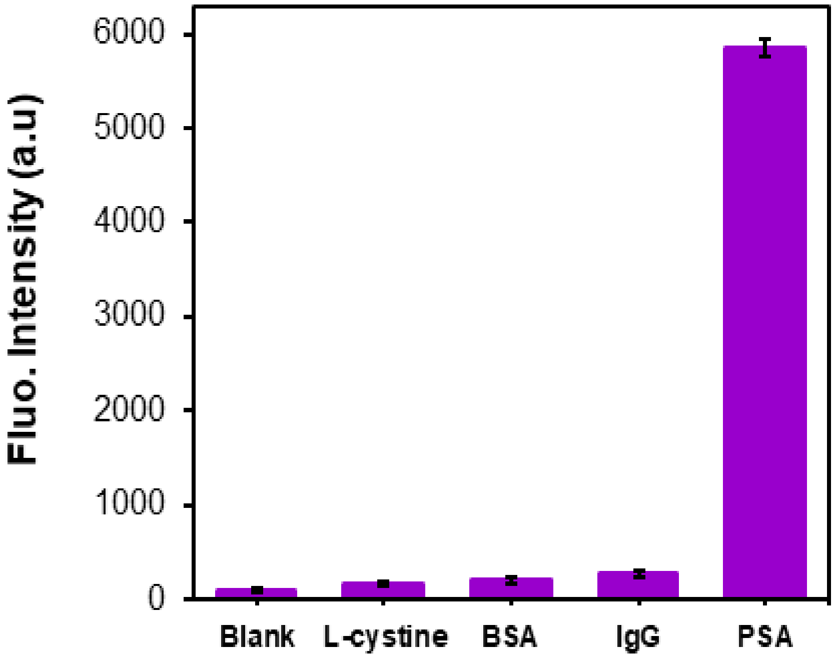

Figure 3.14: The specificity studies of the fluorescent immunoassay for the detection of PSA and other analytes (L-cysteine, BSA, IgG). (n = 3)

3.4 Conclusions

In this chapter, the work looked at developing a simple fluorescent silica antibody nanobioconjugates, FITC@SiO_2-prAmPBA-*anti*-PSA-pAb/glucose for the ultrasensitive detection of PSA. The fluorescent silica antibody nanobioconjugates utilized the use FITC-doped silica nanoparticles as the sensing nanobioconjugates for fluorescence measurements. The preparation, synthesis, optimization, and characterization of the sensing nanobioconjugates was achieved using microscopic and spectroscopic techniques. The preparation was successful as spherical and monodispersed fluorescent FITC@SiO_2-prAmPBA-*anti*-PSA-pAb/glucose nanobioconjugates were obtained with 3% and 6% fluorescence dye loadings. The fluorescent silica nanobioconjugates exhibited excellent optical stability except under alkaline conditions used for enhanced PSA detection. FITC-APTES was successfully incorporated into silica nanoparticles using the water-in-oil (w/o) microemulsion method. Further, surface functionalization of the nanoparticles was achieved using TES-prAmPBA to enable oriented bioconjugation of *anti*-PSA-pAb. The optimization of the as-prepared 3.0% and 6.0% nanoparticles showed that the 6.0% FITC-doped nanoparticles exhibited fluorescence properties with high signal amplification and sensitivity. The *anti*-PSA-pAb bioconjugated promoted specificity and selectivity for PSA antigens. The dissolution of the FITC@SiO_2-prAmPBA-*anti*-PSA-pAb/glucose using NaOH led to alkali hydrolysis of the fluorescent silica nanobioconjugates and the release of the FITC molecules into solution, resulting in amplified fluorescence signals. The combined effect of the low background noise and increased fluorescence intensity resulted in low detection limits and limit of quantification in the pg.mL^{-1}. Thus, paving a way towards early detection and diagnosis of prostate cancer.

3.5 References

[1] R.L. Siegel, K.D. Miller, A. Jemal, Cancer statistics, 2020, CA. Cancer J. Clin. 70 (2020) 7–30.

[2] F. Bray, J. Ferlay, I. Soerjomataram, R.L. Siegel, L.A. Torre, A. Jemal, Global cancer statistics 2018: GLOBOCAN estimates of incidence and mortality worldwide for 36 cancers in 185 countries, CA. Cancer J. Clin. 68 (2018) 394–424.

[3] M.S. Litwin, H.J. Tan, The Diagnosis and Treatment of Prostate Cancer, JAMA. 317 (2017) 2532 - 2542.

[4] T.R. Rebbeck, K. Burns-White, A.T. Chan, K. Emmons, M. Freedman, D.J. Hunter, P. Kraft, F. Laden, L. Mucci, G. Parmigiani, D. Schrag, S. Syngal, R.M. Tamimi, K. Viswanath, M.B. Yurgelun, J.E. Garber, Precision Prevention and Early Detection of Cancer: Fundamental Principles, Cancer Discov. 8 (2018) 803–811.

[5] J.L. Descotes, Diagnosis of prostate cancer, Asian J. Urol. 6 (2019) 129-136.

[6] S.W. Oh, Y.M. Kim, H.J. Kim, S.J. Kim, J.-S. Cho, E.Y. Choi, Point-of-care fluorescence immunoassay for prostate specific antigen, Clin. Chim. Acta. 406 (2009) 18–22.

[7] Y. Gao, J. Xie, H. Chen, S. Gu, R. Zhao, J. Shao, L. Jia, Nanotechnology-based intelligent drug design for cancer metastasis treatment, Biotechnol. Adv. 32 (2014) 761–777.

[8] G. Ertürk, M. Hedström, M.A. Tümer, A. Denizli, B. Mattiasson, Real-time prostate-specific antigen detection with prostate-specific antigen imprinted capacitive biosensors, Anal. Chim. Acta. 891 (2015) 120–129.

[9] P. D’Orazio, Biosensors in clinical chemistry - 2011 update, Clin. Chim. Acta. 412 (2011) 1749–1761.

[10] Z. Yin, L. Zhu, Z. Lv, M. Li, D. Tang, Persistent luminescence nanorods-based autofluorescence-free biosensor for prostate-specific antigen detection, Talanta. 233 (2021) 122563.

[11] T. Steuber, P. Helo, H. Lilja, Circulating biomarkers for prostate cancer, World J. Urol. 25 (2007) 111–119.

[12] M.W. Farha, S.S. Salami, Biomarkers for prostate cancer detection and risk stratification, Ther. Adv. Urol. 14 (2022) 175628722211039.

[13] N. V. Panini, G.A. Messina, E. Salinas, H. Fernández, J. Raba, integrated microfluidic systems with an immunosensor modified with carbon nanotubes for detection of prostate specific antigen (PSA) in human serum samples, Biosens. Bioelectron. 23 (2008) 1145–1151.

[14] U.H. Stenman, J. Leinonen, W.M. Zhang, P. Finne, Prostate-specific antigen, Semin. Cancer Biol. 9 (1999) 83–93.

[15] T.J. Polascik, J.E. Oesterling, A.W. Partin, Prostate specific antigen: A decade of discovery-what we have learned and where we are going, J. Urol. 162 (1999) 293–306.

[16] K.W. Watt, P.J. Lee, T. M'Timkulu, W.P. Chan, R. Loor, Human prostate-specific antigen: structural and functional similarity with serine proteases., Proc. Natl. Acad. Sci. 83 (1986) 3166–3170.

[17] H. Lilja, A. Christensson, U. Dahlén, M.T. Matikainen, O. Nilsson, K. Pettersson, T. Lövgren, Prostate-specific antigen in serum occurs predominantly in complex with alpha 1-antichymotrypsin, Clin. Chem. 37 (1991) 1618–1625.

[18] S. Raoofi Mohseni, F. Golsaz-Shirazi, M. Hosseini, J. Khoshnoodi, T. Bahadori, M.A. Judaki, M. Jeddi-Tehrani, F. Shokri, Characterization of Monoclonal and

Polyclonal Antibodies Recognizing Prostate Specific Antigen: Implication for Design of a Sandwich ELISA., Avicenna J. Med. Biotechnol. 11 (2019) 72–79.

[19] E.A. Stura, B.H. Muller, M. Bossus, S. Michel, C. Jolivet-Reynaud, F. Ducancel, Crystal Structure of Human Prostate-Specific Antigen in a Sandwich Antibody Complex, J. Mol. Biol. 414 (2011) 530–544.

[20] K. Jung, B. Brux, M. Lein, B. Rudolph, G. Kristiansen, S. Hauptmann, D. Schnorr, S.A. Loening, P. Sinha, Molecular Forms of Prostate-specific Antigen in Malignant and Benign Prostatic Tissue: Biochemical and Diagnostic Implications, Clin. Chem. 46 (2000) 47–54.

[21] H.J. Linton, L.S. Marks, L.S. Millar, C.L. Knott, H.G. Rittenhouse, S.D. Mikolajczyk, Benign Prostate-specific Antigen (BPSA) in Serum Is Increased in Benign Prostate Disease, Clin. Chem. 49 (2003) 253–259.

[22] J. Constantinou, M.R. Feneley, PSA testing: an evolving relationship with prostate cancer screening, Prostate Cancer Prostatic Dis. 9 (2006) 6–13.

[23] L.I. Stowell, L.E. Sharman, K. Hamel, An enzyme-linked immunosorbent assay (ELISA) for prostate-specific antigen, Forensic Sci. Int. 50 (1991) 125–138.

[24] J. Liang, C. Yao, X. Li, Z. Wu, C. Huang, Q. Fu, C. Lan, D. Cao, Y. Tang, Silver nanoprism etching-based plasmonic ELISA for the high sensitive detection of prostate-specific antigen, Biosens. Bioelectron. 69 (2015) 128–134.

[25] D. Sadighbayan, K. Sadighbayan, M.R. Tohid-kia, A.Y. Khosroushahi, M. Hasanzadeh, Development of electrochemical biosensors for tumor marker determination towards cancer diagnosis: Recent progress, TrAC Trends Anal. Chem. 118 (2019) 73–88.

[26] S. Zhang, P. Du, F. Li, Detection of prostate specific antigen with 3,4-diaminobenzoic acid (DBA)–H_2O_2–HRP voltammetric enzyme-linked immunoassay system, Talanta. 72 (2007) 1487–1493.

[27] X.H. Pham, E. Hahm, K.-H. Huynh, B.S. Son, H.-M. Kim, B.H. Jun, Sensitive Colorimetric Detection of Prostate Specific Antigen Using a Peroxidase-Mimicking Anti-PSA Antibody Coated Au Nanoparticle, BioChip J. 14 (2020) 158–168.

[28] N. Xia, D. Deng, Y. Wang, C. Fang, S.J. Li, Gold nanoparticle-based colorimetric method for the detection of prostate-specific antigen, Int. J. Nanomedicine. Volume 13 (2018) 2521–2530.

[29] P.Y. You, F.C. Li, M.H. Liu, Y.H. Chan, Colorimetric and Fluorescent Dual-Mode Immunoassay Based on Plasmon-Enhanced Fluorescence of Polymer Dots for Detection of PSA in Whole Blood, ACS Appl. Mater. Interfaces. 11 (2019) 9841–9849.

[30] D. Damborska, T. Bertok, E. Dosekova, A. Holazova, L. Lorencova, P. Kasak, J. Tkac, Nanomaterial-based biosensors for detection of prostate specific antigen, Microchim. Acta. 184 (2017) 3049–3067.

[31] D. Wu, A.C. Sedgwick, T. Gunnlaugsson, E.U. Akkaya, J. Yoon, T.D. James, Fluorescent chemosensors: the past, present and future, Chem. Soc. Rev. 46 (2017) 7105–7123.

[32] K. Kerman, T. Endo, M. Tsukamoto, M. Chikae, Y. Takamura, E. Tamiya, Quantum dot-based immunosensor for the detection of prostate-specific antigen using fluorescence microscopy, Talanta. 71 (2007) 1494–1499.

[33] Y. Chen, X. Guo, W. Liu, L. Zhang, Paper-based fluorometric immunodevice with quantum-dot labeled antibodies for simultaneous detection of carcinoembryonic antigen and prostate specific antigen, Microchim. Acta. 186 (2019) 112.

[34] M.K. Wagner, F. Li, J. Li, X.F. Li, X.C. Le, Use of quantum dots in the development of assays for cancer biomarkers, Anal. Bioanal. Chem. 397 (2010) 3213–3224.

[35] I. V. Koktysh, Y.I. Melnikova, O.S. Kulakovich, A.A. Ramanenka, S. V. Vaschenko, A.O. Muravitskaya, S. V. Gaponenko, S.A. Maskevich, Highly Sensitive Immunofluorescence Assay of Prostate-Specific Antigen Using Silver Nanoparticles, J. Appl. Spectrosc. 87 (2020) 870–876.

[36] D. Liu, X. Huang, Z. Wang, A. Jin, X. Sun, L. Zhu, F. Wang, Y. Ma, G. Niu, A.R. Hight Walker, X. Chen, Gold Nanoparticle-Based Activatable Probe for Sensing Ultralow Levels of Prostate-Specific Antigen, ACS Nano. 7 (2013) 5568–5576.

[37] X. Li, L. Wei, L. Pan, Z. Yi, X. Wang, Z. Ye, L. Xiao, H.-W. Li, J. Wang, Homogeneous Immunosorbent Assay Based on Single-Particle Enumeration Using Upconversion Nanoparticles for the Sensitive Detection of Cancer Biomarkers, Anal. Chem. 90 (2018) 4807–4814.

[38] S. Veeranarayanan, A. Cheruvathoor Poulose, S. Mohamed, A. Aravind, Y. Nagaoka, Y. Yoshida, T. Maekawa, D.S. Kumar, FITC Labeled Silica Nanoparticles as Efficient Cell Tags: Uptake and Photostability Study in Endothelial Cells, J. Fluoresc. 22 (2012) 537–548.

[39] V. Gubala, G. Giovannini, F. Kunc, M.P. Monopoli, C.J. Moore, Dye-doped silica nanoparticles: synthesis, surface chemistry and bioapplications, Cancer Nanotechnol. 11 (2020) 1.

[40] H.M.E. Azzazy, M.M.H. Mansour, S.C. Kazmierczak, From diagnostics to therapy: Prospects of quantum dots, Clin. Biochem. 40 (2007) 917–927.

[41] I. Miletto, A. Gilardino, P. Zamburlin, S. Dalmazzo, D. Lovisolo, G. Caputo, G. Viscardi, G. Martra, Highly bright and photostable cyanine dye-doped silica nanoparticles for optical imaging: Photophysical characterization and cell tests, Dye. Pigment. 84 (2010) 121–127.

[42] C.L. O’Connell, R. Nooney, C. McDonagh, Cyanine5-doped silica nanoparticles as ultra-bright immunospecific labels for model circulating tumour cells in flow cytometry and microscopy, Biosens. Bioelectron. 91 (2017) 190–198.

[43] C.J. Xie, D.G. Yin, J. Li, L. Zhang, B.H. Liu, M.H. Wu, Preparation of A Novel Type of Fluorescein Isothiocyanate-Doped Fluorescent Silica Nanoparticle, and Its Application as pH Probe, Chinese J. Anal. Chem. 38 (2010) 488–492.

[44] P.D.K.P. Ananda, A. Tillekaratne, C. Hettiarachchi, N. Lalichchandran, Sensitive detection of *E. coli* using bioconjugated fluorescent silica nanoparticles, Appl. Surf. Sci. Adv. 6 (2021) 100159.

[45] L. Min, L. Zhao-Yue, L. Qiang, Y. Hang, M. Lan, L. Jing-Hong, B. Yu-Bai, L. Tie-Jin, Functionalized Fluorescein-doped SiO_2 Nanoparticles for Immunochromatographic Assay, Chinese J. Chem. 23 (2005) 875–880.

[46] C.J. Moore, G. Giovannini, F. Kunc, A.J. Hall, V. Gubala, ‘Overloading’ fluorescent silica nanoparticles with dyes to improve biosensor performance, J. Mater. Chem. B. 5 (2017) 5564–5572.

[47] A. Van Blaaderen, A. Vrij, Synthesis and characterization of colloidal dispersions of fluorescent, monodisperse silica spheres, Langmuir. 8 (1992) 2921–2931.

[48] L. Friedrichs, A simple cleaning and fluorescent staining protocol for recent and fossil diatom frustules, Diatom Res. 28 (2013) 317–327.

[49] O.K. Adeniyi, A. Ngqinambi, P.N. Mashazi, Ultrasensitive detection of anti-p53 autoantibodies based on nanomagnetic capture and separation with fluorescent

sensing nanobioprobe for signal amplification, Biosens. Bioelectron. 170 (2020) 112640.

[50] X. Zhao, R.P. Bagwe, W. Tan, Development of Organic-Dye-Doped Silica Nanoparticles in a Reverse Microemulsion, Adv. Mater. 16 (2004) 173–176.

[51] F. Duval, T.A. van Beek, H. Zuilhof, Key steps towards the oriented immobilization of antibodies using boronic acids, Analyst. 140 (2015) 6467–6472.

[52] W. Wei, M. Wei, S. Liu, Silica nanoparticles as a carrier for signal amplification, Rev. Anal. Chem. 31 (2012) 163 - 176.

[53] A. Auger, J. Samuel, O. Poncelet, O. Raccurt, A comparative study of non-covalent encapsulation methods for organic dyes into silica nanoparticles, Nanoscale Res. Lett. 6 (2011) 328.

[54] E. Gök, S. Olgaz, Binding of Fluorescein Isothiocyanate to Insulin: A Fluorimetric Labeling Study, J. Fluoresc. 14 (2004) 203–206.

[55] I. Suzuki, Infrared Spectra and Normal Vibrations of Thioamides. III. N -Methylthioformamide and N -Methylthioacetamide, Bull. Chem. Soc. Jpn. 35 (1962) 1456–1464.

[56] G. Giovaninni, C.J. Moore, A.J. Hall, H.J. Byrne, V. Gubala, pH-Dependent silica nanoparticle dissolution and cargo release, Colloids Surfaces B Biointerfaces. 169 (2018) 242–248.

[57] A. Shrivastava, V. Gupta, Methods for the determination of limit of detection and limit of quantitation of the analytical methods, Chronicles Young Sci. 2 (2011) 21 - 25.

[58] Z. Gao, M. Xu, L. Hou, G. Chen, D. Tang, Magnetic Bead-Based Reverse Colorimetric Immunoassay Strategy for Sensing Biomolecules, Anal. Chem. 85 (2013) 6945–6952.

[59] L. Li, W. Zhang, Y. Wei, L. Yu, D. Feng, A Sensitive Fluorescent Immunoassay for Prostate Specific Antigen Detection Based on Signal Amplify Strategy of Horseradish Peroxidase and Silicon Dioxide Nanospheres, J. Anal. Methods Chem. 2022 (2022) 6209731.

[60] Y. Zhao, W. Gao, X. Ge, S. Li, D. Du, H. Yang, CdTe@SiO_2 signal reporters-based fluorescent immunosensor for quantitative detection of prostate specific antigen, Anal. Chim. Acta. 1057 (2019) 44 - 50.

[61] D. Mwanza, N. Mfamela, O. Adeniyi, T. Nyokong, P. Mashazi, Ultrasensitive detection of prostate-specific antigen using glucose-encapsulated nanoliposomes anti-PSA polyclonal antibody as detection nanobioprobes, Talanta 245 (2022) 123483.

Chapter 4

4 Nanomagnetic-silica antibody conjugates as capture for PSA and detection using for dissolution fluorescence-linked immunosorbent assay

Abstract

A simple, ultrasensitive fluorescence immunobiosensor was developed for the detection of prostate-specific antigen (PSA). The immunosensor platform was based on the immunometric sandwich protocol, using nanomagnetic-silica nanoparticles as capture and fluorescent silica nanoparticles as detection probes. The specificity was achieved using *anti*-PSA-mAb bioconjugated to phenylboronic acid functionalized nanomagnetic-silica nanoparticles, with non-binding sites blocked with glucose (Fe_3O_4@SiO_2-prAmPBA-*anti*-PSA-mAb/glucose) for capture and magnetic separation. *Anti*-PSA-pAb bioconjugated onto phenylboronic acid functionalized FITC-doped silica nanoparticles (FITC@SiO_2-prAmPBA-*anti*-PSA-pAb/glucose) were used as the sensing nanobioconjugates. The Fe_3O_4@SiO_2-prAmPBA-*anti*-PSA-mAb/glucose was used to capture the PSA analytes and selectively isolated using a magnet. A sandwich-type immunoreaction was achieved via the Fc-specific of FITC@SiO_2-prAmPBA-*anti*-PSA-pAb binding to the captured PSA analyte. The alkali hydrolysis of the FITC@SiO_2-prAmPBA-*anti*-PSA-pAb/glucose was achieved using NaOH. The release of FITC molecules leads to an amplified fluorescence detection signal. The analytical performance of the proposed immunobiosensor showed a good linear relationship between the fluorescence intensity and the target PSA concentration ranging from 2.0 pg.mL^{-1} to 100 ng.mL^{-1}. The limit of detection (LOD) was low and 0.81 pg.mL^{-1} and the limit of quantification (LOQ) was 2.46 pg.mL^{-1}. The sensor also exhibited good specificity and selectivity to PSA with 94.8% – 102.5%

recovery rates. Therefore, the fluorescence immunobiosensor exhibited highly sensitive and specific detection properties for prostate-specific antigen (PSA) and a good detection platform in serum samples.

4.1 Introduction

Prostate cancer (PCa) is the most frequently diagnosed male malignancy and the second leading cause of cancer deaths worldwide [1–4]. According to the International Agency for Research on Cancer (IARC) and Global Cancer Statistics (GLOBOCAN), about 1.4 million newly diagnosed cases and 375,000 prostate cancer-related deaths were reported worldwide in 2020 [3–6]. The most common methods of prostate cancer diagnosis are digital rectal examination (DRE), tissue biopsy, and PSA screening is the most promising method for prostate-specific antigen (PSA) cancer diagnosis [7,8]. The first two methods DRE and tissue biopsy are invasive and non-specific as benign cancer can be diagnosed as prostate cancer [9–11]. In addition, using DRE and tissue biopsy only discovers prostate cancer once a mass or tumour has formed and metastasized [12]. At these stages of cancer formation stage III to stage IV chemotherapy is not effective, and reoccurrence is high. Prostate-specific antigen (PSA) is an androgen protease produced by both normal prostate and cancer cells [8,13] PSA is used clinically as an effective biomarker for prostate cancer screening and monitoring [14–16]. In cancer patients, elevated levels of PSA in the serum above 4.0 ng.mL^{-1} are considered to be at higher risk of developing prostate cancer [17,18]. Therefore, a precise detection and quantification of PSA from the onset of cancer carcinogenesis is important for the early diagnosis and monitoring of the progression of prostate cancer. Biosensors are sensing systems capable of detecting ultra-low concentrations of PSA in patients' serum and have been used in research to improve the early detection of prostate cancer. For example, Zhao *et al* [19] designed a fluorescent quantum dots immunosensor as the detection probe. Fe_3O_4NPs nanocomposites were used as the capture probe for the detection of PSA antigen at low concentrations. The biosensor used quantum dots (QDs) which contain heavy toxic metals like cadmium (Cd) and limiting their applications in biological systems [20]. Herein, we report the use of fluorescein-5-isothiocyanate (FITC) as a fluorophore. FITC-doped silica nanoparticles were prepared and used as sensing nanobioconjugates. Furthermore, for enhanced selectivity and sensitivity towards the detection of PSA, nanomagnetic-silica nanoparticles are incorporated as capture bioprobes.

Nanomagnetic-silica nanoparticles as capture bioprobes have been investigated for various medical applications [21–23]. They are advantageous for use in biodetection due to their facile synthesis, small size, stability, good monodispersity, low toxicity, and high magnetic moment [22-24]. They provide an easy way to separate samples from solutions using a magnet [25–27]. Nanomagnetic-silica capture bioprobes contain iron oxide nanoparticles at the core and silica shell. Iron oxide nanoparticles (Fe_3O_4NPs) alone are used in biomedical applications for magnetic resonance imaging (MRI), biomolecular separation, and target-drug delivery [21–29]. This is due to their superparamagnetic properties, controllable particle size (nano-sized nature), and huge surface-specific area [21–30]. However, magnetic Fe_3O_4NPs used in bioapplications are required to be chemically stable and functional for in vivo applications [31,32]. Bare Fe_3O_4NPs are prone to agglomeration, air oxidation, and biodegradation [31–33]. To overcome such limitations surface functionalization has been shown to be successful [30–33]. Silica (SiO_2) is a widely used coating shell or material for magnetic nanoparticles [22,23,26,31–36]. The encapsulation of magnetic Fe_3O_4NPs within a silica shell have been shown to significantly reduce the agglomeration of bare Fe_3O_4NPs and improve their performance in solution. This is because of the SiO_2 nanoparticle's unique properties which provide good stability, hydrophilicity, and biocompatibility, ease of surface modification, and helps prevent unwanted interactions with the magnetic core [30–37]. Moreover, the silica shell provides stability for the magnetic nanoparticles in the core shell and allows for surface modification, attachment of organic molecules, ligands [37]. In this work, the surface functionalization of the silica shell was achieved using affinity ligands which allows for a controlled molecular orientation of the antibody. $Fe_3O_4@SiO_2$NPs, was functionalized by direct covalent immobilization with phenylboronic acid for oriented antibody immobilization [36]. The boronic acid functionalized nanomagnetic materials have been shown to form strong covalent bonds with the N-glycosylated groups on the Fc region of the antibody selectivity [38,39]. Bioconjugation of *anti*-PSA-mAb forms cis-diol bonds with the boronic acid and provides for high selectivity and specificity for antibody-to-antigen interactions for the nanobioprobes [40].

Reports have shown that, the bioconjugation with antibodies is advantageous in biomedical application such as in diagnostics and targeted therapy. This is due to their high specificty, selectivity in bioassay applications and allowing the antibody fucntionalized-$Fe_3O_4@SiO_2$NPs to act as caputre bioprobes and used for the isolation of the target analyte from complex matrices, enhancing the effectiveness of analyte isolation and concentration, minimizes matrix effects due to simplified washing and separation procedures, allows faster assays kinetics, improves the sensitvity and limit of detection (LOD), and reduces the time for analysis [41-43].

In our previous work, the FITC@SiO_2-prAmPBA-*anti*-CRP-pAb/glucose and *anti*-P53-pAb/glucose sensing nanobioprobes were synthesized and characterized [36,44]. In this chapter, the nanomagnetic-silica as capture nanomaterials were prepared and coated with phenylboronic acid for attachment of *anti*-PSA monoclonal antibodies. The use of nanomagnetic-silica nanoparticles as capture bioprobes provide rapid separation using a magnet. The active mixing of the nanomagnetic silica capture in analytes solution promotes faster immunoreaction, higher fluorescence signals, and lower detection limits compared to immunocapture on two-dimensional surfaces such as the conventional ELISA microwells [45,46]. The use of fluorescent silica nanoparticles as the sensing nanobioconjugates provide the fluorescence signals. The silica shell dissolution using NaOH releases the FITC molecules, resulting in amplified fluorescence signals. In this work, we utilized *anti*-PSA-mAb functionalized nanomagnetic-silica nanoparticles as the capture bioprobes and *anti*-PSA-pAb functionalized fluorescent nanoparticles as the sensing nanobioconjugates. A sandwich-type fluorescence immunobiosensor was developed and assessed for selective detection of PSA. The novelty of the work is in the detection of PSA using sandwich immunoassay with fluorescent dye-doped silica nanoparticles and nanomagnetic-silica nanoparticles (magnetic separation) for analyte capture.

This chapter was set out to achieve the following objectives of the thesis

(a) Synthesis of nanomagnetic-silica antibody capture bioprobes (Fe_3O_4@SiO_2-prAmPBA-*anti*-PSA-mAb/glucose).

(b) Characterise the nanomagnetic-silica capture bioprobes.

(c) Detection of PSA using the dissolution route of the FITC@SiO_2-prAmPBA-*anti*-PSA-pAb/glucose sensing nanobioconjugates in a FLISA immunobiosensor set up in both buffer solution and serum samples (Newborn Calf Serum, NCS).

(d) Evaluate the analytical performance of the immunosensor in the presence of both the nanomagnetic-silica capture bioprobes and fluorescent silica antibody sensing nanobioconjugates.

4.2 Experimental

4.2.1 Materials and reagents

Iron (III) Chloride ($FeCl_3.2H_2O$), Sodium oleate, Oleic acid (90%), 1-octadecene (90%), (3-aminopropyl) triethoxysilane (APTES, 98%), tetraethyl orthosilicate (TEOS, 99.9%), 4-carboxyphenylboronic acid, Sodium chloride (NaCl), 4-(1,1,3,3-tetramethyl butyl)-phenyl polyethylene glycol (Triton X-100), N-hydroxysuccinimide (NHS), 1-ethyl-3(3-dimethyl aminopropyl)-carbodiimide (EDC), Sodium hydroxide (NaOH), and Bovine serum albumin (BSA) were purchased from Sigma-Aldrich (USA). Absolute ethanol (98.6.0%, w/v), sodium dihydrogen phosphate (NaH_2PO_4), disodium hydrogen phosphate (Na_2HPO_4), and D-glucose anhydrous were purchased from SAARChem (South Africa). Cyclohexane (99.5%), Deuterated dimethyl sulfoxide (d_6-DMSO), and toluene were purchased from Merck (Germany). Hexan-1-ol was purchased from B&M Scientific (South Africa). Ammonium hydroxide (NH_4OH, 25% wt) was purchased from Minema Chemicals (South Africa). Mouse *anti*-human Prostate-Specific Antibody (*anti*-PSA-mAb, 7820-0370) and Bradford reagent (for Bradford assay) were purchased from Bio-Rad Laboratories (USA). Coupling buffer phosphate buffer solution (PBS, pH 7.4,10 mM) was prepared using 0.63 g disodium hydrogen phosphate (Na_2HPO_4), 0.06 g sodium dihydrogen phosphate (NaH_2PO_4) in 400 mL of distilled water. Washing buffer, (PBST, pH 7.4, 10 mM) was prepared using 1.2 g disodium hydrogen phosphate (Na_2HPO_4), 0.12 g sodium dihydrogen orthophosphate (NaH_2PO_4), and 100µL of Tween 20 in 100 mL of ultra-pure Millipore water. All reagents and solvents in this study were of analytical grade and used as received from the supplier. Ultra-pure water with a resistivity of 18 MΩ.cm (at 25°C) was obtained from a Milli-Q Water Purification System (Millipore Corp. Bedford, MA, USA) and was used for the preparations of aqueous solutions throughout the experiments. The synthesis of the fluorescent FITC@SiO_2NPs nanoparticles was prepared in Chapter 3. In this work, FITC@SiO_2NPs contained 6.0% dye loadings. The functionalization with boronic group and antibody bioconjugation to yield FITC@SiO_2-prAmPBA-*anti*-PSA-pAb as sensing nanobioconjugates will be discussed.

4.2.2 Apparatus and Instrumentations

Infra-red spectra were collected on a Perkin-Elmer Universal ART sampling accessory spectrum 100 FT-IR spectrometer. Zeta-potential measurements were carried out on a Malvern Zetasizer Nano series, Nano ZS90 series S equipped with a 633 nm He/Ne laser. Scanning electron microscopy (SEM) and Energy dispersive X-ray spectroscopy (SEM-EDS) images and elemental mapping were carried out using an INCA PENTA FET coupled to the VAGA TESCAM using 20 kV accelerating voltage. The X-ray powder diffraction (XRD) patterns were recorded on a Bruker D8 Discover equipped with a Lynx Eye detector, using Cu-KA radiation (1.5405 A°, nickel filter). The data was collected in the range from $2\theta = 10^o$ to 90^o, scanning at 1^o min^{-1} with a filter time-constant of 2.5 seconds per step and a slit width of 6.0 mm. Samples were placed on a silicon wafer slide. The XRD data was treated using the freely available Eva (evaluation curve fitting) software. Baseline correction was performed on each diffraction patterns by subtracting a spline fitted to the curve background. UV-Visible (UV-Vis) spectroscopy analysis was acquired on a SHIMADZU UV-2550 spectrometer. ^{1}H NMR spectra analysis was recorded using a Bruker AVANCE 600 MHZ NMR spectrometer in DMSO-d_6. The fluorescence spectra were recorded using a spectramax multitude spectrofluorometer and synergy MX microplate reader.

4.2.3 Preparation of *anti*-PSA-mAb nanomagnetic-silica nanoparticles (Fe_3O_4@SiO_2-prAmPBA-*anti*-PSA-mAb/glucose), Scheme 4.1

4.2.3.1 Synthesis of oleic-capped magnetic nanoparticles (Fe_3O_4NPs)

Fe_3O_4NPs were prepared following a reported method with some modifications [34]. In a typical synthesis procedure, iron (III) chloride (1.25 g, 4.62 mmol) was dissolved in distilled water (10.0 mL). Sodium oleate (5.22 g, 17.2 mmol) was added and magnetically stirred at room temperature. Ethanol (12.5 mL) and n-hexane (20.0 mL) were added to the mixture and stirred at 85°C for 4 hrs. The colour of the mixture turned dark brown from deep maroon. The resulting solution was separated using a separating funnel. A sticky reddish-brown organic layer was obtained and washed repeatedly with deionized water and oven-dried for 12 hrs at 80°C. A reddish-brown

Fe(oleate)$_3$ precursor was obtained as a solid. The sticky Fe(oleate)$_3$ precursor (3.0 g, 3.4 mmol) was dispersed in oleic acid (2.0 mL) and 1-octadecene (7.5 mL). The mixture was degassed under nitrogen gas for 30 mins at room temperature. The temperature was increased by 10^{o}C every 5 mins up to 320^{o}C. The reaction was maintained at 320^{o}C under a flowing stream of nitrogen gas for 45 mins. The resulting solution was cooled at room temperature. Ethanol (60.0 mL) was added to precipitate the oleic-capped Fe_3O_4NPs and collected by magnetic separation. The black precipitate was re-dispersed in hexane and precipitated with ethanol (10.0 mL). The re-suspension of nanoparticles in hexane and ethanol was done several times to obtain clean OA-capped-Fe_3O_4NPs. The obtained OA-Fe_3O_4NPs were collected by magnetic separation and dispersed in cyclohexane at 2.0 mg.mL^{-1}. FT-IR [ATR), τ_{max}/cm^{-1}]: 2918 (C-H), 2849 (C-H), 1545 (COO^-), 1409 (COO^-), and 562 (Fe-O).

4.2.3.2 Preparation of silica coated Fe_3O_4NPs (Fe_3O_4@SiO_2NPs)

A reverse (W/O) microemulsion method was used to encapsulate OA-Fe_3O_4NPs and prepare Fe_3O_4@SiO_2 core-shell nanoparticles. The microemulsion solution was prepared by mixing n-hexanol (1.8 mL), OA-capped Fe_3O_4NPs (2.0 mg.mL^{-1}, 4.0 mL), cyclohexane (15.0 mL), Triton X-100 (4.5 mL), and water (1.5 mL) were added into a reaction flask. The mixture was stirred for 45 mins to form a microemulsion. A transparent golden-yellow solution formed. NH_4OH (200 µL, 25 %) and TEOS (25.0 µL, 0.12 mmol) were added to the mixture and stirred for 6 hrs. Additionally, TEOS (10.0 µL, 0.056 mmol) was added every 2 hrs and six additions were used to grow a silica shell. After the last addition of TEOS, the mixture was stirred for 12 hrs at room temperature, forming Fe_3O_4@SiO_2NPs. Isolating the Fe_3O_4@SiO_2NPs was done by adjusting the pH to 2 with cooling in liquid nitrogen. Acetone (20.0 mL) was added to break the microemulsion. Fe_3O_4@SiO_2NPs were collected by centrifugation and washed with a 1:3 mixture of water and ethanol and collected by magnetic separation. The nanomagnetic-silica nanoparticles were dried overnight at 50°C in the oven and collected as a brown powder. FT-IR [ATR], τ_{max}/cm^{-1}]: 3285 (O-H), 1046 (Si-O-Si), 940 (Si-O), 797 (Si-OH), and 487 (Fe-O).

4.2.3.3 Boronic acid functionalization of nanomagnetic-silica nanoparticles (Fe_3O_4@SiO_2-prAmPBANPs)

The synthesis of Fe_3O_4@SiO_2-prAmPBANPs was achieved by first synthesizing triethoxysilanepropyl-3-amido phenylboronic acid (TES-prAmPBA) as shown in **Scheme S3.2**. Briefly, EDC (31.0 mg, 0.20 mmol), NHS (57.5 mg, 0.5 mmol), and 4-carboxypheynlboronic acid (73.0 mg, 0.43 mmol) were dissolved in dry EtOH (5.0 mL) and stirred. After 15 mins, APTES (0.2 mL, 0.86 mmol) was added dropwise into the solution. The reaction was followed using the thin layer chromatography until reagents completely reacted. The solution mixture was stirred further overnight at room temperature until TES-prAmPBA resulted, separated (centrifuged), and washed with ethanol, and oven dried at 60°C for 24 hrs. The product was obtained as a white precipitate. Yield 66%.

FT-IR [(ATR), τ_{max}/cm^{-1}]: 3228 (OH), 3265 (NH), 1643 (C=O), 1260 (B-O), and 1063 (O-Si-O). ^{1}H NMR (600 MHz, DMSO-d_6) δ [ppm]: 0.78 (2H, $SiCH_2$), 1.25 (t, 9H, CH_3), 1.96 (2H, CH_2), 2.61 (2H, NCH_2), 4.10 (q, 6H, CH_2), 7.88 (d, 2H, H-Ph), 8.18 (d, 2H, H-Ph).

Then, the synthesized TES-prAmPBA (20.0 mg, 0.080 mmol) was dissolved in ammonium solution (5.0 mL) and magnetically stirred for 10 mins. The $Fe_3O_4@SiO_2$NPs (20.0 mg) dissolved in a mixture of (9:1) dry toluene and EtOH. The two solutions were added together under stirring for 24 hrs at room temperature. This resulted in the phenylboronic functionalized nanomagnetic-silica nanoparticles ($Fe_3O_4@SiO_2$-prAmPBANPs) which were separated by magnet. $Fe_3O_4@SiO_2$-prAmPBANPs were washed several times with a 1:1 mixture of water and ethanol, and each time magnetically separated. The product was dried at 50°C for 48 hrs. FT-IR [(ATR), τ_{max}/cm^{-1}]: 3872 & 1541 (N-H), 1649 (C=O), 1386 (B-O), 1056 (Si-O-Si), 949 (Si-O), and 785 (Si-OH).

4.2.4 Bioconjugation of *anti*-PSA-mAb onto $Fe_3O_4@SiO_2$-prAmPBANPs

$Fe_3O_4@SiO_2$-prAmPBANPs (2.0 mg.mL^{-1}) were suspended in cold PBS buffer (2.0 mL, pH 7.4, 10 mM) and sonicated for 10 mins. The $Fe_3O_4@SiO_2$-prAmPBANPs solution was reacted with monoclonal *anti*-PSA antibody (50 µL, 1.0 mg.mL^{-1}) in PBS buffer (2.0 mL, pH 7.4,10 mM) for 6 hrs at 4°C under slow continuous stirring. The antibody-modified nanomagnetic-silica nanoparticles ($Fe_3O_4@SiO_2$-prAmPBA-*anti*-PSA-mAb) were washed with cold PBS (pH 7.4) to remove the unbound antibodies. The unreacted boronic acid sites were blocked by reacting the purified $Fe_3O_4@SiO_2$-

prAmPBA-*anti*-PSA-mAb with D-glucose (50 µg.mL^{-1}) in cold PBS buffer (pH 7.4,10 mM). After 2 hrs, the mixture was magnetically separated and washed with cold PBS buffer (pH 7.4,10 mM) to yield $Fe_3O_4@SiO_2$-prAmPBA-*anti*-PSA-mAb/glucose. The resulting solution was kept at 4°C before use. FT-IR [(ATR), τ_{max}/cm^{-1}]: 3355 (N-H), 1639 (amide I), 1546 (amide II), 1390 (B-O), and 457 (Fe-O).

4.2.5 Bradford assay procedure

A quantitative colorimetric assay was used to quantify the amount of the monoclonal antibody (*anti*-PSA-mAb) conjugated onto $Fe_3O_4@SiO_2$-prAmPBANPs to form $Fe_3O_4@SiO_2$-prAmPBA-*anti*-PSA-mAb. The bioconjugation of *anti*-PSA-mAb onto $Fe_3O_4@SiO_2$-prAmPBANPs was achieved through the affinity boronate ester bond reaction. The reaction targets the carbohydrate moiety of (N-glycan) of the Fc region of the *anti*-PSA monoclonal antibody. The glycosylated antibody in the Fc region was used to react with $Fe_3O_4@SiO_2$-prAmPBANPs to form cyclic ester bonds. Bradford assay was used to confirm the immobilization of the *anti*-PSA-mAb. The *anti*-PSA-mAb solution before and after conjugation were measured. The $Fe_3O_4@SiO_2$-prAmPBA-*anti*-PSA-mAb after conjugation was removed using a magnet and the supernatant was used for protein determination. Bovine Serum Albumin (BSA) standard solutions and the supernatant obtained from $Fe_3O_4@SiO_2$-prAmPBA-*anti*-PSA-mAb were made to react with Bradford reagent at room temperature for 30 mins. UV-Vis spectra were used to follow the bioconjugation of the monoclonal *anti*-PSA antibodies.

4.2.6 Preparation of the *anti*-PSA-pAb fluorescent silica antibody sensing nanobioconjugate, (FITC@SiO$_2$-prAmPBA-*anti*-PSA-pAb/glucose)

First, the fluorescent silica nanoparticles (6 %, w/w FITC@SiO$_2$NPs) were synthesised (in Chapter 3) and stored in the dark. The FITC@SiO$_2$NPs (20.0 mg) were dispersed in ethanol (5.0 mL) and stirred for 20 min. TES-prAmPBA (40.0 mg, 0.10 mmol) dissolved in ammonium solution was added to the nanoparticle ethanol solution. The resulting solution was continuously mixed at room temperature overnight in the dark. The product, phenylboronic acid functionalized-silica nanoparticles (FITC@SiO$_2$-prAmPBANPs) were obtained after centrifugation and washed several times with a 1:1 mixture of water/ethanol to remove unreacted reagents. The FITC@SiO$_2$-prAmPBANPs were oven dried at 40^{o}C for 48 hours in the dark.

In the second step, the Fc-directed oriented bioconjugation of the polyclonal antibody (*anti*-PSA-pAb) onto FITC@SiO$_2$-prAmPBANPs was achieved through the boronate ester bonds. The N-glycans on the Fc region of the *anti*-PSA-pAb was reacted with the boronic acids of fluorescence nanoparticles. Briefly, FITC@SiO$_2$-prAmPBANPs (2.0 mg) were dispersed in cold PBS buffer (2.0 mL, pH 7.4,10 mM) and stirred for 10 min. Polyclonal *anti*-PSA antibody (50 μL, 1.0 mg.mL^{-1}) was added to the solution. The mixture was kept at 4^{o}C under continuous slow stirring and allowed to react for 6 hours. The *anti*-PSA-pAb bioconjugated FITC-doped silica nanoparticles were centrifuged and washed with 4^{o}C cold PBS buffer (pH 7.4) to remove the unbound antibodies. The unreacted boronic acid sites were blocked by incubating the purified FITC@SiO$_2$-prAmPBA-*anti*-PSA-pAbNPs in 4^{o}C cold PBS (pH 7.4) containing D-glucose solution (50.0 µg.mL^{-1}, 60 mg, 0.334 mmol). After 2 hours, the mixture was centrifuged and washed three times with 4°C cold PBS buffer (pH 7.4, 10 mM). This yielded *anti*-PSA-pAb/glucose modified FITC-doped silica nanobioconjugates, represented as FITC@SiO_2-prAmPBA-*anti*-PSA-pAb/glucose. FITC@SiO_2-prAmPBA-*anti*-PSA-pAb/glucose was suspended in PBS buffer (2.0 mL, pH 7.4, 10 mM) and kept at 4°C before use.

4.2.7 Immunoassay procedure for detection of PSA

The monoclonal antibody functionalized-Fe_3O_4@SiO_2-prAmPBA-*anti*-PSA-mAb/glucose (100 µL 100 µg.mL^{-1}) capture bioprobes, were added into 50 µL of spiked serum with different concentrations of PSA and left for 20 mins. Followed by the addition of the polyclonal functionalized fluorescent FITC@SiO_2-prAmPBA-*anti*-PSA-pAb/glucose (100µL, 200 µg.mL^{-1}) sensing nanobioconjugates. The mixture was incubated for 50 min and subjected to gentle shaking at room temperature. A magnet was used to separate the Fe_3O_4@SiO_2-prAmPBA-*anti*-PSA-mAb<PSA>pAb-PSA-*anti*-prAmPBA-SiO_2@FITC immunocomplex from the unreacted reagents. The isolated immunocomplex was washed three times with cold PBST buffer (pH 7.4, 10 mM) and magnet was used for separation. The sandwiched PSA will result in a capture of the fluorescence nanoparticles and magnetically separated. The isolated immunocomplex was re-dispersed in 50 µL of PBS buffer (pH 7.4,10 mM). NaOH (20 µL, 10 mM) was added and incubated at 30°C. After 20 min, the reaction was then subjected to fluorescence measurements with an excitation at 480 nm.

4.3 Results and Discussion

4.3.1 Synthesis of Fe_3O_4@SiO_2-prAmPBA-*anti*-PSA-mAb/glucose

The preparations of nanomagnetic-silica bioprobes was synthesized through several steps. Initially, the synthesis of the stable oleic acid functionalized magnetite (Fe_3O_4NPs) nanoparticles by (a) thermal decomposition of the Fe(oleate)$_3$ precursor to form a wůstite (Fe-O) nanomaterial and (b) the oxidation of Fe-O to form the Fe_3O_4 phase [25,47,48]. Then, a quaternary reverse (W/O) microemulsion system was used to covalently coat the Fe_3O_4NPs with a silica shell to yield nanomagnetic-silica nanoparticles, Fe_3O_4@SiO_2NPs. In this method, the oleic-capped magnetic nanoparticles were coated with the silica shell via a ligand exchange of the oleic ligands and hydrolysis of tetraethyl orthosilicate (TEOS). The hydrolyzed TEOS attached onto the surface of Fe_3O_4NPs which has a strong affinity for oxygen. TEOS hydrolyzed undergoes polycondensation, forming Fe-O-Si bonds and resulting in silica shell [30,49]. The Fe_3O_4@SiO_2NPs were surface functionalized with triethoxysilanepropyl-3-amido phenylboronic acid (TES-prAmPBA) to form phenylboronic acid-functionalized nanomagnetic-silica nanoparticles, Fe_3O_4@SiO_2-prAmPBANPs. The Fe_3O_4@SiO_2-prAmPBANPs were bioconjugated with *anti*-PSA-mAbs and non-specific binding sites blocked with D-glucose to yield Fe_3O_4@SiO_2-prAmPBA-*anti*-PSA-mAb/glucose nanobioprobes. The step-by-step preparations and characterization of the capture bioprobes, Fe_3O_4@SiO_2-prAmPBA-*anti*-PSA-mAb/glucose was studied.

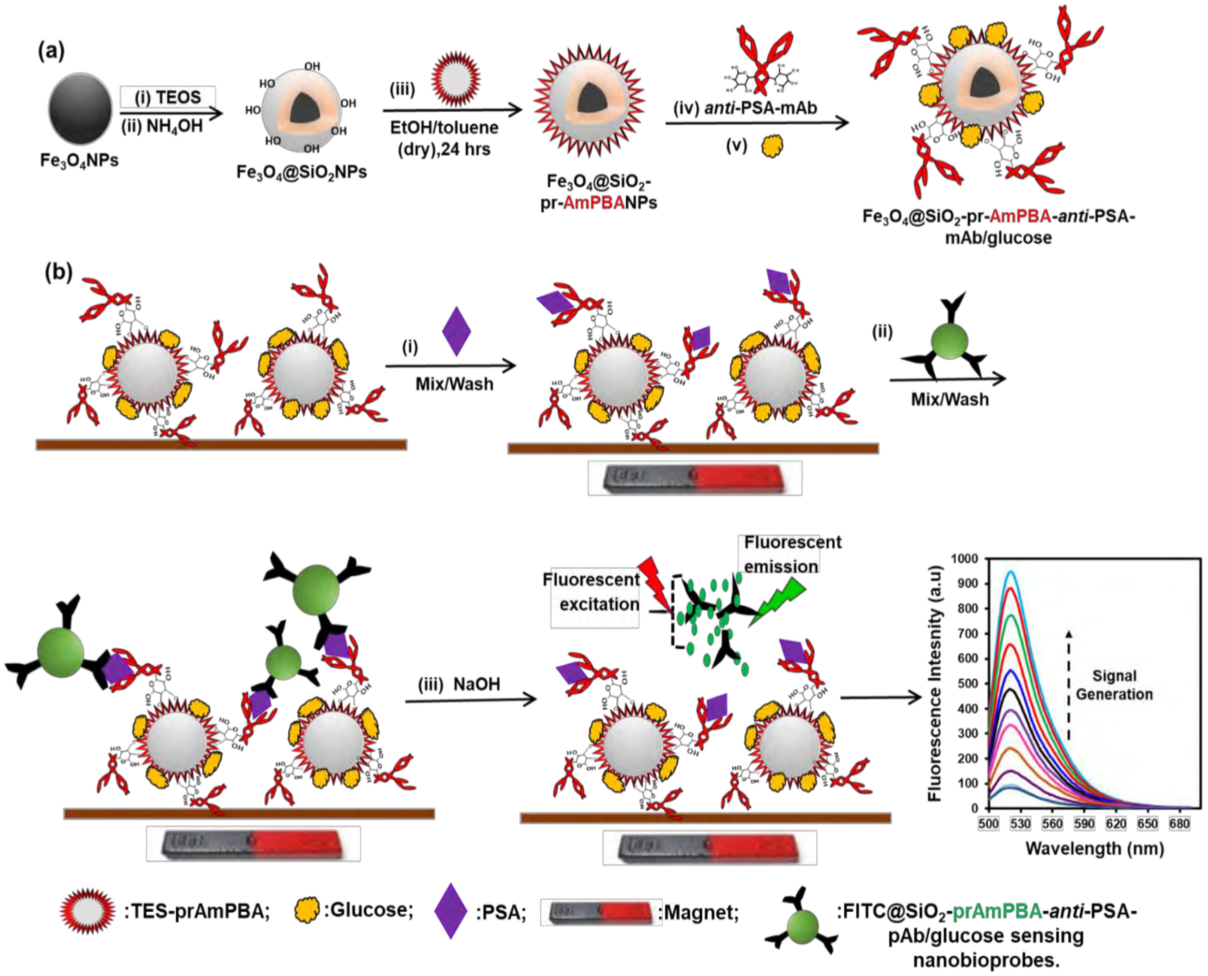

Scheme 4.1: Schematic illustrations of (a) the step-by-step synthesis of the Fe_3O_4@SiO_2-prAmPBA-*anti*-PSA-mAb/glucose capture nanobioprobes. (b) The enhanced fluorescence detection of PSA using Fe_3O_4@SiO_2-prAmPBA-mAb/glucose capture and FITC@SiO_2-prAmPBA-*anti*-PSA-pAb/glucose sensing nanobioconjugates after magnetic separation and dissolution with NaOH (10 mM).

4.3.2 Characterization of Fe_3O_4@SiO_2-prAmPBA-*anti*-PSA-mAb/glucose

4.3.2.1 XRD diffraction characterization

Figure 4.1 shows the XRD diffractograms of (i) Fe_3O_4NPs, (ii) Fe_3O_4@SiO_2NPs, and (iii) Fe_3O_4@SiO_2-prAmPBANPs. The diffractogram in **Fig. 4.1(i)** showed the formation of the Fe_3O_4NPs with peaks at the following 2θ values at 30.6°, 35.8°, 43.8°, 57.7°, and 63.2° which are indicative of a crystalline cubic spinel structure of the magnetite (Fe_3O_4) [30,50,51]. The diffraction patterns show the characteristic of magnetite which were indexed for the following Miller Indices (220), (311), (400), (420), and (440) [36,52]. The diffraction patterns matched well with the Fe_3O_4NPs for the JCPDS-international Centre (JCPDS file NO.19-0629). Similarly, the same peaks are observed for the coated nanomagnetic nanoparticles with silica shell (Fe_3O_4@SiO_2NPs) in **Fig. 4.1(ii)** and functionalization with boronic acid (Fe_3O_4@SiO_2-prAmPBANPs) in **Fig. 4.1(iii)**. A new diffraction peak was observed at $2\theta = 18.1^\circ$ for the amorphous SiO_2. This indicated that Fe_3O_4NPs were stable after the formation of the silica shell and post-surface functionalization with TES-prAmPBA. The crystalline phase of the Fe_3O_4NPs after silica shell coating and surface functionalization remained intact. The average crystal size of Fe_3O_4NPs core, obtained using Debye-Scherrer equation was calculated to be 8.7 nm for Fe_3O_4NPs, 16.5 nm for Fe_3O_4@SiO_2NPs, and 16.9 nm for Fe_3O_4@SiO_2-prAmPBANPs. The increase in particles size was due to the silica shell coating Fe_3O_4NPs core. The functionalization with TES-prAmPBA did not increase the particles size and this is due to a thin monolayer of TES-prAmPBA to form Fe_3O_4@SiO_2-prAmPBANPs. The nanoparticles still retained their magnetic properties. The Fe_3O_4 diffraction peaks were broad after coating with an amorphous silica shell.

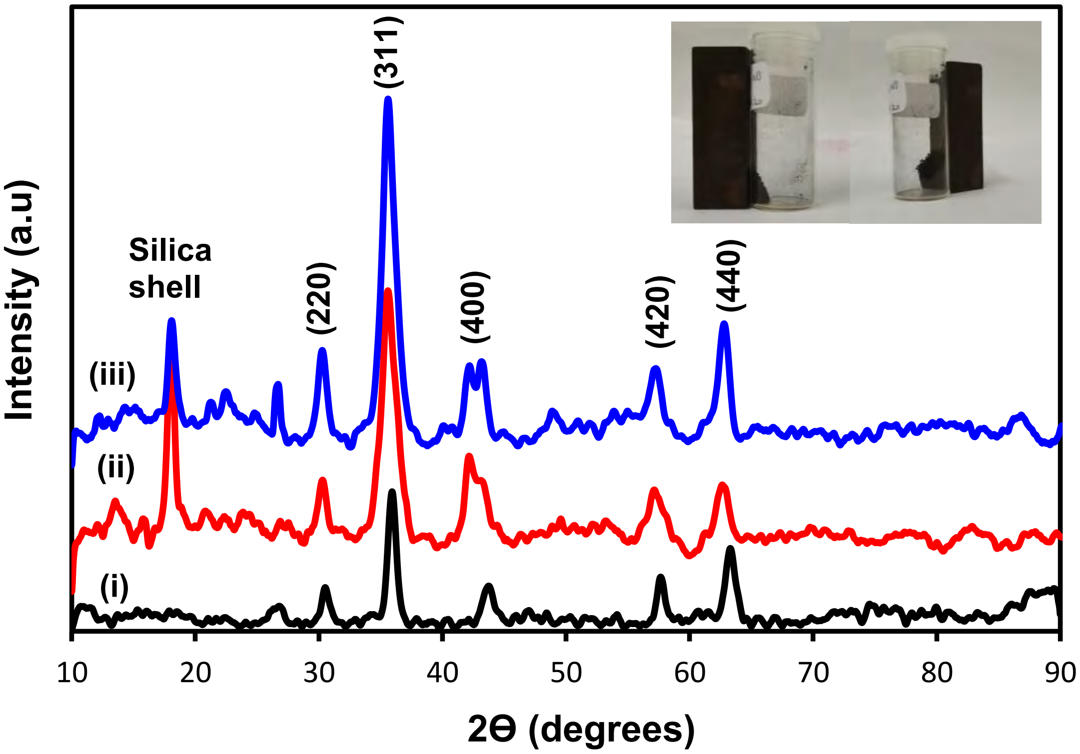

Figure 4.1: XRD diffractograms of (i) Fe_3O_4NPs, (ii) Fe_3O_4@SiO_2NPs, and (iii) Fe_3O4@SiO_2-prAmPBANPs. The insert exhibits the photographs of Fe_3O_4@SiO_2NPs and Fe_3O_4@SiO_2-prAmPBANPs.

4.3.2.2 TEM characterization

The TEM images were used to observe the morphology and size distribution of the nanoparticles to confirm the successful surface coating with silica and surface functionalization with TES-prAmPBA. **Figure 4.2** shows the TEM images and size distribution histograms of (a) Fe_3O_4NPs, (b) Fe_3O_4@SiO_2NPs, and (c) Fe_3O_4@SiO_2-prAmPBANPs. The shape of the nanoparticles is spherical for Fe_3O_4NPs before and after surface coating with SiO_2 shell and TES-prAmPBA. **Figure 4.2(a)** shows that the Fe_3O_4NPs are spherical, monodispersed, and less aggregated. The size distribution was wide with particles size distribution of 10 ± 2 nm. Fe_3O_4NPs were clumping together. **Figure 2(b)** shows the Fe_3O_4@SiO_2NPs which exhibits a core shell structure and agglomeration and clumping of the nanoparticles. The magnetic particles remained even after coating with a silica shell. The reverse water-in-oil (W/O) microemulsion method used induced the surfactant Triton-X-100 surrounded droplets that contained the Fe_3O_4NPs and subsequent coating of silica via hydrolysis of TEOS [51]. From the TEM images, the nanoparticles were agglomerated, but showed that each nanoparticle contained single to multiple magnetite particles in Fe_3O_4@SiO_2NPs. The Fe_3O_4@SiO_2NPs were estimated to have an average diameter of 15 ± 3 nm with a narrow size distribution. A 5 nm size increase is observed from Fe_3O_4NPs to Fe_3O_4@SiO_2NPs, which can be attributed to the silica shell formation. **Figure 4.2(c)**, the Fe_3O_4@SiO_2-prAmPBANPs showed an estimated average particle size and narrow distribution of 21 ± 3 nm. The increase in the particle size diameter was due to the introduction of TES-prAmPBA onto the silica surface. Therefore, the successive increase in particles size diameter and at each stage of functionalization of the nanoparticles indicated the successful coating with silica and TES-prAmPBA.

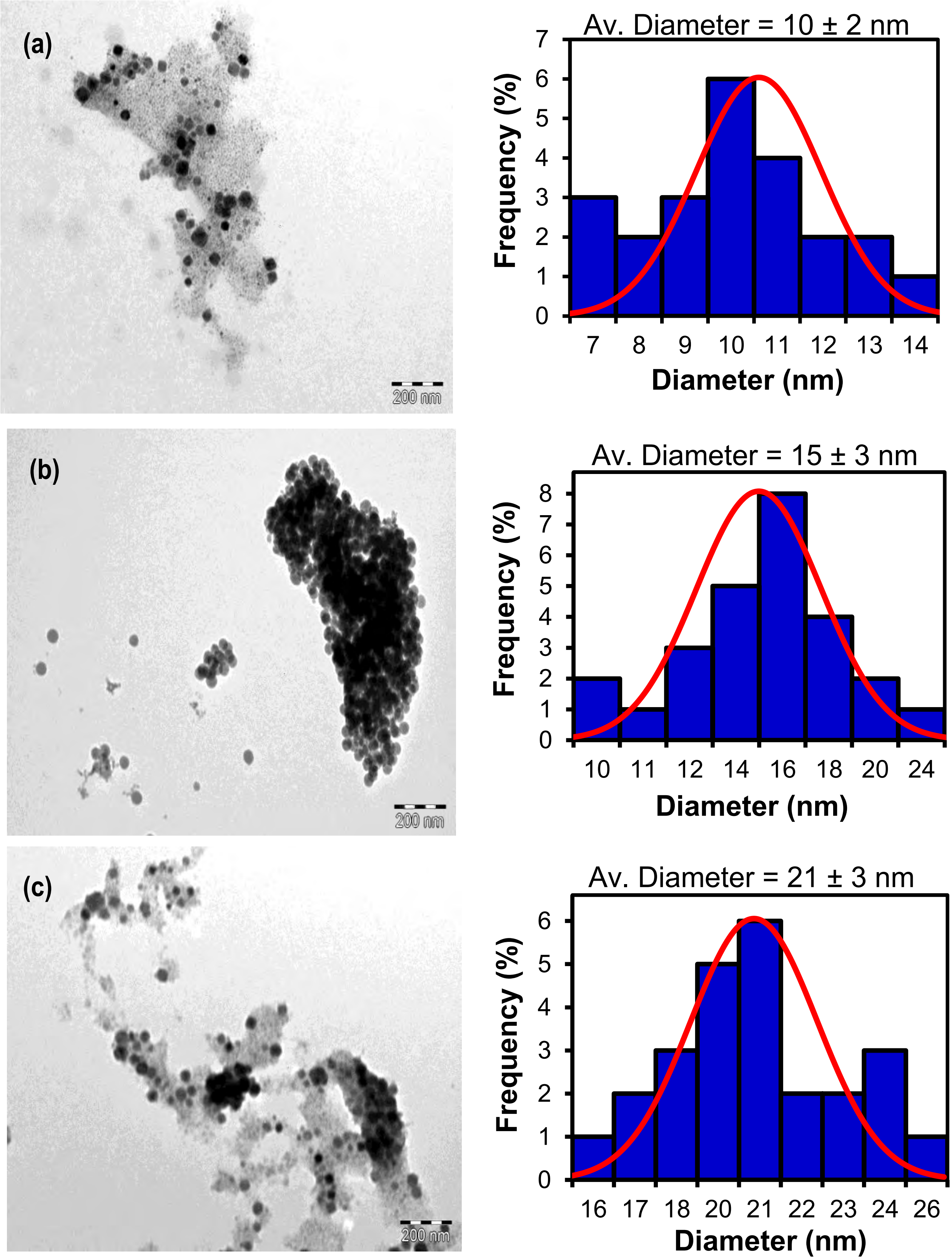

Figure 4.2: TEM images of (a) Fe_3O_4NPs, (b) Fe_3O_4@SiO_2NPs, (c) Fe_3O_4@SiO_2-prAmPBANPs.

4.3.2.3 EDS-SEM characterization

The characterization of the as-prepared magnetic nanoparticles was further performed by EDS-SEM, FT-IR analyses, and zeta-potential measurements. The energy dispersive X-ray spectroscopy (EDS) spectra were used for quantitative elemental composition analysis of the magnetic nanoparticles at different functionalization steps. **Figure 4.3** shows the EDS spectra with corresponding SEM images of (a) Fe_3O_4NPs, (b) Fe_3O_4@SiO_2NPs, and (c) Fe_3O_4@SiO_2-prAmPBANPs. EDS spectrum of Fe_3O_4NPs in **Fig. 4.3(a)** showed the presence of Fe K (33.9%), O K (27.8%), and C K (38.3.0%) confirming the presence of carbon (C K), iron (Fe K), and oxygen (O K) which was attributed to iron oxide nanoparticles capped with oleic acid. The carbon (C K) was from the oleic acid (C-H) chains used in their preparations as a stabilizer for the nanoparticles.

Figure 4.3(b) shows the EDS spectrum of Fe_3O_4@SiO_2NPs. The presence of the Si K peak confirmed the formation of the silica shell. The disappearance of the carbon (C K) peaks is due to the treatment of the magnetic nanoparticles with tetraethyl orthosilicate (TEOS) which form siloxane (Si-O-Si) and silanol (Si-OH) functional groups. The elemental composition was Fe K (29.5%), O K (50.4%), and Si K (20.1%). The increase in O K from 27.8% to 50.4% is due to SiO_2 shell, and the Fe K decrease from 33.9% to 29.5% further confirming the formation of the silica (SiO_2) shell. The presence of Si K and increased O peaks confirms the successful silica coating of magnetic nanoparticles. After surface functionalization with TES-prAmPBA to yield Fe_3O_4@SiO_2-prAmPBANPs, the appearance of the boron (B K) peak was observed in **Fig. 4.3(c)**.

Further, the presence of the N K peak is due to the amide bond from TES-PrAmPBA. Similarly, the C K peaks are due to the TES-prAmPBA. Therefore, with the appearance of the iron (Fe K), oxygen (O K), silica (Si K), boron (B K), carbon (C K), and nitrogen (N K) peaks confirmed the successful surface formation of Fe_3O_4@SiO_2-prAmPBANPs. The monitored steps confirmed the successful synthesis of the magnetic nanoparticles and their functionalization with phenylboronic acid.

The corresponding scanning electron microscopy (SEM) images to the EDS spectra confirmed the synthesis of Fe_3O_4NPs and the different functionalization steps. The SEM images showed a variation and changes in surface roughness from the Fe_3O_4NPs to Fe_3O_4@SiO_2NPs, and to Fe_3O_4@SiO_2-prAmPBANPs. The change in the surface roughness with the support of the EDS analysis confirmed the successful modification and functionalization of Fe_3O_4NPs to Fe_3O_4@SiO_2-prAmPBANPs. Further, the SEM images showed the inhomogeneity in the nanomagnetic nanoparticles size distribution.

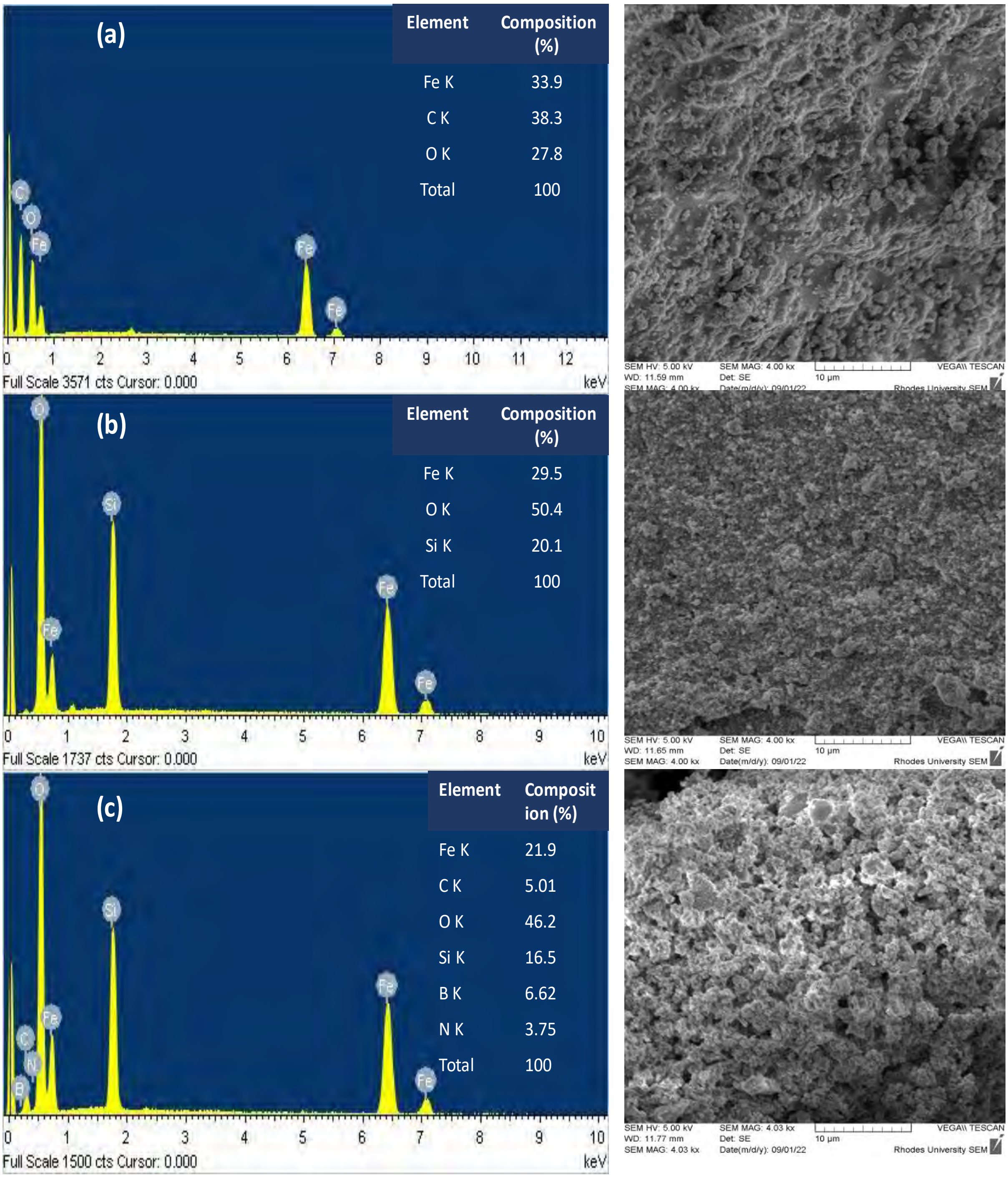

(a)

Element	Composition (%)
Fe K	33.9
C K	38.3
O K	27.8
Total	100

(b)

Element	Composition (%)
Fe K	29.5
O K	50.4
Si K	20.1
Total	100

(c)

Element	Composition (%)
Fe K	21.9
C K	5.01
O K	46.2
Si K	16.5
B K	6.62
N K	3.75
Total	100

Figure 4.3: EDS plots with corresponding SEM images for (a) Fe_3O_4NPs, (b) $Fe_3O_4@SiO_2$NPs, and (c) $Fe_3O_4@SiO_2$-prAmPBANPs.

4.3.2.4 FT-IR analysis

The FT-IR was used to confirm the successful synthesis of the magnetic nanoparticles, the surface functionalization and bioconjugation with *anti*-PSA-mAb. **Figure 4.4** shows the FT-IR spectra of (a) (i) Fe_3O_4NPs, (ii) Fe_3O_4@SiO_2NPs, (iii) Fe_3O_4@SiO_2-prAmPBANPs, and (b) Fe_3O_4@SiO_2-prAmPBA-*anti*-PSA-mAb. The FT-IR spectrum of Fe_3O_4NPs in **Fig. 4.4(a)(i)** shows the aliphatic (C-H) asymmetric and symmetric stretching bands at 2918 cm^{-1} and 2849 cm^{-1}. The peaks at 1545 cm^{-1} and 1409 cm^{-1} are attributed to asymmetric and symmetric ($-COO^-$) stretching vibrations, due to the carboxylates with Fe ions of Fe_3O_4NPs. The interactions of oleic acid (OA) as a capping agent being chemically bound to the magnetite Fe_3O_4NPs. An intense (Fe-O) peak is also observed at 562 cm^{-1} and confirming the successful synthesis and coating of Fe_3O_4NPs with oleic acid. Then, the coating with SiO_2 to OA-capped Fe_3O_4NPs to form Fe_3O_4@SiO_2NPs. This is to enable the stability of the nanoparticles. After the formation of the silica shell the peaks at 1710 cm^{-1}, 1545 cm^{-1}, and 1409 cm^{-1} disappeared in **Fig. 4.4(a)(ii)**. This was due to the ligand exchange between TEOS and oleic acid ligands to yield Fe_3O_4@SiO_2 core shell nanoparticles. Additionally, a broad (O-H) peak is observed at 3285 cm^{-1}. Other peaks at 1046 cm^{-1}, 940 cm^{-1}, and 797 cm^{-1} appeared due to the asymmetric stretching vibration bands of siloxane (Si-O-Si), (Si-O) group, and silanol (Si-OH) groups, respectively. A decrease in the (Fe-O) peak is observed at 562 cm^{-1}. This reflected the successful synthesis of the Fe_3O_4@SiO_2NPs.

Surface functionalization of the magnetic-silica nanoparticles was achieved using TES-prAmPBA using covalent attachment via siloxane bond formation. **Figure**

4.4(a)(iii) shows the Fe_3O_4@SiO_2-prAmPBANPs spectrum which exhibits an (N-H) stretching peak at 3872 cm^{-1} corresponding to the (N-H) bending at 1540 cm^{-1} of the amide bond of TES-prAmPBA. The (C=O) absorption peak is observed at 1649 cm^{-1} and the emergence of the absorption peak of the (B-O) vibrational stretch at 1386 cm^{-1}. These indicate the successful surface modification of Fe_3O_4@SiO_2NPs with TES-prAmPBA onto the silica layer. The Fe_3O_4@SiO_2-prAmPBANPs were later reacted with *anti*-PSA-mAb to form Fe_3O_4@SiO_2-prAmPBA-*anti*-PSA-mAb.

The bioconjugation of the antibody was achieved through cyclic boronate ester bonds between the cis-diol of the glycan moieties on the Fc region of the antibody, to the (-OH) groups on the phenyboronic acid. The boronic acid bioconjugation method helps maintain the orientation of the antibody for enhanced antigen binding. **Figure 4.4(b)** shows the FT-IR spectrum of Fe_3O_4@SiO_2-prAmPBA-*anti*-PSA-mAb and the appearance of an intense stretching vibration of the (amide I) and (amide II) cyclic ester bonds of the *anti*-PSA antibody at 1639 cm^{-1} and 1546 cm^{-1} is observed. The absorption peak at 3355 cm^{-1} is assigned to the presence of the NH_2 from the antibody. The shift of B-O peak from 1386 cm^{-1} to 1390 cm^{-1} of the boronic acid confirmed the successful bioconjugation of the antibody to the phenylboronic acid. This confirms the successful preparation of Fe_3O_4@SiO_2-prAmPBA-*anti*-PSA-mAb bioprobes.

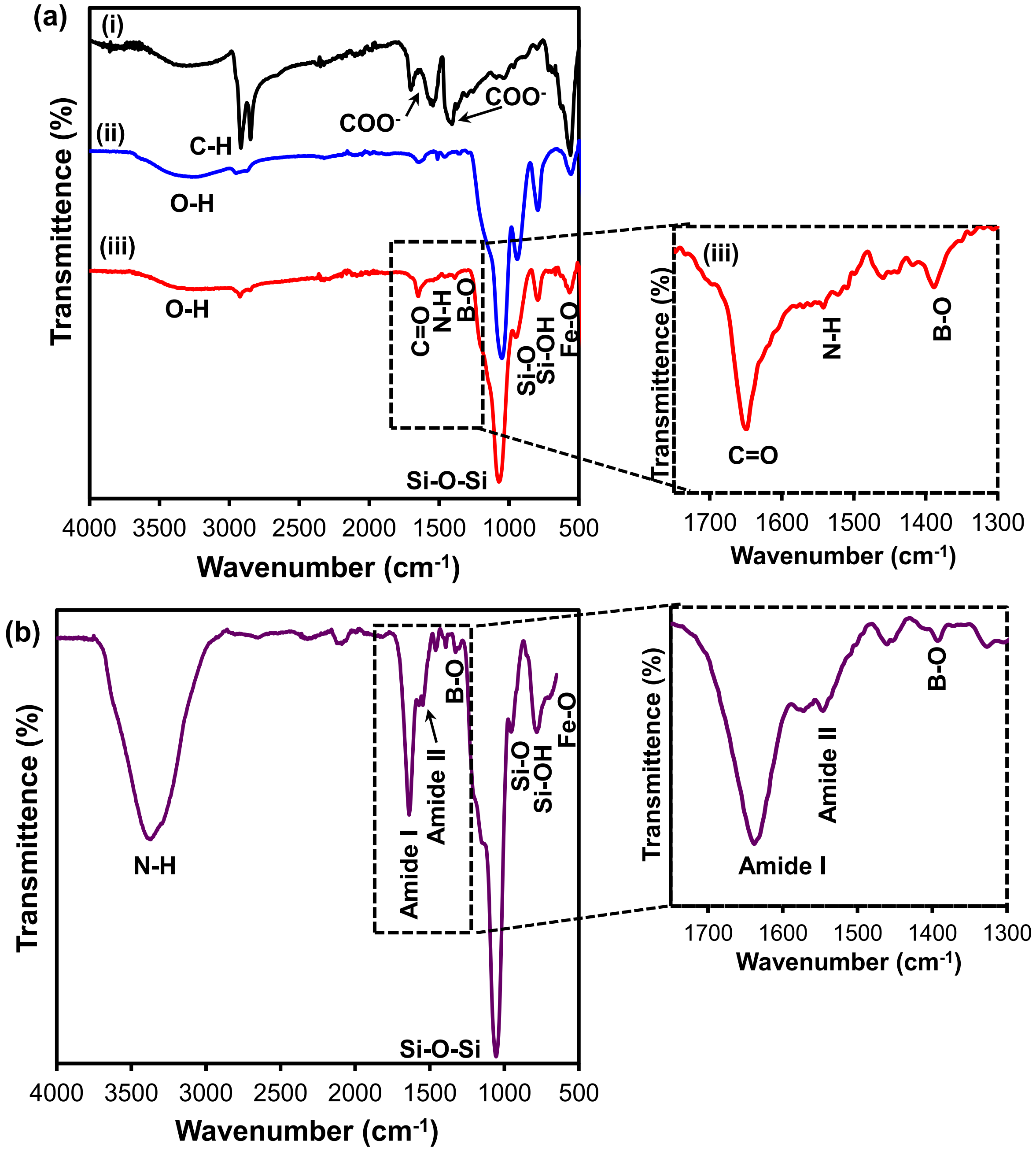

Figure 4.4: FT-IR spectra of (a) (i) Fe_3O_4NPs, (ii) Fe_3O_4@SiO_2NPs, (iii) Fe_3O_4@SiO_2-prAmPBANPs, and (b) Fe_3O_4@SiO_2-prAmPBA-*anti*-PSA-mAb.

4.3.3 Effects of pH on nanoparticles surface charge

The zeta potential measurements were carried out to further confirm the functionalization and stability of the magnetic nanoparticles in changing pH conditions. **Figure 4.5** shows the zeta potential (mV) plot obtained at varied pH values from pH 2.0 to pH 10 in 10 mM PBS for (i) Fe_3O_4NPs, (ii) $Fe_3O_4@SiO_2$NPs, (iii) $Fe_3O_4@SiO_2$-prAmPNANPs, and (iv) $Fe_3O_4@SiO_2$-prAmPBA-*anti*-PSA-mAb. **Figure 4.5(i)** for the Fe_3O_4NPs shows a decrease in the zeta potential values up to -30 mV as the pH values increase. The decrease in zeta potential value is due to the deprotonation of the surface hydroxyl (OH) leading to a negative zeta potential surface charge. The zeta potential was -23.8 mV at pH 7.0. After coating with silica shell in **Fig. 4.5(ii)**, the zeta potential values started at +20 mV for $Fe_3O_4@SiO_2$NPs. As the pH increased the zeta potential was negative and increased negatively up to -43.2 mV at pH 10. The isoelectric point (IEP) was observed at pH 2.3. At pH 7.0 a zeta potential was -32.2 mV. The negative increase in the zeta potential was due to the deprotonation of the (OH) groups from the silica shell and confirming the presence of the silanol (Si-OH) groups. After the surface functionalization with TES-prAmPBA, in **Fig. 4.5(iii)** shows a decrease in the zeta potential charges from +24.0 mV at pH 3 to –40.0 mV at pH 10. The isoelectric point was observed at pH 5.2. The zeta potential charge was due to the deprotonation of the (B-OH) hydroxyl groups from TES-prAmPBA with a zeta potential of -30.0 mV at pH 7.0. **Figure 4.5(iv)** shows pH effect on $Fe_3O_4@SiO_2$-prAmPBA-*anti*-PSA-mAb and a decrease from +25.0 mV at pH 2.0 to -23 mV at pH 10. An isoelectric point is found at pH 6.4 and the zeta-potential of -3.7 mV is observed at pH 7.0. This can be related to the protein functional groups from the antibody. The observed changes in surface due to pH changes confirm the successful bioconjugation of the *anti*-PSA-mAb to yield Fe_3O_4@SiO_2-prAmPBA-*anti*-PSA-mAb capture probes.

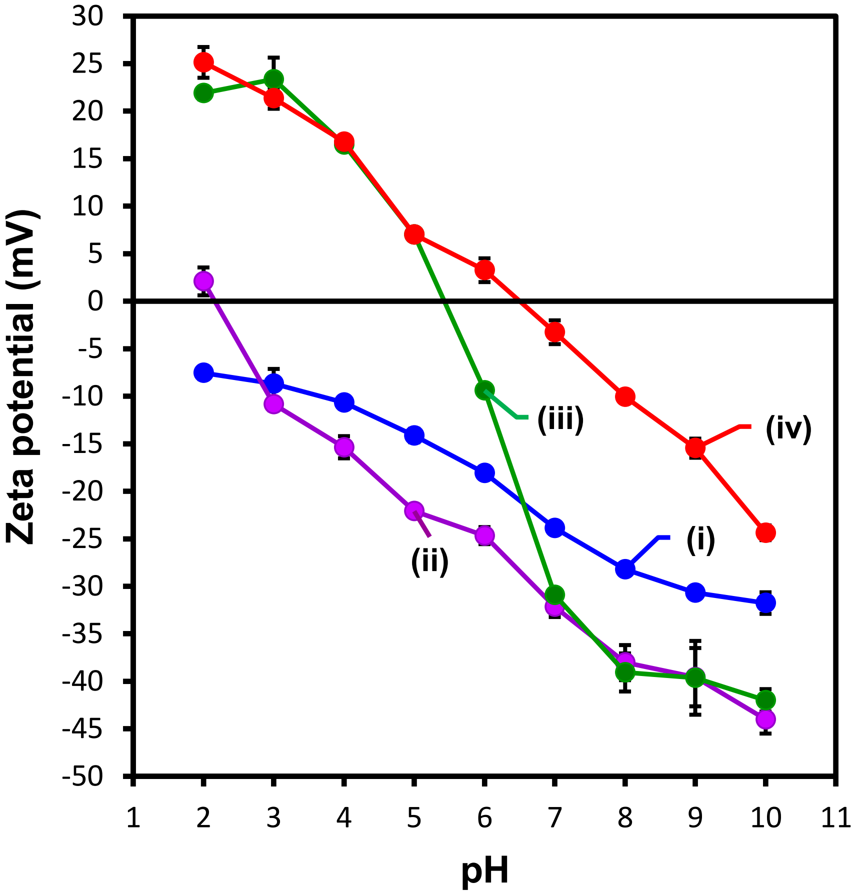

Figure 4.5: Zeta potential (mV) vs pH (2-10, PBS, 10 mM) for (i) Fe_3O_4NPs, (ii) Fe_3O_4@SiO_2NPs, (iii) Fe_3O_4@SiO_2-prAmPBANPs, and (iv) Fe_3O_4@SiO_2-prAmPBA-*anti*-PSA-mAb.

4.3.4 Bioconjugation with *anti*-PSA-mAb onto Fe_3O_4@SiO_2-prAmPBANPs

UV-Vis spectra and the Bradford assay were used to confirm the immobilization of *anti*-PSA-mAb onto Fe_3O_4@SiO_2-prAmPBANPs and for protein quantification. The calibration curve at different BSA concentrations was used to quantify the protein solution before and after conjugation. The UV-Vis absorbance measurements were obtained at 595 nm and the protein (*anti*-PSA-mAb) concentration before was measured. The protein amount bioconjugated onto Fe_3O_4@SiO_2-prAmPBANPs to form Fe_3O_4@SiO_2-prAmPBA-*anti*-PSA-mAb was calculated by subtracting the determined concentration of the supernatant from the initial concentration solution of *anti*-PSA-mAb. After bioconjugation the percentage of the conjugation efficiency (%CE) was calculated using **Equation (3.2)**. The %CE was found to be 71.9% corresponding to the amount of protein conjugated to form Fe_3O_4@SiO_2-prAmPBA-*anti*-PSA-mAb capture bioprobes. Therefore, this study and the Bradford assay **Fig. 4.6** below confirmed the successful preparations of Fe_3O_4@SiO_2-prAmPBA-*anti*-PSA-mAb used as capture bioprobes for PSA. The magnetic separation allowed for only bioconjugated *anti*-PSA-mAb to be obtained. Non-specific boronic acid binding sites were blocked with D-glucose solution to yield Fe_3O_4@SiO_2-prAmPBA-*anti*-PSA-mAb/glucose capture bioprobes.

4.3.5 Bradford Assay *anti*-PSA-mAb onto Fe_3O_4@SiO_2-prAmPBANPs

The Bradford assay was used to determine the protein quantification of *anti*-PSA monoclonal antibodies (*anti*-PSA-mAbs) onto Fe_3O_4@SiO_2-prAmPBANPs. UV-Vis measurements were obtained at 595 nm which corresponded to the BSA standard solutions and protein (*anti*-PSA-mAb) in solution as shown in **Fig. 4.6(a)**. The calibration curve of known BSA concentrations as shown in **Fig. 4.6(b)** was used to extrapolate and determine the concentrations of the *anti*-PSA-mAb in the supernatant solution. The absorbance of the used volumes of the BSA standard solutions and protein suspension were recorded in triplicates. Mean values were determined and found to range from 0.23 to 0.32 ± 0.09 a.u with very low standard deviations. The mean value of the unknown concentration of the *anti*-PSA-mAbs suspension was 0.25 ± 0.02 a.u and recorded as a representative value of the absorbance of *anti*-PSA-mAbs. Then, this value was fitted into the calibration curve, along with the BSA standard solutions mean values, and used to calculate the concentration of the unknown protein x (*anti*-PSA-mAbs) after bioconjugation with $Fe_3O_4@SiO_2$-pr-AmPBANPs. The linear equation used was (ΔAbs = 0.007 [*anti*-PSA-mAb] + 0.214) with R^2=0.997 was used to determine the concentration of the unknown protein x (*anti*-PSA-mAbs) and which was found to be 4.49 µg.mL^{-1}.

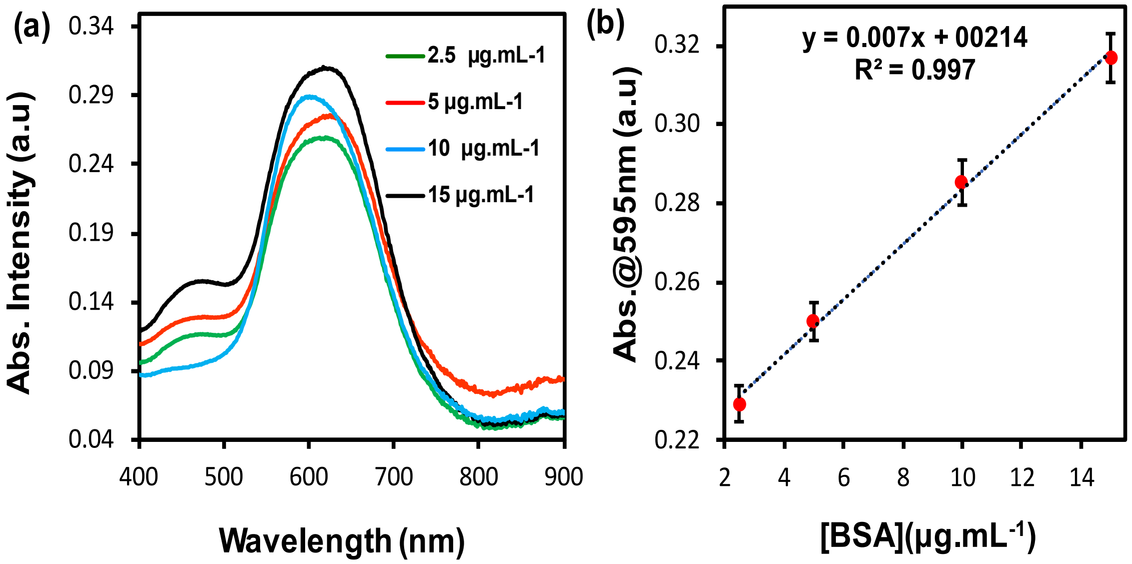

Figure 4.6: (a) UV-Vis spectrum of different BSA standards (2.5 - 15 µg.mL^{-1}) and (b) the corresponding calibration curve of different BSA standards (n = 3).

4.4 Evaluating the immunosensor reaction

In the proposed immunosensor, $Fe_3O_4@SiO_2$-prAmPBA-*anti*-PSA-mAb/glucose bioprobes are used to capture PSA from the sample solution as the first immunoreaction. Then, FITC@SiO$_2$-prAmPBA-*anti*-PSA-pAb/glucose nanobioconjugates were added to recognize the captured PSA by the second immunoreaction, forming sandwich immunocomplexes of Fe$_3$O$_4$@SiO$_2$-prAmPBA-*anti*-PSA-mAb<PSA>pAb-PSA-*anti*-prAmPBA@SiO$_2$@FITC. **Figure 4.7** shows the fluorescence emission spectra of the nanomagnetic capture nanoparticles for (a) Fe$_3$O$_4$NPs, (b) Fe$_3$O$_4$@SiO$_2$NPs, (c) Fe$_3$O$_4$@SiO$_2$-prAmPBANPs, and (d) Fe$_3$O$_4$@SiO$_2$-prAmPBA-*anti*-PSA-mAb>PSA. In **Fig. 4.7(a)-(d),** no fluorescence emission intensity was observed. Only in the presence of FITC@SiO$_2$-prAmPBA-*anti*-PSA-pAb/glucose, PSA, and Fe$_3$O$_4$@SiO$_2$-prAmPBA-*anti*-PSA-mAb sandwich immunoassay we observed a fluorescence signal. The immunoassay resulted (i) in the capture of PSA by Fe$_3$O$_4$@SiO$_2$-prAmPBA-*anti*-PSA-mAb/glucose, (ii) magnetically separated, (iii) detection using FITC@SiO$_2$-prAmPBA-*anti*-PSA-pAb/glucose, (iv) magnetically separated, and (v) the fluorescence signal was generated by adding NaOH (20 µL, 10 mM), and after 20 mins the sandwich-like immunocomplex nanobioprobes were subjected to fluorescence measurements. **Figure 4.7(e)** shows the fluorescence emission of the sandwich immunoassay, Fe$_3$O$_4$@SiO$_2$-prAmPBA-*anti*-PSA-mAb<PSA>pAb-PSA-*anti*-prAmPBA@SiO$_2$@FITC nanobioprobes at 518 nm. The emission spectrum is similar to **Fig. S4.1(b)** for FITC @SiO$_2$-prAmPBA-*anti*-PSA-pAb/glucose nanobioconjugates. Therefore, indicating the successful capture of PSA by Fe$_3$O$_4$@SiO$_2$-prAmPBA-*anti*-PSA-mAb/glucose and detection using the fluorescence nanoparticles, FITC@SiO$_2$-prAmPBA-*anti*-PSA-pAb/glucose as sandwich immunoassay.

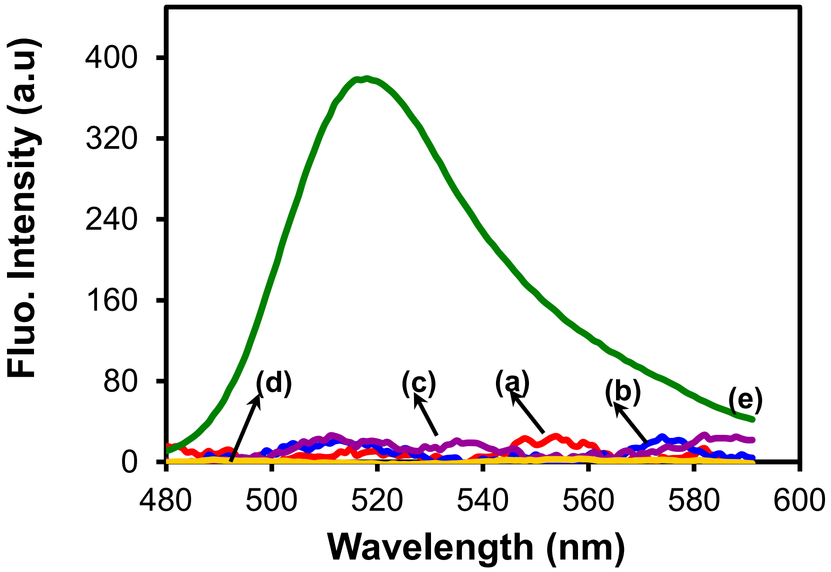

Figure 4.7: Fluorescence spectra of (a) Fe_3O_4NPs, (b) Fe_3O_4@SiO_2NPs, (c) Fe_3O_4@SiO_2-prAmPBANPs, (d) Fe_3O_4@SiO_2-prAmPBA-*anti*-PSA-mAb<PSA, and (e) Fe_3O_4@SiO_2-prAmPBA-*anti*-PSA-mAb<PSA>pAb-PSA-*anti*-prAmPBA-SiO_2@FITC nanobioprobes.

4.4.1 Optimization of the detection conditions

The concentration of the Fe_3O_4@SiO_2-prAmPBA-*anti*-PSA-mAb/glucose capture bioprobes and FITC@SiO_2-prAmPBA-*anti*-PSA-pAb/glucose sensing nanobioconjugates along with the effect of the incubation time of the PSA capture were optimized. Both the concentration and incubation time parameters affect the sensitivity of the immunobiosensor. **Figure 4.8** shows the fluorescence spectra of the obtained Fe_3O_4@SiO_2-prAmPBA-*anti*-PSA-mAb<PSA>pAb-PSA-*anti*-prAmPBA-SiO_2@FITC nanobioprobes at (a) the different concentrations of the Fe_3O_4@SiO_2-prAmPBA-*anti*-PSA-mAb/glucose and (b) the effects of the incubation time on the response of the immunobiosensor for the detection of PSA. The concentration of PSA was 50 ng.mL^{-1}

and FITC@SiO_2-prAmPBA-*anti*-PSA-pAb/glucose was 20 µg.mL^{-1}. From **Fig. 4.8(a)** the fluorescence emission intensity increased with increasing amounts of Fe_3O_4@SiO_2-prAmPBA-*anti*-PSA-mAb/glucose up to 10 µg.mL^{-1}. Similarly, **Fig. 4.8(b)** the fluorescence emission intensity increased with the increasing incubation time with a fluorescence maximum at 50 mins. The optimum incubation time for FITC@SiO_2-prAmPBA-*anti*-PSA-pAb/glucose in NaOH (10 mM) was 20 mins at 37°C.

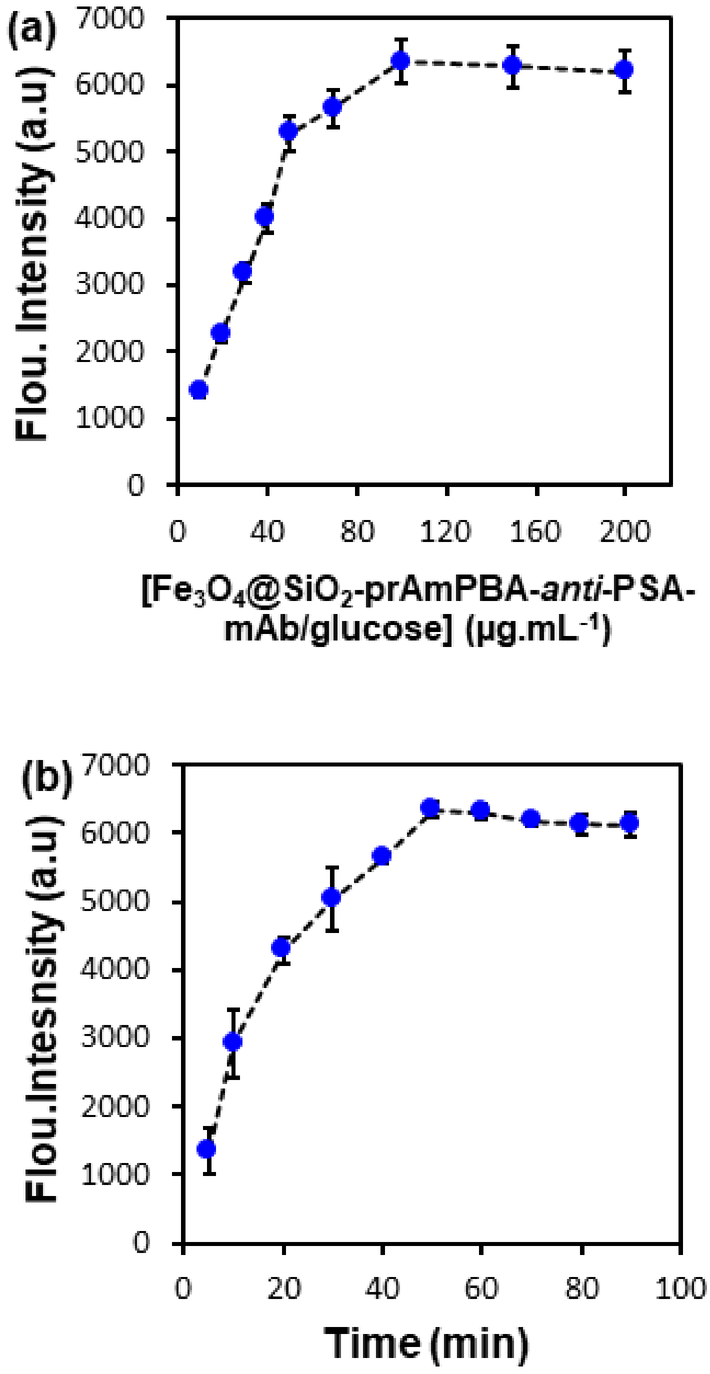

Figure 4.8: Effect of (a) Fe_3O_4@SiO_2-prAmPBA-*anti*-PSA-mAb/glucose concentration on the fluorescence signal and (b) incubation time of the Fe_3O_4@SiO_2-prAmPBA-*anti*-PSA-mAb/glucose<PSA>glucose/pAb-PSA-*anti*-prAmPBA-SiO_2@FITC on the response of the immunobiosensor of PSA (n=3).

4.4.2 Detection of PSA

Using the proposed fluorescence immunobiosensor, PSA was detected using fluorescence measurements. The dissolution fluorescence-linked immunosorbent assay (FLISA) method was employed for the detection of PSA. After the addition of NaOH, the FITC molecules are released from the silica shell into solution and increasing the fluorescence detection. The Fe_3O_4@SiO_2-prAmPBA-*anti*-PSA-mAb/glucose capture and FITC@SiO_2-prAmPBA-*anti*-PSA-pAb/glucose sensing nanobioprobes were incubated for 50 mins to form the Fe_3O_4@SiO_2-prAmPBA-*anti*-PSA-mAb<PSA>pAb-PSA-*anti*-prAmPBA-SiO_2@FITC immunocomplexes. After 50 min the sandwich assay was separated magnetically and washed with PBS (10 mM, 7.4). NaOH (20 µL, 10 mM) solution was added. After 20 mins the solution of the immunocomplex nanobioprobes were subjected to fluorescence measurements at an excitation of 480 nm. **Figure 4.9(a)** shows an increasing fluorescence intensity at increasing PSA concentrations from 2.0 pg.mL^{-1} - 100 ng.mL^{-1}. **Figure 4.9(b)** shows the PSA dose-response curve, which shows the correlation of the fluorescence intensity with an increase in the PSA concentrations. **Figure 4.9(c)** shows the calibration curve of the proposed fluorescence immunosensor, the changes in fluorescent intensity ($\Delta FI_{max} = FI_i - FI_o$) vs the log of PSA concentration. The linear relationship was obtained over the studied concentration range up to 100 ng.mL^{-1}. A linear regression equation with a regression coefficient (R^2) of 0.995 is **Equation (4.1)**:

$$\Delta FI_{max} = 1094.2 \log [PSA] + 1315.3 \qquad \textbf{(4.1)}$$

A detection limit (LOD) of 0.81 pg.mL^{-1} and limit of quantification (LOQ) of 2.46 pg.mL^{-1} were achieved. The results suggested the fluorescence immunosensor can be used for sensitive detection of ultra-low concentrations of PSA in pg.mL^{-1} range and up to ng.mL^{-1}.

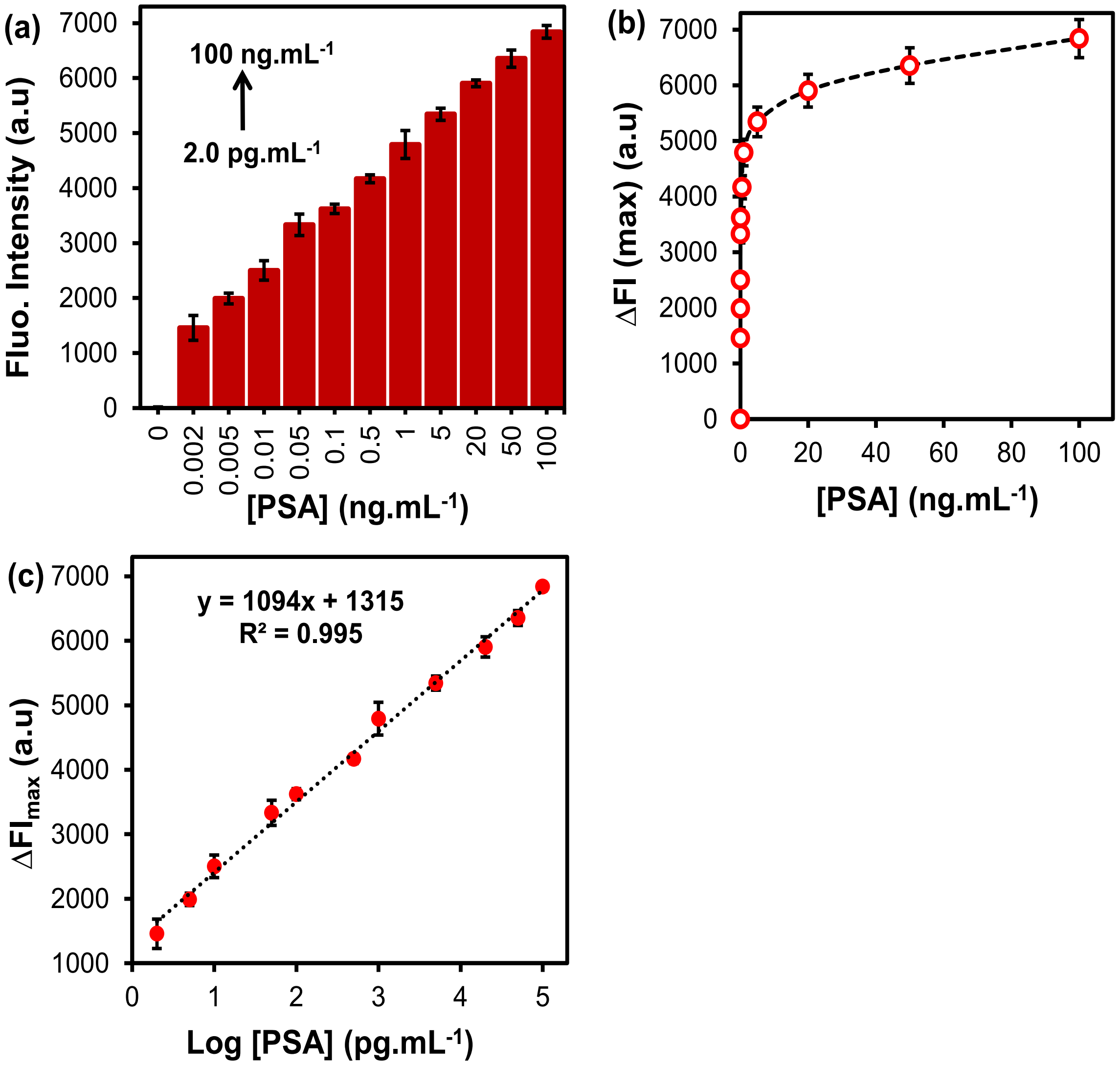

Figure 4.9: (a) Bar graph for fluorescence emission signal for different concentrations of PSA ranging from 2.0 pg.mL^{-1} to 100 ng.mL^{-1}, (b) dose-response curve of relative fluorescence intensity ($\Delta FI_{max} = FI_i - FI_o$), and (c) linear relation of relative fluorescence intensity (ΔFI_{max}) against PSA concentrations.

The applicability of the fluorescence immunobiosensor was conducted in PSA spiked newborn calf serum (NCS) samples. The average values of the recovery and the coefficient of the variation (CV) results are summarized in **Table 4.1**. Excellent % recovery values in the ranges of 94.8% to 103.0% were obtained, with low coefficient of variation (%CV) from 1.2% to 6.8%. These results show reliability of the fluorescence immunosensor for PSA detection.

Table 4.1: Intra-assay % recovery for the detection of PSA in the spiked serum samples.

Added (ng. mL^{-1})	Inter-assay of PSA (ng. mL^{-1})				Average recovered	CV (%)	Recovery (%)
	1	2	3	4			
0.5	0.49	0.53	0.48	0.45	0.49	6.78	97.5
1	0.96	0.98	0.98	0.87	0.95	1.22	94.8
5	5.3	4.8	5.2	5.3	5.15	4.62	102.5

4.5 Specificity and selectivity of the immunosensor

The specificity and selectivity of the proposed immunosensor was investigated by determining the assay responses to PSA and other interfering analytes. Further, the immunosensor was verified by applying the immunosensor in serum samples spiked with BSA, IgG antibody solutions and the mixture of IgG and PSA as shown in **Fig. 4.10**. The corresponding fluorescence responses of the immunosensor are after removing the background interferences. The specificity and selectivity studies of the fluorescence immunosensor in the presence of PSA and other analytes like BSA and IgG, mixture of IgG and PSA. From **Fig. 4.10**, the BSA and IgG antibody samples shows very weak fluorescence responses. The PSA spiked serum samples and IgG/PSA mixture gave high fluorescence intensity response. The immunosensor demonstrated excellent specificity and selectivity towards PSA detection.

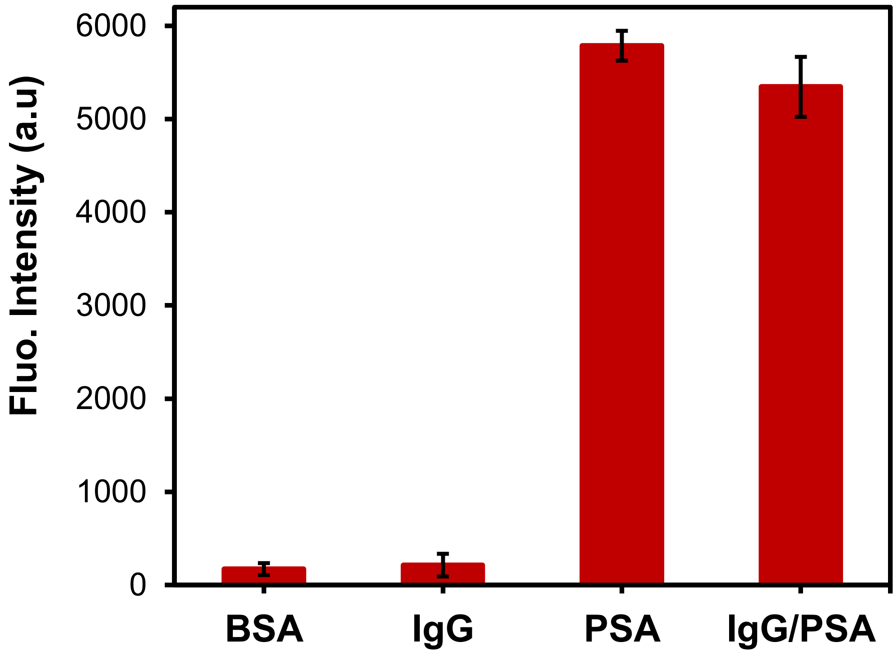

Figure 4.10: The specificty studies of the fluorescent immunoassay sensor in the presences of PSA and other antibodies. (n = 3).

Furthermore, the comparison of the study was done with previously reported methods of detection for PSA as summarized in **Table 4.2**. The LOD of the study was found to be 0.81 pg.mL^{-1} with an LOQ of 2.46 pg.mL^{-1}. As compared to other previously reported methods of PSA detection with LODs of 10 pg.mL^{-1} [2], 3.0 pg.mL^{-1} [19], 83 pg.mL^{-1} [53], 27 pg.mL^{-1} [54], 30 pg.mL^{-1} [55], and which employed the use of detection probes such as Mutli-CAT-AuNPs-Ab$_2$, HRP-Ab$_2$-SiO$_2$NSs, CdTe@SiO$_2$-Ab$_2$, Ag/SiO$_2$@RuBpy@SiO$_2$-Ab$_2$, and rGO-Ca:CdSe-Ab$_2$, respectively. In this work, the proposed FLISA biosensor gave a lower LOD of 1.07 pg.mL^{-1} for PSA detection. The proposed FLISA in this study offered the advantage due to the use of nanomagnetic-silica capture bioprobes for PSA concentration enrichment in the serum matrix and the highly fluorescent FITC-doped silica sensing nanoconjugates, in which the amplification of fluorescence signals was observed upon dissolution of the silica nanoparticles.

Table 4.2: A comparison of different analytical biosensors' performance for the detection of PSA.

Detection Probe	**Capture substrate**	**Signal Monitored**	**Linear concentration range (LCR)**	**LOD**	**Ref.**
FITC@SiO$_2$-prAmPBA-*anti*-PSA-pAb\glucose	Fe$_3$O$_4$@SiO$_2$-*anti*-PSA-mAb/glucose	Fluorescence (serum)	2.0 pg.mL^{-1} – 100 ng.mL^{-1}	0.81 pg.mL^{-1}	[TW]
	well/*anti*-PSA-mAb/BSA	Fluorescence (buffer)	2.0 pg.mL^{-1} - 50 ng. mL^{-1}	0.70 pg.mL^{-1}	[TW]
	well/*anti*-PSA-mAb/BSA	Fluorescence (serum)	2.0 pg.mL^{-1} - 100 ng.mL^{-1}	1.07 pg.mL^{-1}	[TW]
HRP-Ab$_2$-SiO$_2$NSs	well/Ab$_1$/BSA	Fluorescence	30 pg.mL^{-1} - 100 ng. mL^{-1}	10 pg. mL^{-1}	[2]
CdTe@SiO$_2$-Ab$_2$	Fe$_3$O$_4$-Ab$_1$	Fluorescence	10 pg.mL^{-1} – 5.0 ng.mL^{-1}	3.0 pg.mL^{-1}	[19]
HRP-*anti*-PSA-IgG	well-anti-PSA-mIgY	Fluorescence	0.10 ng.mL^{-1} - 3.38 ng.mL^{-1}	83 pg.mL^{-1}	[50]
Ag/SiO$_2$@RuBpy@SiO$_2$-Ab$_2$	IMN-Ab$_1$	Photo-luminescence	0.10 ng.mL^{-1} – 100 ng.mL^{-1}	27 pg.mL^{-1}	[51]
Multi-CAT-AuNPs-Ab$_2$	MB-Ab$_1$	Colorimetric	50 pg.mL^{-1} - 20 ng. mL^{-1}	30 pg. mL^{-1}	[52]

TW: This work; **Multi-CAT-AuNP-Ab$_2$**: Polyclonal Goat *anti*-Human PSA/catalase-labelled gold nanoparticles; **HRP-Ab$_2$-SiO$_2$NSs**: Horseradish peroxidase-labelled *anti*-PSA antibody/silicon dioxide nanospheres; **CdTe@SiO$_2$-Ab$_2$**: PSA-labelled cadmium telluride@silica core-shell nanoparticles. **HRP-*anti*-PSA-IgG**: Horseradish peroxidase-labelled *anti*-PSA antibody. **Ag/SiO$_2$@RuBpy@SiO$_2$-Ab$_2$**: A three layered silver core-shell, outer layered RuBpy doped-silica fluorescent composites surface functionalized with PSA antibody. **IMN**: Immunomagnets.

4.6 Conclusions

We have developed a highly sensitive and selective fluorescence immunoassay for rapid detection of PSA using *anti*-PSA polyclonal antibody fluorescent silica nanobioconjugates for fluorescence sensing and nanomagnetic-silica antibody conjugates for PSA capture. The step-by-step preparation and characterization of the nanomagnetic-silica antibody conjugates was followed using microscopic and spectroscopic techniques. The preparation was successful as spherical nanomagnetic-silica antibody capture nanobioprobes were obtained. A sandwich immunocomplexes of the fluorescent silica sensing nanobioconjugates and nanomagnetic-silica capture bioprobes formed through two immunoreactions used for the accurate detection of PSA. Compared with common ELISA methods, the nanomagnetic-silica capture bioprobes assisted in PSA enrichment using a magnet to separate the captured PSA from the matrix. In addition, the fluorescent silica nanobioconjugate, enhanced the fluorescence intensity upon dissolution, using NaOH. This resulted in amplified fluorescence signs due to the FITC molecules being released, and enhancing the sensitivity of the immunoassay. The combined effects of the low background noise and increased fluorescence signals increased the fluorescence intensity resulting in a low limit of detection and limit of quantification in the pg.mL^{-1}. Moreover, the oriented bioconjugation of monoclonal and polyclonal PSA antibodies promoted specificity and selectivity to PSA. Potential interfering proteins could not be detected using this system confirming its specificity and selectivity even at higher concentrations. The presented immunoassay was demonstrated to be simple, specific, ultrasensitive, and showed good use of PSA detection in serum samples.

4.7 References

[1] Y. Wu, Y. Wang, Z. Huang, Q. Liu, Recent advances in analysis technology for detection of prostate cancer biomarkers, Microchem. J. 190 (2023) 108740.

[2] L. Li, W. Zhang, Y. Wei, L. Yu, D. Feng, A Sensitive Fluorescent Immunoassay for Prostate Specific Antigen Detection Based on Signal Amplify Strategy of Horseradish Peroxidase and Silicon Dioxide Nanospheres, J. Anal. Methods Chem. 2022 (2022) 1–9.

[3] G. Perry, F. Cortezon-Tamarit, S.I. Pascu, Detection and monitoring prostate specific antigen using nanotechnology approaches to biosensing, Front. Chem. Sci. Eng. 14 (2020) 4–18.

[4] J. Oto, Á. Fernández-Pardo, M. Royo, D. Hervás, L. Martos, C.D. Vera-Donoso, M. Martínez, M.J. Heeb, F. España, P. Medina, S. Navarro, A predictive model for prostate cancer incorporating PSA molecular forms and age, Sci. Rep. 10 (2020) 2463.

[5] R.L. Siegel, K.D. Miller, A. Jemal, Cancer statistics, 2020, CA. Cancer J. Clin. 70 (2020) 7–30.

[6] P. Rawla, Epidemiology of Prostate Cancer, World J. Oncol. 10 (2019) 63–89.

[7] J. Constantinou, M.R. Feneley, PSA testing: An evolving relationship with prostate cancer screening, Prostate Cancer Prostatic Dis. 9 (2006) 6–13.

[8] D. Damborska, T. Bertok, E. Dosekova, A. Holazova, L. Lorencova, P. Kasak, J. Tkac, Nanomaterial-based biosensors for detection of prostate specific antigen, Microchim. Acta. 184 (2017) 3049–3067.

[9] M.S. Litwin, H.-J. Tan, The Diagnosis and Treatment of Prostate Cancer, JAMA. 317 (2017) 2532 – 2542.

[10] T.R. Rebbeck, K. Burns-White, A.T. Chan, K. Emmons, M. Freedman, D.J. Hunter, P. Kraft, F. Laden, L. Mucci, G. Parmigiani, D. Schrag, S. Syngal, R.M. Tamimi, K. Viswanath, M.B. Yurgelun, J.E. Garber, Precision Prevention and Early Detection of Cancer: Fundamental Principles, Cancer Discov. 8 (2018) 803–811.

[11] J.L. Descotes, Diagnosis of prostate cancer, Asian J. Urol. 6 (2019) 129–136.

[12] Y. Gao, J. Xie, H. Chen, S. Gu, R. Zhao, J. Shao, L. Jia, Nanotechnology-based intelligent drug design for cancer metastasis treatment, Biotechnol. Adv. 32 (2014) 761–777.

[13] E.A. Stura, B.H. Muller, M. Bossus, S. Michel, C. Jolivet-Reynaud, F. Ducancel, Crystal Structure of Human Prostate-Specific Antigen in a Sandwich Antibody Complex, J. Mol. Biol. 414 (2011) 530–544.

[14] D.C. Pérez-Ibave, C.H. Burciaga-Flores, M.Á. Elizondo-Riojas, Prostate-specific antigen (PSA) as a possible biomarker in non-prostatic cancer: A review, Cancer Epidemiol. 54 (2018) 48–55.

[15] H. Van Poppel, M.J. Roobol, C.R. Chapple, J.W.F. Catto, J. N'Dow, J. Sønksen, A. Stenzl, M. Wirth, Prostate-specific Antigen Testing as Part of a Risk-Adapted Early Detection Strategy for Prostate Cancer: European Association of Urology Position and Recommendations for 2021, Eur. Urol. 80 (2021) 703–711.

[16] L. Yang, H. Zhao, G. Deng, X. Ran, Y. Li, X. Xie, C.P. Li, Immunosensor for prostate-specific antigen using Au/Pd@flower-like SnO_2 as platform and Au@mesoporous carbon as signal amplification, RSC Adv. 5 (2015) 74046–74053.

[17] P. Song, B. Yang, Z. Peng, J. Zhou, Z. Ren, K. Fang, L. Yang, L. Wang, Q. Dong, Reduced cancer-specific survival of low prostate-specific antigen in high-grade

prostate cancer: A population-based retrospective cohort study, Int. J. Surg. 76 (2020) 64–68.

[18] G.S.M. Kammeijer, J. Nouta, J.J.M.C.H. de la Rosette, T.M. de Reijke, M. Wuhrer, An In-Depth Glycosylation Assay for Urinary Prostate-Specific Antigen, Anal. Chem. 90 (2018) 4414–4421.

[19] Y. Zhao, W. Gao, X. Ge, S. Li, D. Du, H. Yang, CdTe@SiO_2 signal reporters-based fluorescent immunosensor for quantitative detection of prostate specific antigen, Anal. Chim. Acta. 1057 (2019) 44 – 50.

[20] S. Veeranarayanan, A. Cheruvathoor Poulose, S. Mohamed, A. Aravind, Y. Nagaoka, Y. Yoshida, T. Maekawa, D.S. Kumar, FITC Labeled Silica Nanoparticles as Efficient Cell Tags: Uptake and Photostability Study in Endothelial Cells, J. Fluoresc. 22 (2012) 537–548.

[21] M.D. Nguyen, H.V. Tran, S. Xu, T.R. Lee, Fe_3O_4 Nanoparticles: Structures, Synthesis, Magnetic Properties, Surface Functionalization, and Emerging Applications, Appl. Sci. 11 (2021) 11301.

[22] L. Zhang, H. Shao, H. Zheng, T. Lin, Z. Guo, Synthesis and characterization of Fe_3O_4@SiO_2 magnetic composite nanoparticles by a one-pot process, Int. J. Miner. Metall. Mater. 23 (2016) 1112–1118.

[23] R.C. Popescu, E. Andronescu, B.S. Vasile, Recent Advances in Magnetite Nanoparticle Functionalization for Nanomedicine, Nanomaterials. 9 (2019) 1791.

[24] A.S. Teja, P.-Y. Koh, Synthesis, properties, and applications of magnetic iron oxide nanoparticles, Prog. Cryst. Growth Charact. Mater. 55 (2009) 22–45.

[25] L. Zhang, R. He, H.C. Gu, Oleic acid coating on the monodisperse magnetite nanoparticles, Appl. Surf. Sci. 253 (2006) 2611–2617.

[26] F. Ahangaran, A. Hassanzadeh, S. Nouri, Surface modification of $Fe_3O_4@SiO_2$ microsphere by silane coupling agent, Int. Nano Lett. 3 (2013) 23.

[27] S. Mohapatra, N. Panda, P. Pramanik, Boronic acid functionalized superparamagnetic iron oxide nanoparticle as a novel tool for adsorption of sugar, Mater. Sci. Eng. C. 29 (2009) 2254–2260.

[28] C.Y. Wang, J.M. Hong, G. Chen, Y. Zhang, N. Gu, Facile method to synthesize oleic acid-capped magnetite nanoparticles, Chinese Chem. Lett. 21 (2010) 179–182.

[29] N. V. Jadhav, A.I. Prasad, A. Kumar, R. Mishra, S. Dhara, K.R. Babu, C.L. Prajapat, N.L. Misra, R.S. Ningthoujam, B.N. Pandey, R.K. Vatsa, Synthesis of oleic acid functionalized Fe_3O_4 magnetic nanoparticles and studying their interaction with tumor cells for potential hyperthermia applications, Colloids Surfaces B Biointerfaces. 108 (2013) 158–168.

[30] M. Bloemen, W. Brullot, T.T. Luong, N. Geukens, A. Gils, T. Verbiest, Improved functionalization of oleic acid-coated iron oxide nanoparticles for biomedical applications, J. Nanoparticle Res. 14 (2012) 1100.

[31] Q. Fan, Y. Guan, Z. Zhang, G. Xu, Y. Yang, C. Guo, A new method of synthesis well-dispersion and dense $Fe_3O_4@SiO_2$ magnetic nanoparticles for DNA extraction, Chem. Phys. Lett. 715 (2019) 7–13.

[32] S. Wang, J. Tang, H. Zhao, J. Wan, K. Chen, Synthesis of magnetite–silica core–shell nanoparticles via direct silicon oxidation, J. Colloid Interface Sci. 432 (2014) 43–46.

[33] Z. Lu, J. Dai, X. Song, G. Wang, W. Yang, Facile synthesis of Fe_3O_4/SiO_2 composite nanoparticles from primary silica particles, Colloids Surfaces A Physicochem. Eng. Asp. 317 (2008) 450–456.

[34] O. Adeniyi, S. Sicwetsha, P. Mashazi, Nanomagnet-Silica Nanoparticles Decorated with Au@Pd for Enhanced Peroxidase-Like Activity and Colorimetric Glucose Sensing, ACS Appl. Mater. Interfaces. 12 (2020) 1973–1987.

[35] G. Asab, E.A. Zereffa, T. Abdo Seghne, Synthesis of Silica-Coated Fe_3O_4 Nanoparticles by Microemulsion Method: Characterization and Evaluation of Antimicrobial Activity, Int. J. Biomater. 2020 (2020) 1–11.

[36] A. Adesina, O. Adeniyi, P. Mashazi, Nanomagnet Bioconjugates with anti -CRP Polyclonal Antibodies as Nanobioprobes for Enhanced Impedimetric Detection of CRP, Electroanalysis. 35 (2023) 120 - 130.

[37] S. Kralj, M. Drofenik, D. Makovec, Controlled surface functionalization of silica-coated magnetic nanoparticles with terminal amino and carboxyl groups, J. Nanoparticle Res. 13 (2011) 2829–2841.

[38] P.C. Lin, S.H. Chen, K.Y. Wang, M.L. Chen, A.K. Adak, J.R.R. Hwu, Y.J. Chen, C.C. Lin, Fabrication of Oriented Antibody-Conjugated Magnetic Nanoprobes and Their Immunoaffinity Application, Anal. Chem. 81 (2009) 8774–8782.

[39] C. Bi, S. Zhang, Y. Li, X. He, L. Chen, Y. Zhang, Boronic acid-functionalized iron oxide magnetic nanoparticles via distillation–precipitation polymerization and thiol–yne click chemistry for the enrichment of glycoproteins, New J. Chem. 42 (2018) 17331–17338.

[40] X. Xue, H. Gong, H. Zheng, L. Ye, Boronic Acid Functionalized Nanosilica for Binding Guest Molecules, ACS Appl. Nano Mater. 4 (2021) 2866–2875.

[41] K. Wu, J. Liu, V. K. Chugh, S. Liang, R. Saha, V. D. Krishna, M.C. Cheerran, J. Wang, Magnetic nanopaticles and magnetic particles spectroscopy-based bioassys: a 15 yearr recap, Nano. Futur. 6 (2022) 022001.

[42] L. Lu, X. Wang, C. Xiong, L. Yao, Recent advances in biological detection with magnetic nanoparticles as a useful tool, Sci. China Chem. 58 (2015) 793–809.

[43] S. Carinelli, M. Luis-Sunga, J. L. González-Mora, P. A. Salazar-Carballo, Synthesis and modification of magnetic nanoparticles for biosensing and bioassay application: A review. Chemosensor, 11 (2023) 533.

[44] O.K. Adeniyi, A. Ngqinambi, P.N. Mashazi, Ultrasensitive detection of anti-p53 autoantibodies based on nanomagnetic capture and separation with fluorescent sensing nanobioprobe for signal amplification, Biosens. Bioelectron. 170 (2020) 112640.

[45] A.B. Ganganboina, A.D. Chowdhury, I.M. Khoris, F. Nasrin, K. Takemura, T. Hara, F. Abe, T. Suzuki, E.Y. Park, Dual modality sensor using liposome-based signal amplification technique for ultrasensitive norovirus detection, Biosens. Bioelectron. 157 (2020) 112169.

[46] M. Ben Ismail, E. de la Serna, G. Ruiz-Vega, T. García-Berrocoso, J. Montaner, M. Zourob, A. Othmane, E. Baldrich, Using magnetic beads and signal amplifiers to produce short and simple immunoassays: Application to MMP-9 detection in plasma samples, Anal. Chim. Acta. 999 (2018) 144–154.

[47] R. Hufschmid, H. Arami, R.M. Ferguson, M. Gonzales, E. Teeman, L.N. Brush, N.D. Browning, K.M. Krishnan, Synthesis of phase-pure and monodisperse iron oxide nanoparticles by thermal decomposition, Nanoscale. 7 (2015) 11142–11154.

[48] D.K. Kim, J.W. Lee, Synthesis of Non-hydrate Iron Oleate for Eco-friendly Production of Monodispersed Iron Oxide Nanoparticles, J. Korean Ceram. Soc. 55 (2018) 625–634.

[49] H.L. Ding, Y.X. Zhang, S. Wang, J.M. Xu, S.C. Xu, G.H. Li, Fe_3O_4@SiO_2 Core/Shell Nanoparticles: The Silica Coating Regulations with a Single Core for Different Core Sizes and Shell Thicknesses, Chem. Mater. 24 (2012) 4572–4580.

[50] R.M. Patil, P.B. Shete, N.D. Thorat, S. V. Otari, K.C. Barick, A. Prasad, R.S. Ningthoujam, B.M. Tiwale, S.H. Pawar, Non-aqueous to aqueous phase transfer of oleic acid coated iron oxide nanoparticles for hyperthermia application, RSC Adv. 4 (2014) 4515–4522.

[51] J. Nayeem, M.A.A. Al-Bari, M. Mahiuddin, M.A. Rahman, O.T. Mefford, H. Ahmad, M.M. Rahman, Silica coating of iron oxide magnetic nanoparticles by reverse microemulsion method and their functionalization with cationic polymer P(NIPAm-co-AMPTMA) for antibacterial vancomycin immobilization, Colloids Surfaces A Physicochem. Eng. Asp. 611 (2021) 125857.

[52] C. Hui, C. Shen, J. Tian, L. Bao, H. Ding, C. Li, Y. Tian, X. Shi, H.-J. Gao, Core-shell Fe_3O_4@SiO_2 nanoparticles synthesized with well-dispersed hydrophilic Fe_3O_4 seeds, Nanoscale. 3 (2011) 701–705.

[53] A. Łupicka-Słowik, R. Grzywa, E. Leporowska, D. Procyk, J. Oleksyszyn, M. Sieńczyk, Development and Evaluation of an Immunoglobulin Y-Based ELISA for Measuring Prostate Specific Antigen in Human Serum, Ann. Lab. Med. 39 (2019) 373–380.

[54] D.D. Xu, Y.L. Deng, C.Y. Li, Y. Lin, H.W. Tang, Metal-enhanced fluorescent dye-doped silica nanoparticles and magnetic separation: A sensitive platform for one-step fluorescence detection of prostate specific antigen, Biosens. Bioelectron. 87 (2017) 881–887.

[55] Z. Gao, M. Xu, L. Hou, G. Chen, D. Tang, Magnetic Bead-Based Reverse Colorimetric Immunoassay Strategy for Sensing Biomolecules, Anal. Chem. 85 (2013) 6945–6952.

Chapter 5

5 Conclusion and future perspectives

5.1 Conclusions

The thesis aim was to prepare fluorescent FITC-doped silica antibody nanoparticles and nanomagnetic-silica nanoparticles for selective, specific, and ultrasensitive detection prostate-specific antigen (PSA) at ultra-low concentrations. Several objectives were set and achieved by developing a simple fluorescent silica antibody nanobioprobes with excellent fluorescence properties. The nanobioprobes encapsulating FITC as fluorophore, FITC@SiO_2-prAmPBA-*anti*-PSA-pAb/glucose, were prepared and characterized fully. The nanobioprobes were bioconjugated with *anti*-PSA-pAb successfully for specific, selective and ultrasensitive detection of PSA using TES-prAmPBA for controlled orientation. The fluorescence silica nanoparticles also carried 3.0% and 6.0% of the fluorophores. 6.0% FITC-doped nanoparticles exhibited fluorescence properties with high signal amplification and sensitivity especially after dissolution with NaOH (alkali hydrolysis) which led to the release of the FITC molecules into solution. Low background noise and increased fluorescence intensity resulted in ultra-low detection limits in the pg.mL^{-1}. The detection of PSA was via the fluorescence-linked immunosorbent assay on the black 96-well microplates coated with monoclonal *anti*-PSA-mAb as capture protein. In addition, magnetic nanoparticles were further bioconjugated with capture protein, monoclonal *anti*-PSA-mAb, Fe_3O_4@SiO_2-prAmPBA-*anti*-PSA-mAb/glucose. The magnetic nanoparticles were used to enrich the target PSA biomarker from the samples. A sandwich immunocomplexes of Fe_3O_4@SiO_2-prAmPBA-*anti*-PSA-mAb<PSA>pAb-PSA-*anti*-prAmPBA-SiO_2@FITC were formed through two immunoreactions and used for the accurate detection of PSA. Compared with common ELISA methods, FITC@SiO_2-

prAmPBA-*anti*-PSA-pAb/glucose nanobioprobes showed enhanced fluorescence intensity since the silica shell reduced the photobleaching of the optical properties of FITC. In addition, the target PSA enrichment through the nanomagnetic Fe_3O_4@SiO_2-prAmPBA-*anti*-PSA-mAb/glucose bioprobes further enhanced the sensitivity of immunosensor. The proposed immunoassay used NaOH dissolution fluorescence immunosorbent assay for the ultra-low detection of PSA in pg.mL^{-1} and exhibited high sensitivity wide concentration range up to 100 ng.mL^{-1} covering the clinical range for the quantitative PSA screening. The immunoassay was demonstrated to be simple, specific, and sensitive, and showed good use of PSA detection even in serum samples.

5.2 Future perspectives

The fluorescence systems developed for the detection of PSA still require the use of real samples and validation with clinical samples. Monitoring and quantifying PSA levels is crucial in the diagnosis of prostate cancer. PSA alone is not specific to prostate cancer therefore, there is a need for the detection of PSA and its isoforms for total PSA, free-PSA and complex-PSA. These biomarkers if quantified can be specific for prostate cancer diagnosis. The discrimination between benign and malignant increased concentration of PSA is also another factor to take into account when diagnosing prostate cancer. The use of a ratio of free-PSA to complexed-PSA and use of threshold analysis will assist in determining the positive prostate cancer diagnosis for the benign and prostate cancer diagnosis. The detection of other biomarkers for prostate cancer would also be investigated for multiplexed detection which will result in the definitive diagnosis.

6 Chapter 3 Appendix

^{1}H-NMR of FITC-APTES

The proton (^{1}H) NMR was used for the characterization of FITC-APTES measured in DMSO-d_6. **Figure S3.1** shows the ^{1}H NMR spectrum of the synthesized FITC-APTES. The proton NMR was used to obtain structural information and successful formation of FITC-APTES. From the spectrum, a triplet peak at 1.04 ppm attributed to the CH_3 from the APTES. At 0.8 ppm and, 1.56, and 2.25 ppm are attributed to the aliphatic CH_2 groups of APTES. 3.25 ppm is attributed to the CH_2 and NH protons. Downfield of the spectrum, the peaks at 6.58 ppm, 7.67, and at 8.12 ppm are attributed to the aromatic ring protons from FITC, respectively. Lasty, at 10.13 attributed to the OH protons from FITC. Therefore, confirming the successful formation of FITC-APTES.

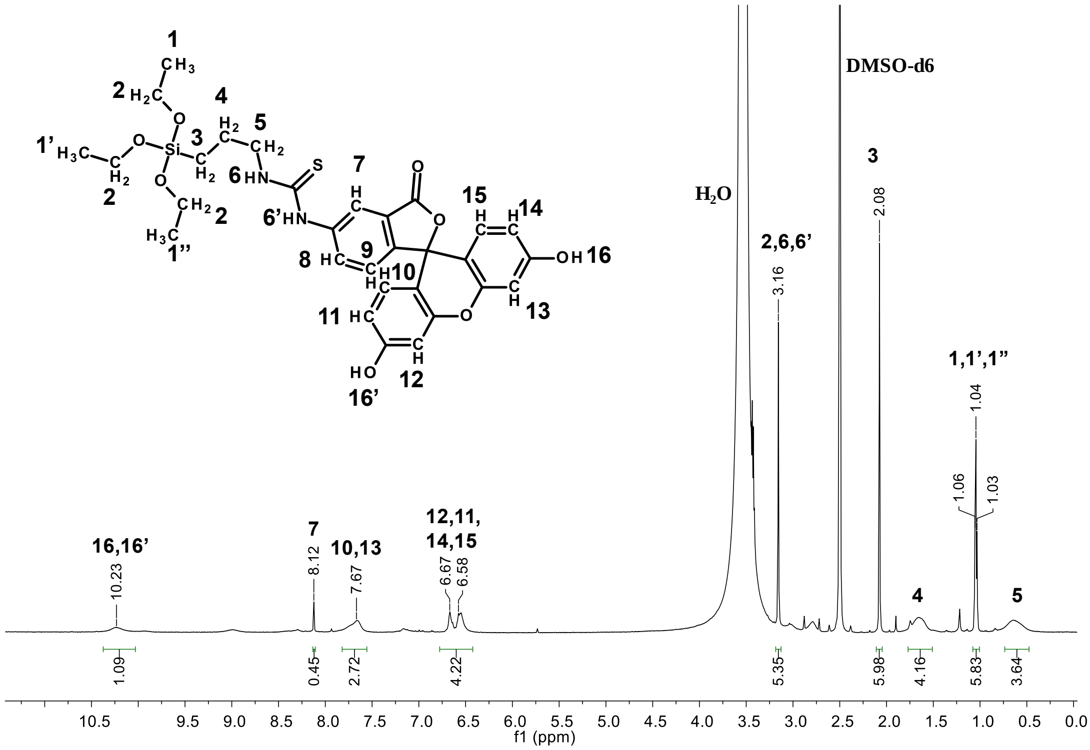

Figure S3.1: ^{1}H NMR spectrum of fluorescein-isothiocyanito-3-propyltriethoxysilane (FITC-APTES) measured in DMSO-d_6.

Synthesis of TES-prAmPBA

As one of the components for the preparation of fluorescent silica antibody nanobioprobes, triethoxysilanepropyl-3-amido phenylboronic acid (TES-prAmPBA) was synthesized to introduce the boronic acid functional group used for oriented antibody bioconjugation. The carboxylic acid functional group of 4-carboxyphenylboronic acid (4-CPBA) are reacted with the primary amine group of APTES and resulting in TES-prAmPBA through secondary amide bond formation. TES-prAmPBA was surface functionalized onto fluorescent silica nanoparticles through a covalent attachment via siloxane bond formation.

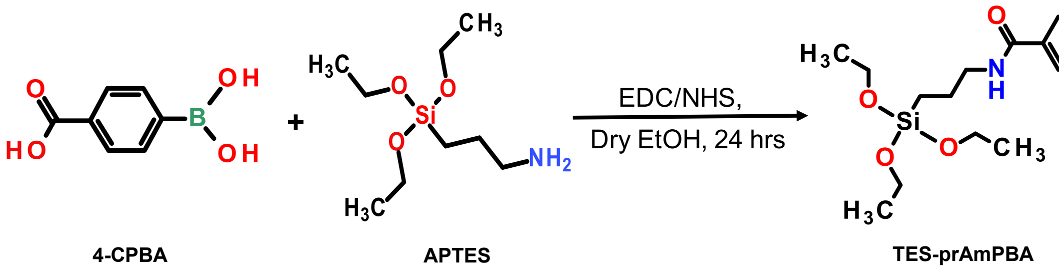

Scheme S3.1: Synthesis of triethoxysilanepropyl-3-amido phenylboronic acid (TES-prAmPBA).

^{1}H-NMR of TES-prAmPBA

Figure S3.2 below shows the ^{1}H NMR spectrum of TES-prAmPBA measured in DMSO-d_6. From the spectrum, the aromatic protons are observed between 5.50 ppm and 5.78 ppm and the aliphatic (CH_3) protons at 1.25 ppm. The two protons on N-CH_2 from the propyl (CH_2 group) are observed at 2.11 ppm, and the NH proton from the amide bond was broad at 10.25 ppm. Therefore, confirming the successful formation of TES-prAmPBA.

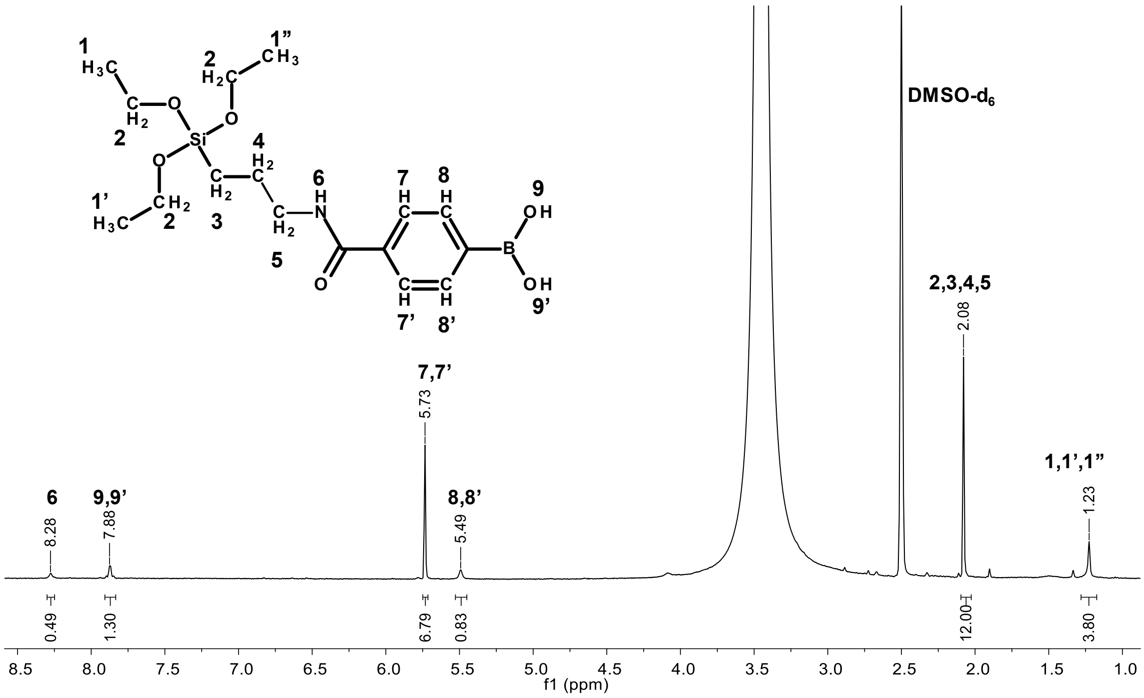

Figure S3.2: ^{1}H NMR spectrum of triethoxysilanepropyl-3-amido phenylboronic acid (TES-prAmPBA) measured in DMSO-d_6.

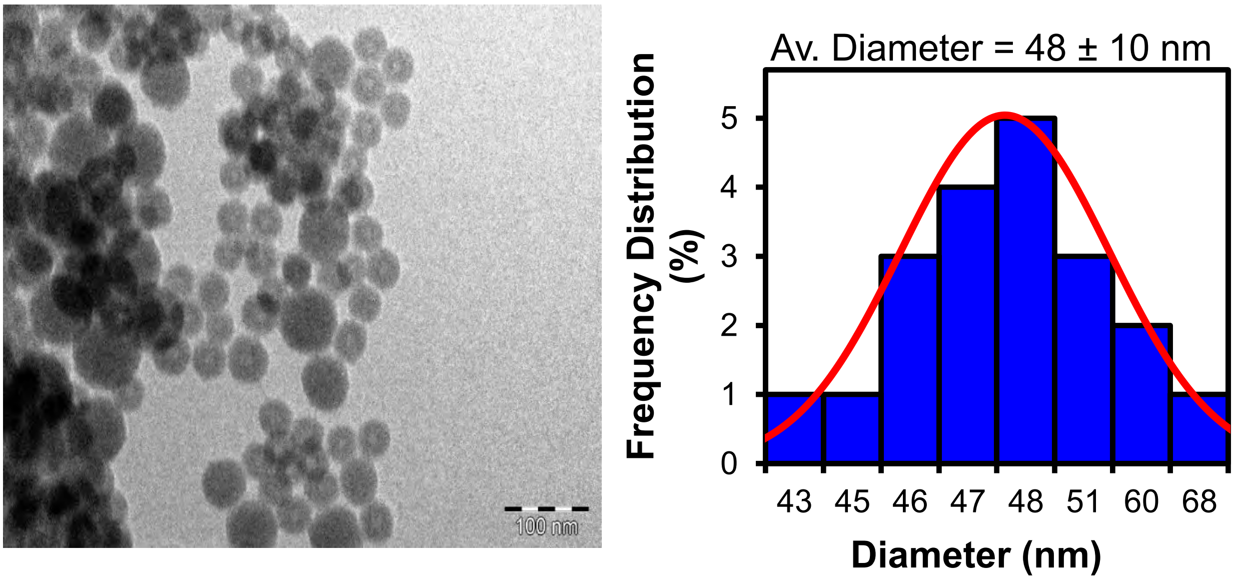

Figure S3.3: TEM image of FITC@SiO$_2$-prAmPBA-*anti*-PSA-pAb nanoparticles and the corresponding size distribution histogram.

Dye-Leakage and photostability study

The photostability comparison study of (a) FITC, (b) FITC-APTES, and (c) FITC@SiO_2NPs over 50 min and looked at the amount of dye encapsulated in FITC@SiO_2NPs. The excitation wavelength values used was 480 nm. The emission values were obtained at 520 nm FITC, 518 nm for both FITC-APTES, and FITC@SiO_2NPs.

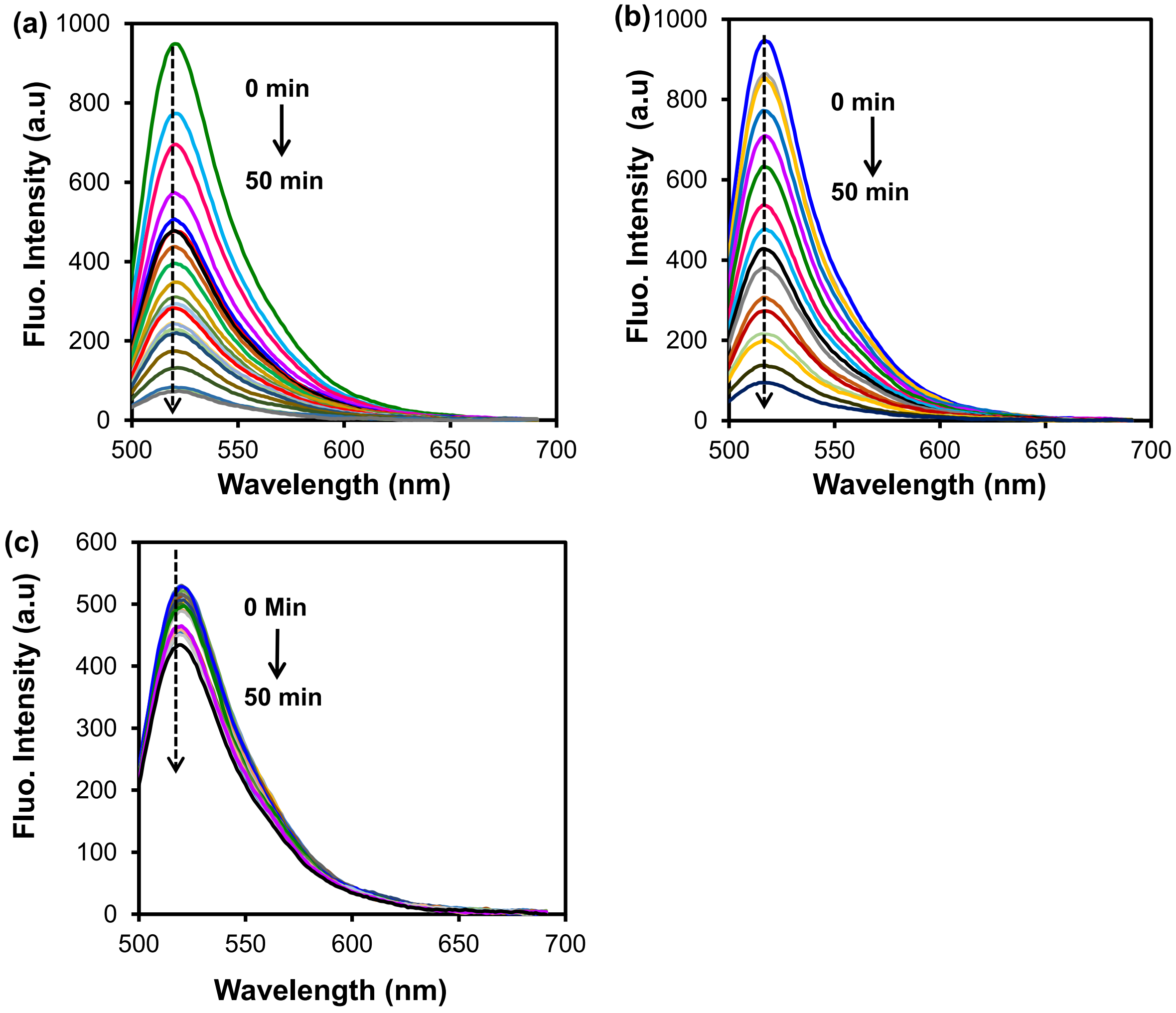

Figure S3.4: Fluorescence spectra of (a) FITC, (b) FITC-APTES, and (c) FITC@SiO_2NPs. All samples were diluted in PBS buffer (pH 7.4) and measurements were taken at 5 min intervals.

7 Chapter 4 Appendix

Figure S4.1(a) the UV-Vis spectra of (i) Fe_3O_4@SiO_2-prAmPBA-*anti*-PSA-mAb/glucose capture bioprobes show no absorption properties (along with the nanomagnetic nanoparticles and the functionalization steps). The FITC@SiO_2-prAmPBA-*anti*-PSA-pAb/glucose sensing nanobioconjugates exhibits absorption properties at 495 nm. Similarly, the Fe_3O_4@SiO_2-prAmPBA-*anti*-PSA-mAb/glucose showed no fluorescence emission properties. On the other hand, the FITC@SiO_2-prAmPBA-*anti*-PSA-pAb/glucose fluorescence emission is observed at 518 nm as shown in **Figure S4.1(b)**.

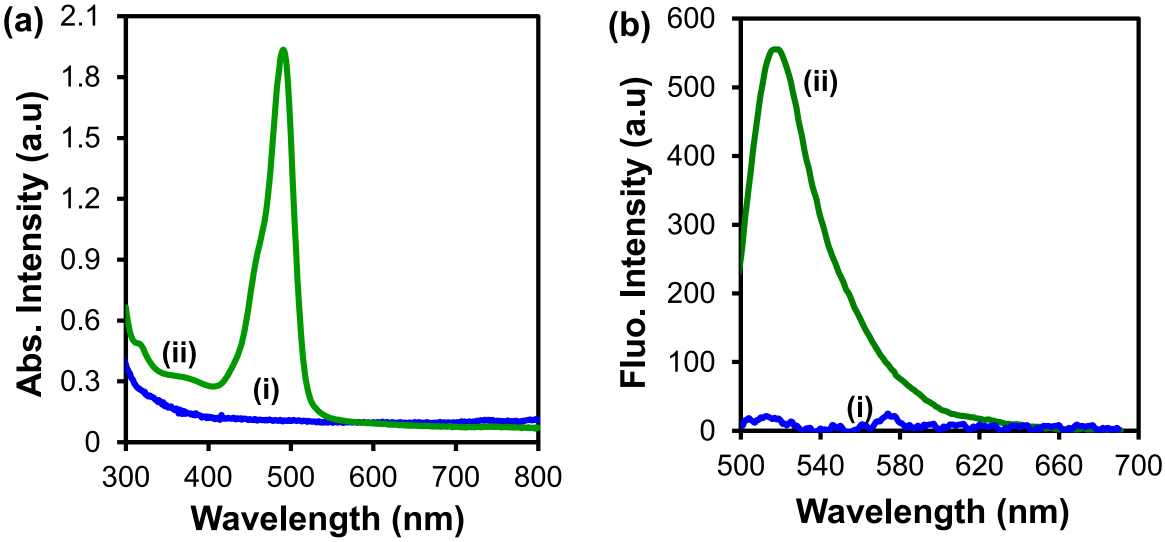

Figure S4.1: (a) UV-Vis and (b) fluorescence spectra of (i) Fe_3O_4@SiO_2-prAmPBA-*anti*-PSA-mAb/glucose capture nanobioprobes and (ii) FITC@SiO_2-prAmPBA-*anti*-PSA-pAb/glucose sensing nanobioconjugates.